Development and Impedance Control of Lightweight Shape Memory Alloy Actuated Robotic Arms

Auri Cormier

A Thesis Submitted to the Faculty of Graduate Studies in Partial Fulfillment of the Requirements for the Degree of Master of Science

Graduate Program in Earth and Space Science
York University
Toronto, Ontario

December 2025

Abstract

Shape memory alloys (SMAs) have been proposed as a lightweight actuator for robotic applications. Their low mass makes them an excellent candidate for aerial manipulation, where reducing the mass of a manipulator can increase usable payload and save energy. Existing SMA-actuated robotic arms are restricted in their size, strength, and degrees of freedom (DOFs). This thesis develops two 3-DOF, SMA-actuated robotic arms suitable for aerial manipulation.

The developed arms are significantly more capable than existing SMA-actuated arms and can manipulate masses of up to 300 g. A novel compliant joint design is introduced that allows for simultaneous control of antagonistic SMA actuators. The joint provides direct measurements of the torque applied by each actuator, allowing for the development of a multi-level impedance controller. Finally, an extended Kalman filter formulation is introduced and integrated into the multi-DOF robotic arm.

Acknowledgements

I would like to thank my research advisor and supervisor, Dr. Michael Bazzocchi, for his guidance and assistance in this work. He has created a lab environment filled with passion and positivity that I am grateful to be a part of. I learn more every day, and look forward to continuing to do so.

I also thank Dr. Marcias Martinez for his extensive optimization and materials science knowledge. The time he took to share this with me is greatly appreciated, and his support allowed me to explore research topics I never could have completed on my own.

Finally, I thank my research committee members: Dr. Ryan Orszulik, Dr. Jinjun Shan, and Dr. George Zhu for their continued support and participation on the committee. Our discussions regarding my work have been insightful, thoughtful, and have guided me to the conclusion of my work.

Table of Contents

List of Tables

List of Figures

Nomenclature

A_f	Austenite Finish Temperature (°C)
A_s	Austenite Start Temperature (°C)
A_w	SMA Wire Surface Area (m^2)
a_w	SMA Wire Cross-Sectional Area (m^2)
$\mathbf{B}$	Compliant Joint Damping Coefficient (Nm°/s)
$\boldsymbol{C}$	Coriolis/Centrifugal Matrix of Robotic Arm (Nm)
c_p	SMA Wire Specific Heat (J/kg°K)
D_a	Actuator Z-axis distance (m)
d_n	X-Direction Distance to Link n Center of Mass (m)
E	SMA Wire Young's Modulus (MPa)
E_1	3D Printed Intraplanar Young's Modulus (GPa)
E_2	3D Printed Interplanar Young's Modulus (GPa)
$\mathbf{F_k}$	Extended Kalman Filter State Transition Function Jacobian
F_x	X-Axis Force (N)
F_y	Y-Axis Force (N)
f	Extended Kalman Filter State Transition Function
$\boldsymbol{G}$	Gravity Compensation Matrix of Robotic Arm (Nm)
G_{12}	3D Printed Bending Modulus (GPa)

h SMA Wire Heat Transfer Coefficient (W/m^2°K)

I Identity Matrix

$\boldsymbol{K}_k$ Extended Kalman Filter Kalman Gain

$\mathbf{K}$ Compliant Joint Spring Coefficient (Nm/°)

$\mathbf{K}_d$ Actuator Position Controller Derivative Gain

$\mathbf{K}_{da}$ Antagonistic Position Controller Derivative Gain

$\mathbf{K}_{dg}$ Joint Position Controller Derivative Gain

$\mathbf{K}_i$ Actuator Position Controller Integral Gain

$\mathbf{K}_{ig}$ Joint Position Controller Integral Gain

$\mathbf{K}_{ia}$ Antagonistic Position Controller Integral Gain

$\mathbf{K}_p$ Actuator Position Controller Proportional Gain

$\mathbf{K}_{pg}$ Joint Position Controller Proportional Gain

$\mathbf{K}_{pa}$ Antagonistic Position Controller Proportional Gain

k Simulation / Control Step Number

L_n Length of Arm Link n (m)

L_w SMA Wire Length (m)

l_c Length to Center of Mass of Arm Link (m)

$\mathbf{M}$ Mass Matrix of Robotic Arm (Nms^2/rad)

M_f Martensite Finish Temperature (°C)

M_s Martensite Start Temperature (°C)

M_x X-Axis Moment (Nm)

M_y Y-Axis Moment (Nm)

m_n Mass of Arm Link n (kg)

m_w Mass of SMA Wire (kg)

N_w	Number of Wires in SMA Actuator
n	Joint Number
$\mathbf{P}_k$	Extended Kalman Filter Predicted Covariance
P_x	X-Position of Arm Wrist (m)
P_y	Y-Position of Arm Wrist (m)
$\mathbf{Q}_k$	Extended Kalman Filter Process Covariance
$\mathbf{q}$	Robotic Arm Link Angle (°)
$\mathbf{q_d}$	Desired Robotic Arm Link Angle (°)
$\mathbf{q_m}$	Measured Robotic Arm Link Angle (°)
R	SMA Wire Resistance (Ω)
R_a	Resistance of SMA Wire in Austenite Phase (Ω)
$\mathbf{R}_k$	Extended Kalman Filter Measurement Covariance
R_m	Resistance of SMA Wire in Martensite Phase (Ω)
r_n	SMA Actuator Mounting Radius for Joint n (m)
S	Clockwise/Counterclockwise Switching Term
$\mathbf{S}_k$	Extended Kalman Filter Residual Covariance
$\mathbf{T}$	SMA Wire Temperature (°C)
T_{amb}	Room Temperature (°C)
$\mathbf{T}_w$	Waypoint Time (s)
t_s	Timestep Length (s)
$\mathbf{u}$	Extended Kalman Filter Input Vector
$\mathbf{V}$	SMA Actuator Voltage (V)
V_{cw}	Clockwise SMA Actuator Voltage (V)
V_{ccw}	Counterclockwise SMA Actuator Voltage (V)

X_{11}	Tensile Strength (MPa)
X_{12}	Transverse Strength (MPa)
X_{22}	Shear Strength (MPa)
X_{EE}	X-Position of End-Effector (m)
$\mathbf{x}$	Extended Kalman Filter State Vector
$\hat{\mathbf{x}}$	Extended Kalman Filter Estimated State Vector
Y_{EE}	Y-Position of End-Effector (m)
$\mathbf{z_k}$	Extended Kalman Filter Observation Matrix
fi	Impedance Controller Damping Coefficient (Nm°/s)
γ	Normalized Time
ϵ	SMA Wire Strain
ϵ_t	SMA Wire Transformation Strain
ϵ_s	SMA Wire Elastic Strain
ϵ_m	SMA Wire Maximum Strain
Θ	SMA Constitutive Model Temperature Dependence
θ_{EE}	End-Effector Angle Relative To Base Frame (°)
θ_a	SMA Actuator Angle (°)
θ_c	Measured Encoder Angle (°)
θ_w	SMA Wire Angle (°)
˘	Impedance Controller Spring Coefficient (Nm/°)
Λ	Time Between Waypoints (s)
λ	Minimum Jerk Trajectory
ν	Poisson's Ratio
ξ	SMA Wire Phase

$\boldsymbol{\sigma}$ SMA Wire Stress (MPa)

σ_{11} Intra-Layer Stress (MPa)

σ_{22} Inter-Layer Stress (MPa)

σ_{13} x-Z Bending Stress (MPa)

σ_{23} X-Y Bending Stress (MPa)

$\sigma_{w,max}$ Maximum Allowable Wire Stress (MPa)

$\boldsymbol{\emptyset}$ Joint Torque (Nm)

$\boldsymbol{\emptyset_{a,n}}$ Maximum Torque For Joint n (Nm)

$\tau_{l,n}$ Joint Torque Limit for Joint n (Nm)

$\boldsymbol{\emptyset_{m,n}}$ Torque Applied by Link Mass for Joint n (Nm)

$\boldsymbol{\emptyset_{cmd}}$ Commanded Joint Torque Vector (Nm)

$\boldsymbol{\emptyset_{cmd,n}}$ Commanded Joint Torque for joint n (Nm)

$\boldsymbol{\phi}$ Compliant Joint Deflection (°)

$\boldsymbol{\phi}_d$ Desired Compliant Joint Deflection (°)

$\boldsymbol{\phi}_e$ Estimated Compliant Joint Deflection (°)

$\boldsymbol{\phi}_m$ Measured Compliant Joint Deflection (°)

$\boldsymbol{\phi}_{min}$ Minimum Target Compliant Joint Deflection (°)

Ω SMA Constitutive Model Phase Dependence

τ_{12} Inter-Layer Stress (MPa)

Chapter 1

Introduction

Shape memory alloys are a class of materials that are capable of deforming and returning to their original size and shape through a reversible phase transformation. If formed into a wire and stretched, the wire transforms from an austenite phase to a martensite phase, which is reversed when heated above a critical temperature. This transformation exerts significant force as the wire contracts, making SMA actuators significantly stronger by mass when compared to motor or pneumatic actuators [1].

The high strength and low mass of SMA actuators makes them particularly useful in aerial manipulation applications, where reducing the mass of a manipulator increases the available payload capacity. Multi-degree-of-freedom aerial manipulators often require large drone platforms due to the large mass of their manipulator, providing a lower bound on drone size [2]. Several papers have worked to reduce the weight of robotic arms using techniques such as topology optimization [3, 4], but the mass of servo or motor actuators cannot easily be reduced and can comprise over half of an arm's mass [5]. An SMA-actuated robotic arm designed for aerial manipulation tasks could replace heavier motor-driven arms, dramatically decreasing power usage and required drone size.

Despite their potential, existing SMA-actuated robotic arms are unsuitable for aerial manipulation due to their limited strength, range, and degrees of freedom (DOFs). To date, only two SMA-actuated robotic arms with 2-DOFs have been developed, both of which rely on a bias force to restore the actuator to its original position [6, 7]. Due to the lack of a multi-DOF arm, current SMA-actuated robotic arms are unable to complete tasks common for motor-operated robots, as none have the required degrees of freedom for position and orientation control of an end-effector. This restricts the field of SMA-actuated robotics from performing common aerial manipulation tasks, such as object grasping and manipulation, path following, and

obstacle avoidance. A 3-DOF arm would enable experimental validation of controllers and path planning algorithms that address the unique behaviour of SMA actuators during these tasks. Current SMA-actuated robotic arms are also unsuitable for aerial manipulation tasks due to their low strength, as existing designs are only able to manipulate masses of less than 75 g [7]. This payload capacity is lower than the mass of even lightweight active end-effectors in the literature [8, 9].

The strength and range of SMA-actuated robotic arms cannot easily be increased due to several design challenges specific to SMA wires. First, existing designs cannot easily increase the strength of SMA actuators without risking structural failure, as no analysis has been performed on the load application of SMA actuators. Second, size restrictions of multi-wire SMA actuators must be addressed. Existing SMA bundle actuator designs [10] cannot be spooled over rollers, making them unacceptably long for multi-DOF robotics applications.

Many control challenges regarding SMA-actuated robotic arms currently remain unsolved. Impedance control, a particularly important type of control for aerial manipulation, remains very limited despite its prevalence in motor-actuated robotics. Existing works either use load cells to directly measure SMA wire force and do not validate the controller under load [11], or are limited entirely to simulation [12]. Other SMA actuators have implemented load cells to measure torque [13, 14, 15], but do not use this for torque or impedance control.

To address the need for a lightweight, high payload SMA-actuated arm, two 3-DOF, SMA-actuated robotic arms are developed. The first arm is an improvement in scale, payload, and range over existing SMA-actuated arms. By developing an arm with three degrees of freedom, simultaneous control of the end-effector position and orientation is achieved. This control is essential for aerial manipulation tasks and has not been achieved with SMA actuators. Then, the payload capacity of the arm is increased using many parallel wires spooled over rollers, making this the first SMA-actuated arm capable of manipulating common drone payloads. The increased complexity associated with these improvements required a detailed design analysis in this thesis. The second arm iterates on the first design by increasing its range of motion and introducing a compliant SMA-actuated joint. Integrating compliant joints into the arm enables direct torque control of the joints, a capability critical to completing delicate aerial manipulation tasks.

The literature gaps regarding SMA control are also addressed in this thesis. A joint space impedance controller is integrated with a novel compliant actuator design that decouples the angle of each actuator from the load, allowing for a novel

bidirectional position control that improves on existing antagonistic actuator controllers. Finally, this work investigates the application of an extended Kalman filter (EKF) in an experimental robotic system. Existing SMA state estimation techniques are limited to simulations [16, 17], standalone actuators with no external dynamics [18], or parameter estimation instead of control [19] (with more details on existing techniques provided in Chapter 2). The process to integrate multiple SMA actuator estimators into a control system is addressed and applied in the impedance controller experiments.

This chapter outlines the motivation behind SMA-actuated robotic arm research as well as the specific motivations for the design and control works completed in this thesis. Several research objectives are outlined and the contributions each objective achieves are described. Finally, the list of publications achieved in this work and an overview of the thesis structure are included.

1.1 Motivation and Scope

The applications of aerial manipulators to solving real world problems has grown dramatically in the past decade. Drone systems are now used in agricultural monitoring [20], transmission line inspection [21], and construction surveying [22]. Recent works have focused on expanding aerial manipulator technology from passive observation to active manipulation of their environment. These aerial manipulators have been used to complete construction tasks such as sealing cracks in pipes [23], opening and closing valves [24], and installing sensors. However, this increase in task complexity requires increasingly complex and heavy manipulators. Most drone platforms have a payload capacity of only a few hundred grams [2], making the design of lightweight manipulators an essential task in progressing aerial manipulator technology.

The use of SMA actuators as an alternative to motors or pneumatic actuators in such a weight-critical application is attractive due to their extremely low mass and high strength [1]. However, significant advancements in size, complexity, and control of SMA-actuated systems are required for future use in practical aerial manipulation tasks.

Existing research in SMA-actuated arms is limited in two important ways. First, the range, payload, and degrees of freedom of existing arms are limited. The most common prototypes are only 1-DOF revolute joints [14, 25], or less commonly, 2-DOF robotic arms [6, 7]. These robotic arms are capable of only simple movements, and cannot control the position and orientation of an end-effector, as is required for many

robotics tasks. Additionally, existing arms have very limited strength and range. Even stronger arms in the literature exert less than 0.1 Nm of torque [7], which is not enough for even the most lightweight robotic grippers [8, 9].

Additionally, control of SMA-actuated robotic arms remains difficult and is often limited to position or velocity control. In particular, force or torque control of SMA-actuated robotic arms is currently limited to simulations that were not experimentally validated [12, 14], or to single joints without load [11]. Impedance control, which relates the wrench applied by a robotic arm to its position, is not well explored for SMA-actuated robotics. Extending impedance control to experimental SMA-actuated platforms is essential for cooperation with people and in unstructured environments. Impedance control of a low torque antagonistic actuator has been completed by using load cells to directly measure wire force, but was not tested under load [11]. Additionally, impedance control of a robotic arm, rather than a rotary joint, has not been completed experimentally. The development of an impedance controller for an SMA-actuated arm is particularly useful for aerial manipulation by allowing the arm to behave in a predictable and controlled manner when interacting with its environment.

This work focuses on the development and control of two SMA-actuated robotic arms on a fixed test stand. Considerations in the design, such as mass, size, and operating space, are addressed in regards to future work on an aerial manipulator. The design of these arms focuses on significantly increasing the payload, range, and degrees of freedom of existing SMA-actuated robotic arms. The proposed controllers are evaluated using experimental behaviour of the arm and compared to desired, but not optimal, results.

1.2 Goal and Objectives

The goal of this thesis is to develop a multi-DOF, SMA-actuated robotic arm and controller to achieve compliant behaviour. The payload capacity, range, and degrees of freedom of existing SMA-actuated arms will be increased. Impedance control of the arm will be achieved by introducing a compliant joint design to allow the arm to respond predictably to disturbances. Finally, an extended Kalman filter was applied to reduce measurement noise and provide insight into hidden system states. This goal was decomposed into the following objectives:

- **Objective 1 (O1):** Develop a planar 3-DOF, SMA-actuated robotic arm capable of manipulating lightweight end-effectors through a range of motion suitable

for aerial manipulation.

- **Objective 2 (O2):** Design a multi-level impedance controller for an SMA-actuated robotic arm utilizing a novel compliant joint design.
- **Objective 3 (O3):** Integrate an extended Kalman filter (EKF) into the SMA-actuated robotic arm system.

1.3 Statement of Contributions

Each objective outlined above includes several contributions to the literature, which are outlined as follows:

Objective 1 (O1)
This thesis introduces two 3-DOF robotic arms actuated by SMA wires. Both of these constitute significant advancements to the design of SMA-actuated robotic arms. The first develops a bundle actuator spooled over many rollers, creating a compact actuator that provides over 25 times the torque of existing SMA actuators in robotic arms. The second proposes a new design that integrates SMA wires within the base of the arm, keeping them stationary throughout their range of motion. These designs resulted in substantial increases in range and payload, and are the first capable of simultaneous end-effector position and orientation control. Additionally, they are the first with payload capacity high enough for practical end-effectors.

Objective 2 (O2)
This work is the first experimental validation of impedance control of an SMA-actuated robotic arm. Existing works have only completed this in simulation [12] or with no load [11]. The extension from simulation to experimental validation is achieved by introducing a novel compliant joint design that allows for direct measurement of actuator torque. Furthermore, a novel low-level controller is introduced that separately controls the position of both the clockwise and counterclockwise wire groups within an antagonistic actuator. The controller was shown to be substantially more effective in path-following tasks by maintaining both sets of wires in a pre-heated, mid-transformation state.

Objective 3 (O3)
Finally, an extended Kalman filter is implemented into a controller and used for ex-

perimental testing. Previous SMA-based works have only used an EKF in controllers for simulated arms, which assume perfect knowledge of the dynamics of the arm and actuator system [16]. Additionally, the integration of an EKF to an antagonistic SMA actuator has never been completed. Existing EKF formulations cannot be applied to antagonistic actuators, so a new formulation is introduced that uses separate estimators for each actuator coupled by the compliant joint and then the arm dynamics to create a complete system model.

1.4 Refereed Publications

As part of the completion of this thesis, two manuscripts were prepared for journal publication, corresponding to Chapters 3 and 4. The first journal paper has been published in the *Journal of Intelligent Material Systems and Structures* and the second is currently under review.

[1] A. Cormier, M.C.F. Bazzocchi, M. Martinez, "A shape memory alloy actuated robotic arm for aerial manipulation," *Journal of Intelligent Material Systems and Structures*, Vol. 36, Iss. 20, pp. 1325-1341, 2025.

[2] A. Cormier, M.C.F. Bazzocchi, "Multi-Level Impedance Control of a Shape Memory Alloy Actuated Robotic Arm," under review, 2025.

1.5 Thesis Overview

This section provides a brief overview of the chapter contents and purposes in this thesis:

Chapter 2: Literature Review
A review of the existing literature is conducted to identify gaps in SMA actuation technology. The literature review first covers the mechanics of SMA transformation and models, then explores how they are used in actuators. Additional focus is placed on SMA-actuated robotic arms and the control methods applied to them, with a final review on state estimation techniques.

Chapter 3: A Shape Memory Alloy Actuated Robotic Arm for Aerial Manipulation

This chapter describes the design and optimization process of a 3-DOF, SMA-actuated robotic arm. Topology optimization is applied to the arm links, resulting in a lightweight robotic arm suitable for aerial manipulation tasks. Then, an adaptive PI controller is applied to the arm in experimental path-following tasks. The work in this chapter was published in publication 1 [26].

Chapter 4: Multi-Level Impedance Control of an SMA-Actuated Robotic Arm

This chapter focuses on impedance control of an SMA-actuated robotic arm. It introduces a new robotic arm and compliant joint design, then evaluates a proposed multi-level controller. Each level of the controller is evaluated in experimental tests and a joint space impedance controller reached the desired joint torques as expected. Finally, the integration of an extended Kalman filter (EKF) with the arm's simulation model is completed and discussed. The work in this chapter has been prepared as a manuscript and is currently under review [27].

Chapter 5: Conclusion

The conclusion summarizes the work completed in this thesis and highlights the key contributions it makes to the literature and the world at large. The applicability of the developed arms and associated control methods to inspection and construction tasks are discussed. Finally, several opportunities for future works building on this research are identified.

Chapter 2

Literature Review

2.1 Shape Memory Alloys

Shape memory alloys (SMA) are a class of metal alloys that exhibit the shape memory effect. This effect allows the metal to "remember" a shape imposed on it during heat treatment, such as a coiled spring shape [28]. When below a transformation temperature, the metal easily stretches or bends, then returns to its original shape when heated beyond its transformation temperature. As a result, SMAs alternate between two states—the high-temperature austenite phase and the low-temperature martensite phase. They are generally formed into wires, springs, or ribbons [29] and can be integrated into various structures to take advantage of this effect.

The transformation of an SMA wire between the martensite and austenite phases is most commonly described by a well-established constitutive model introduced by [30]. This one-dimensional model describes the relationship between the phase, strain, stress, and temperature of an SMA wire. This model and others similar to it [31, 32] define a kinetic law describing the phase change of a wire and a mechanical law describing the wire's stress-strain relationship [33].

2.2 SMA Actuators

SMA actuators are appealing as an alternative to traditional actuators due to their extremely high strength-weight ratio. When contracting, very high forces can be applied even with lightweight actuators. SMA actuators have a work density of 10 J/cm^3, 25 times higher than electric motors and over 50 times that of pneumatic actuators [1]. SMA wires have the highest strength-weight ratio of any actuator under 1 lb and have

been used in a high-strength actuator capable of lifting 100 lb, which is over 300 times the actuator's weight [10]. This makes them ideal for applications where weight is an important factor.

SMA-actuated structures can be categorized into rigid, semi-rigid, and soft structures [34]. Rigid structures use traditional joints and bearings to allow movement between two links such as in [7, 17, 25]. Rigid structures can be further divided into externally mounted and embedded elements, and the paper describes the trade-offs associated with each design. Semi-rigid and soft structures embed SMA actuators into flexible materials or matrices to allow for a continuously bending joint [19, 35, 36]. SMA actuators generally take the form of either wires or springs, although some work in sheet-like coatings have occurred. Wires generally supply greater applied forces but shorter stroke length, while springs supply lower applied forces but have stroke lengths up to ten times longer than wires [29, 34].

SMA actuators are typically powered by controlling their supplied current, heating the wire through joule heating. Wire overheating due to the high required currents must be considered to prevent damage to the wire and other components [29]. To prevent this, either a maximum current limit is set or more advanced control methods are used to briefly supply higher than rated current [37]. This method improved heating times of Flexinol wires, a commercially available prefabricated SMA wire, by measuring the change in resistance of the element as it heats. Flexinol wire data sheets include a maximum safe heating current [29], but higher maximum currents were safely achieved using measurements of the wire's resistance and the developed temperature model. This technique doubled the heating rate of wires compared to using the data sheet maximum current with no change to cooling rate, resulting in a maximum actuator rotational velocity of approximately 100°/s over a 60° range of motion.

SMA actuators have two major drawbacks. The first drawback is the actuator's reliance on temperature to exert force. Wires can be quickly heated, but cooling, which usually relies on convection with ambient air, is usually slower than heating [29]. This results in a system that heats much faster than it cools, leading to a large imbalance between contraction and extension speed. Some works have experimented with water-based cooling [38, 39], but their increased mass removes their mass advantage over other actuators.

The second drawback to using SMA actuators is their complex, non-linear response. As the actuator undergoes a phase change, mechanical properties such as the shear modulus and resistance change [40, 41, 42]. While under external loading, wire

temperature increases, further complicating the actuator modeling [43]. These drawbacks mean that SMA actuators generally require feedback controllers to be applied effectively.

2.3 SMA Actuator Control

The control of SMA actuators is a complex task due to their transformation hysteresis, difficulty in heat transfer modeling, and nonlinear behaviour. A wide range of control methods, including sliding mode control, [25, 35], PID [10, 25, 35], adaptive control [25, 44], backstepping control [14], and model predictive control [45, 46, 47] have been applied to SMA actuators.

PID control is the most common controller applied to SMA actuators and does not require a model of the system. This is particularly beneficial for SMA actuators, which have states that either cannot be measured outside of a laboratory or are difficult to measure (temperature, resistance, martensite fraction, etc). PID controllers avoid this issue because any state that can be measured (such as joint angle) can be chosen instead of internal states. These controllers have been applied to robotic arms [7, 25, 44], linear actuators [10], and soft robotic arms [35].

A PID controller has also been applied to design a large, high-strength SMA actuator [10]. The controller was capable of linear and angular positioning within an error of ± 0.004 in and 1°, respectively. The actuator performed with minimal error under significant mechanical loading that corrected in less than one second.

Sliding mode control is also applied to several SMA actuators. This mode of control requires a model of SMA wire transformation, but is robust to modeling errors. It is used in [44] to design and simulate a lightweight, 1-DOF robotic arm based on a nonlinear dynamic model. The model integrates SMA heat transfer, phase transformation, and constitutive models with robotic arm kinematic and dynamic models. The design of the arm weighs only 48 g and is modeled to be able to lift 500 g with a 15 cm long arm. Another paper uses an adaptive sliding mode control to control the position of a needle tip in a medical device and found that the adaptive sliding mode controller performed better than PID control [48].

Model predictive control simulates future behaviour to determine the optimal control inputs for the controlled system based on a provided objective function. Model predictive control has been applied to control the position of an SMA actuator in simulation, which found that it resulted in lower steady-state errors than variable structure control [46]. A similar controller was validated experimentally and compared

to a PID controller, which it outperformed [45]. The transformation of SMA wires is approximated using an artificial neural network in [47], which is then applied to position control of a spring bias actuator.

Backstepping control algorithms begin with a desired behaviour, such as acceleration, and then calculates the required inputs using a series of subsystem models. This model-based algorithm has been applied to a simulated SMA actuator to determine the required voltage across the actuator based on a desired applied force [14]. It compares two approaches for the algorithm, then applies it to a 1-DOF robotic arm, which was modeled in MATLAB/Simulink for verification. However, the lack of experimental verification does not verify the system's robustness to modeling errors. This method requires significant advances to be used experimentally, as simulations of this method were not found to be robust to errors in the estimation of the heat transfer coefficients.

Multi-level controllers apply impedance control to allow for compliant behaviour. Impedance controllers simulate a spring-mass damper at each joint with a desired stiffness, then determine the torque required for the robotic system to match the simulated system. This is difficult to apply to SMA wires due to the complex nonlinear model that describes their behaviour and the difficulty in measuring the stress of the wire. Impedance controllers require a low-level force or torque controller to drive the actuator to the torque required by the impedance controller. This type of low-level force control has been achieved using load cells for feedback position control of an SMA actuator [13, 15]. A similar low-level controller was used in an impedance controller for an SMA spring-actuated rotary joint that directly measured the SMA wire force using load cells [11]. It was able to drive a joint to a desired angle, but no measurements of torque to validate the impedance controller were provided and experiments were not conducted under load. For an impedance controller to be extended from a single actuator to a robotic arm under load, a more thorough investigation of controller performance must be conducted. Impedance control has also been applied in simulation for a 1-DOF, spring bias joint designed for an exoskeleton [12]. It applied a "bang-bang" low-level controller and investigated three simulation case studies with varying impedance. This project does not employ feedback control and instead predicts wire stress using a common SMA model. Due to a lack of experimental validation, it is unknown how large prediction errors would be using this technique.

2.4 SMA-Actuated Robotic Arms

Research in designing manipulators with SMA actuators has created prototypes with a wide range of complexity and application. The simplest prototypes are simple grabber-style manipulators, which are not capable of moving on their own but can interact with the environment [36, 49, 50]. The prototype developed in [36] places SMA wires within silicone tubes embedded within a polymer to create a flexible, curving actuator controlled by a quasi-static model. The actuator achieved a maximum bending angle of 143°. The actuator was then implemented in a triangular and an antagonistic gripper, which were both tested on various objects. Both grippers were able to grasp a wide range of objects with different shapes and masses up to 2 kg. The triangular gripper was installed as the end-effector of a robotic arm and used to pick up, move, and place a soft drink can. The flexible gripper developed in [49] spools the wires over a series of rollers to reduce gripper size for use on a snake robot. The gripper includes force sensors that are used for closed-loop control of clamping force. A different SMA-actuated gripper was designed to optimize two-way actuation by pre-treating antagonistically arranging SMA wires [50]. The actuator was heat treated such that one wire to return to a curved shape and one to a straight shape, resulting in higher speed actuation when compared with two straight wires.

The low mass of SMA actuators also makes them suitable for prosthetic applications. A range of prosthetic hands [51, 52], as well as hands with four [53] and three [54] fingers have been developed. These designs use tendon-based actuators, and often include multiple degrees of freedom per finger by installing the full length of the SMA wire within a wrist or lower arm. However, their extremely small size prevents the integration of joint position sensors, so these works are generally limited to open loop control or simple range of motion and strength testing.

Several works have developed SMA-based assistive devices to assist patients with elbow flexion [55, 56], wrist motion [57], and shoulder movements [58]. These works focus on the range of motion and strength of the assistive device, but generally do not apply a position or force-based controller.

The continuous nature of SMA actuators has been used to design fully flexible robotic arms [35, 39]. These flexible actuators have been applied to a soft robotic arm driven by three radially located SMA coils within a silicone sleeve. The arm segments bend continuously and implement hall effect sensors on the arm surface to determine its curvature, which is used to control the arm position. Each segment is able to angle itself in two dimensions, allowing for complex curved shapes when

multiple segments are linked. The arm is controlled by a PID controller, and various experiments in 1D and 2D bending are conducted. A similar flexible design has been implemented in a prototype neurosurgical robotic arm that used vision tracking of arm features for feedback control [39]. This design separates the arm from the actuators with stiff tendons, allowing the SMA springs to be water-cooled.

Other works design stiff robotic arms, although they are generally small and have few degrees of freedom. The simplest design is a single, SMA-actuated joint with a spring bias, as in [17]. This robotic arm has limited function given its single degree of freedom and one-directional actuation control. More advanced designs include a single joint with an antagonistic actuator and end-effector [25]. The work also models and prototypes an SMA-actuated robotic arm and performs a comparison of PID, sliding mode, and adaptive control methods. The prototype arm was able to achieve angular errors of less than 0.1° and manipulate a 60 g payload with an arm weight of 100 g.

A notable gap in SMA-actuated robotic arms appears when investigating control of multiple degrees of freedom. A 2-DOF, spring bias system has been developed to mimic the planar motion of a human shoulder and elbow [7]. This arm was used for path-following tests, but its low payload capacity and relatively high path-following errors limit its capability to complete more complex tasks. Two spring bias SMA actuators are similarly integrated into a small robotic arm to experimentally validate a variable structure controller [6]. However, the link lengths of 7 cm significantly limit the range of the arm, which is used for step response position tests.

2.5 State Estimation for SMA Systems

State estimation techniques estimate system properties that cannot be easily measured, such as wire temperature and stress. Wire temperature is particularly difficult to measure, as the very small size of wires makes attaching thermistors or thermocouples very difficult. Additionally, even detailed thermomechanical models of SMA wires result in large temperature, and therefore stress errors [59]. While the constitutive model of the SMA wire can calculate these values, small measurement or parameter setting errors can result in large errors in performance due to the actuator's high nonlinearity. The most common state estimation method is the Kalman filter [17], which can minimize these errors by measuring a state variable that is more easily measured and estimating the unmeasured states from the system dynamics and inputs.

A Kalman filter [17] has been applied to a rotary SMA actuator in simulation,

then expanded to an extended Kalman filter (EKF) [16]. Both methods measure the applied voltage and measured angular joint position to estimate the wire's stress, which is easily related to the actuator torque. However, the methods used in these papers have several limitations. First, the EKF was only applied to a simulation of the joint, making its performance in experimental applications unclear. Secondly, the model of the SMA actuator was not used for stress estimation. Instead, the stress of the wire is estimated from the joint dynamics. This means that the SMA wire is treated as a black box, which does not allow for extension to an antagonistic configuration. In an antagonistic configuration, the dynamics of the joint would only provide the difference in stress between the two wires, not the actual wire stress.

Another work estimated the states of a single spring bias actuator in simulation using an augmented extended Kalman filter (AEKF) [60], which included spring coefficients and a joint friction coefficient as unknown system states. This model, unlike the two discussed previously, did use the constitutive model of the SMA wire for stress estimation. However, this work did not demonstrate the system's efficacy experimentally.

Similarly, an EKF is applied to a simulation of a silicone coated SMA actuator in [61]. Unlike other estimators, it defines its state as the wire stress and heat transfer coefficient and applies it to an adaptive PID position controller. Extended Kalman filters have also been used for self-sensing applications [62]. This method observes SMA spring resistance instead of deflection, using the EKF to estimate spring temperature and stress. This method resulted in low estimation errors in simulation for a linear actuator.

Extended Kalman filters have also been used in works that do not estimate states specific to SMA wires (such as stress, temperature, and phase). Actuator angular velocity and acceleration were estimated from angular position measurements in [63]. This method did not use a dynamic model of the SMA wire or the actuator. Instead, it estimated angular velocity and acceleration using a forward Euler method and treated the SMA wire as unmodeled process noise. An unscented Kalman filter was also used to estimate joint velocity and acceleration in [64], which developed a motor-actuated assistive device with variable joint stiffness introduced by SMA springs. Simulated SMA spring stiffness is a variable used for the estimation of joint velocity, but SMA-specific states were not estimated. Since spring stiffness is not a function of the system states of motor and joint angular position and velocity, SMA dynamics do not appear in the state transition function. Similarly, an EKF combined with feedback linearization has been used for the position estimation of a

constant-stress SMA wire, [65], which achieved good experimental results. It models the SMA wire as a spring with stiffness dependent on the wire phase, which was modeled separately from the EKF. The inclusion of the estimator improved experimental performance, but this method requires constant stress that cannot be achieved in a robotic arm.

A different method used Time Delay Estimation applied to a sliding mode controller to control the angle of a rotary actuator [66]. This method does not require a model of the actuator and was able to accurately predict wire stress in simulation. It is important to note that all SMA state estimation to date has been on single wire, spring bias actuators, and without perturbations. Additionally, control of an SMA actuator using the estimated state has only been completed in simulation.

2.6 Non-SMA Robotic State Estimation

Most robotic arms do not use an observer or estimator to determine the torque applied at a joint, and instead calculate the applied torque via a servo or motor's current draw [67]. However, state estimation techniques are well established in robotic arm control. State estimation has been applied to estimate the external forces and torque applied to a robotic manipulator [68]. This estimator was validated experimentally using a robot with a force-torque sensor on its wrist and found that the estimator accurately predicted the applied wrench. A similar work is completed in [69], which also estimates the stiffness of an unknown material that the end-effector presses against. Kalman filtering techniques have been applied to a motor actuated arm to estimate joint torque and contact forces from only joint position measurements [70]. Other works have used a disturbance observer [71] or sliding perturbation observer [72] for similar force control of motor-driven arms. State estimation has also been used to estimate the force a muscle applies in the human body by measuring electrocardiogram signals from the muscle and measured arm position and velocity [73]. The prevalence of state estimation in motor-driven robotic arms highlights the importance of developing similar estimators for SMA-actuated systems.

2.7 Summary and Research Gaps

This literature review discussed shape memory alloy actuators, their control methods, and their use in robotic arms. Several gaps in the literature were identified and are highlighted here.

First, the size and degrees of freedom of existing SMA-actuated robotic arms remains extremely limited. Existing stiff arms have only one [16, 74] or two [6, 7] SMA-actuated DOFs, limiting the tasks these arms can complete. More specifically, a two-DOF robotic arm cannot control the position and orientation of an end-effector, making manipulation tasks impossible. Despite their low weight, their payload capacities cannot currently match that of a motor-actuated robotic arm. For SMA-actuated arms to be used for practical manipulation experiments, a stronger arm with more degrees of freedom is required.

Second, impedance control of SMA-actuated robotic arms has not been well explored. It has been completed in simulation for a spring-bias actuator [12], and for an antagonistic actuator with no load in [11]. This controller relies on load cell measurements for closed-loop control and discusses position, but not torque tracking results. Impedance control of multi-DOF robotic arms is important for robotic arms working in sensitive environments or with people, but work is required to achieve this with SMA-actuated robotic systems.

Finally, the state estimation of an antagonistic SMA actuator is identified as a research gap. While an extended Kalman filter has been used to estimate the states of an SMA wire in simulation [16], an EKF has not been applied to an antagonistic actuator. Importantly, this extension to antagonistic systems cannot use the same methodology as previous works [16, 17], which calculate wire stress from link dynamics. A new formulation must be developed to extend state estimation to antagonistic, and then multi-DOF, SMA-actuated systems.

Chapter 3

A Shape Memory Alloy Actuated Robotic Arm

3.1 Introduction

Aerial manipulation vastly broadens the applications of robotic systems by increasing mobility and range of a manipulator. Advanced aerial manipulators are often a meter or more across, making them unsuitable for applications in small spaces or near people. The mass of the manipulator, usually a robotic arm, is currently the limiting factor in the development of small aerial manipulators [2]. Several papers have worked to reduce the weight of robotic arms using techniques such as topology optimization [3, 4], but the mass of servo or motor actuators cannot easily be reduced and can comprise over half of an arm's mass [5].

Shape memory alloy actuators are a significantly lighter and stronger alternative to motor actuators, making them an excellent choice for aerial manipulators. SMA actuators also have advantages over other alternative actuators such as pneumatic soft actuators or electroactive polymers. Pneumatic actuators are capable of generating large forces and displacements [75], but require a supply of compressed air, usually a pump [76], adding to the mass of the system. Another alternative actuator, electroactive polymers, create a displacement by applying a voltage between two electrodes. They are often used for bending applications [77] and are capable of generating large displacements, but require much higher voltages and generate much lower forces than SMA actuators [78].

Despite their benefits, SMA-actuated robotic arms remain limited. Due to the lack of a multi-DOF arm capable of precise control, current SMA-actuated robotic

arms are unable to complete tasks common in robotic manipulation, as none have the required degrees of freedom for position and orientation control of a robotic arm. This restricts the field of SMA-actuated robotics from common aerial manipulation tasks, such as object grasping and manipulation, path following, and obstacle avoidance. A 3-DOF arm will enable experimental validation of controllers and path planning algorithms that address the unique behaviour of SMA actuators during these tasks.

To integrate SMA-actuated robotic arms into aerial manipulators, their strength must also be increased. Existing designs are only able to manipulate masses of roughly 75 g [7], which is lower than the mass of even lightweight active end-effectors in the literature [8, 9]. Unfortunately, their strength or range cannot be easily increased due to several restrictions including structural and size limitations. Firstly, existing designs cannot easily increase the number or strength of wires without suffering from structural failure, as no analysis has been performed on the load application of SMA actuators. Secondly, size restrictions of multi-wire SMA actuators must be considered. Existing designs for SMA bundle actuators are unsuitable for an aerial manipulator due to their inability to use rollers to increase their length. Improvements in SMA-actuated robotic arms require addressing both arm and actuator design limitations that remain unaddressed in the literature.

To resolve the need for a lightweight, high payload SMA-actuated arm, a 3-DOF, SMA-actuated robotic arm is developed. This chapter addresses the design limitations of SMA-actuated arms in several ways. First, the arm increases the degrees of freedom of existing arms by incorporating multiple actuators within each link. This enables the arm to simultaneously control end-effector position and orientation, which is essential for aerial manipulation tasks and has not been achieved with SMA actuators. Second, the payload capacity of the arm is increased with a design implementing many wires spooled around a series of rollers, making this the first SMA-actuated arm capable of manipulating common drone payloads. The increased complexity associated with these improvements requires a level of design analysis that has not been conducted in the literature.

In this chapter, the forward kinematics of the arm are calculated for a range of joint angles to find a suitable operating space. A static force analysis is used to calculate the required strength and size of the SMA actuators, which informs the geometry of the arm's components. The resulting actuator forces are applied to the arm's links using ABAQUS CAE's topology optimization tools [79] to reduce component mass, and component failure is simulated using the Tsai-Hill failure criterion. The components were 3D printed from a carbon fiber reinforced nylon filament and assembled

into the arm. Finally, an adaptive proportional-integral (PI) position controller was applied alongside a linear path planning algorithm with a trapezoidal velocity profile to a set of step response and path following tasks. The arm's unique design that contains multiple actuators within a single link allows for more degrees of freedom, and the actuator analysis and following topology optimization drastically increases the capability of the system. The resulting arm has over double the range and 25 times the torque of any existing SMA-actuated robotic arm, making it substantially more capable in completing future aerial manipulation tasks.

This chapter is structured as follows: In §3.2, an analysis of possible operating spaces is conducted and used to inform the actuator requirements in §3.3. The topology optimization is in §3.4, and a summary of the arm's assembly and system architecture is in §3.5. The arm's controller and path planning algorithm are described in §3.6 and the results and discussion are reviewed in §3.7, with some concluding remarks in §3.8.

3.2 Robotic Arm Analysis

Before SMA actuators can be designed for a robotic arm, the structure of the arm must be considered. The arm, shown in Fig. 3.1, has three coplanar degrees of freedom arranged in, which allows control of both the position of the end-effector within a plane and orientation relative to the base frame. The $\hat{X}$-axis is defined as parallel to the drone platform and ground (with positive to the right), and the $\hat{Y}$-axis is the positive vertical perpendicular to it. The first joint is on a mounting component to connect the arm and drone systems, while the second and third are separated by links 1 and 2. The third joint is a single component that allows for an end-effector to be mounted to it. To prevent overstrain of the SMA wires, physical stops are added to each joint.

Defining the desired link lengths and joint ranges of motion is particularly important for SMA-actuated robotic arms due to their limited actuation range, which is defined by the length of the wire. To define the operating space of the arm, the forward kinematics of the arm were calculated for a given range of angles. The result is the set of all points the arm's end-effector can reach as described in Eqs. (3.1) and (3.2), where L_n represents the length of a numbered link and q_n represents the angle of the numbered joint.

$$\begin{aligned} X = {} & L_1 \sin(q_1) + L_2 \sin(q_1 + q_2) \\ & + L_3 \sin(q_1 + q_2 + q_3) \end{aligned} \tag{3.1}$$

$$\begin{aligned} Y = {} & -(L_1 \cos(q_1) + L_2 \cos(q_1 + q_2) \\ & + L_3 \cos(q_1 + q_2 + q_3)) \end{aligned} \tag{3.2}$$

Figure 3.1 displays two different operating spaces for two ranges of joint angles for a potential design. Both operating spaces have the same magnitude of joint range, and thus require the same length of wire for each actuator. Each plot uses the link lengths $L_1 = 228.6$ mm, $L_2 = 203.2$ mm, and $L_3 = 25.4$ mm. The operating spaces are plotted as blue and red dots alongside a 0.4 m wide drone with joint 1 located at the origin, i.e., (0,0).

The selection of an operating space is specific to the application of the system. For an aerial manipulator, the shown operating space can be rotated about the vertical axis, so an operating space biased towards the manipulator's front or back is acceptable as the opposite side can be reached by rotating the drone base. The area of each operating space was calculated numerically, and the biasing of joint 2 increased the area of the operating space from 443.6 cm^2 to 897.2 cm^2, representing over a two-fold increase.

3.3 SMA Actuator Analysis

Shape memory alloys undergo a phase change from martensite to austenite when strained that is reversible when heated [29]. SMA wire actuators function by converting the linear force caused by their phase transformation to a torque by mounting the wires to a point offset from the link's rotational axis. Each actuator can only exert force in one direction, so a restoring force is required, usually in the form of a bias spring or a second antagonistically arranged wire, as shown in Fig. 3.2. The use of a bias spring introduces an additional constraint, as its applied force is coupled to the wire strain. This results in a reduction of maximum force near the actuator's maximum angle, where a larger spring force must be overcome. An antagonistic configuration must overcome the minimum force to stretch the passive wire, but this force remains constant along the joint's range of motion. An antagonistic configuration was

chosen for this design due to its higher activation frequency and precision [44] when compared to a bias spring, as well as for the constant and lower force required to stretch the passive wire.

In an antagonistic configuration, each actuator rotates one joint by pulling on a circular feature that maintains a constant radius such that the resulting torque is constant for all angles. The use of an antagonistic configuration introduces the possibility of asynchronous actuation depending on the rate of heating and cooling of the wires when switching direction of motion. This behaviour can be observed in Figure 3.2, where the offset time between the two wires transforming in opposite directions is shown by the red and blue highlighted areas. The highlighted regions represent time when temperature is between A_s and A_f, representing forward transformation, and M_s and M_f, representing backwards transformation. If one wire cools slowly and the other heats quickly, the antagonistic wire will temporarily increase wire tension until

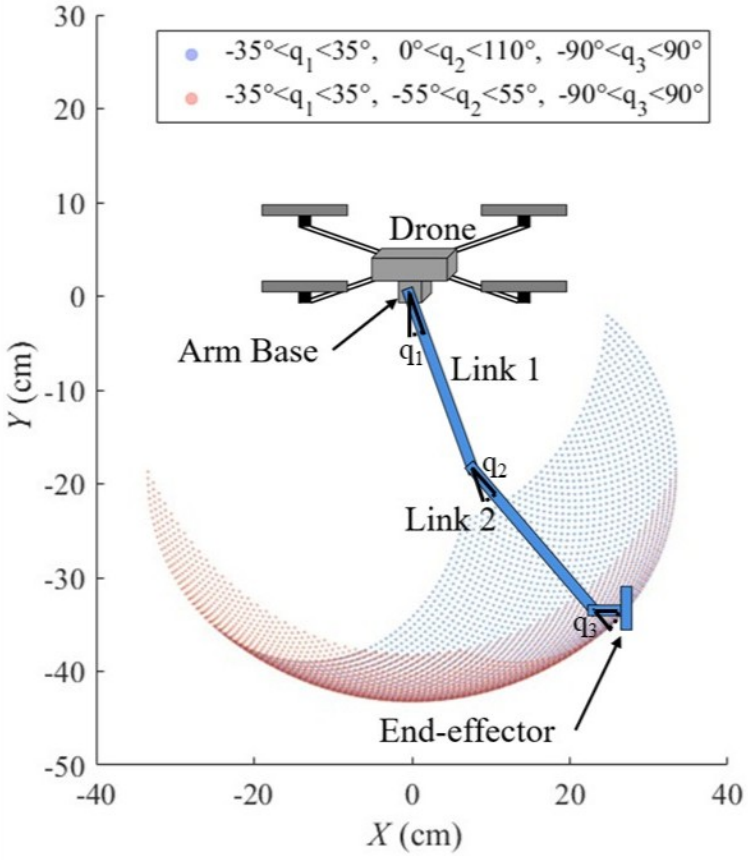

Figure 3.1: Two operating spaces with the same magnitude of joint ranges. The biased operating space (blue) is significantly larger than the unbiased operating space (red).

motion can begin, reducing the response time of the actuator. This effect is limited in this work by the smooth paths generated by the path planning algorithm and relatively fast cooling of the wire, as summarized in Table 3.1. This behaviour could be further limited using active cooling methods such as forced air convection [29]. Conversely, if one wire cools quickly and the other heats slowly, it is possible for slack to be introduced into the wire. A pre-tensioning mechanism could be used to prevent slack, but this project reduces mechanical complexity by ensuring that the wires are heated quickly enough to prevent wire slack.

Next, the type, number, and length of wire are selected. Flexinol brand wires were chosen due to their low cost, commercial availability, and their prevalence in existing literature [29]. The diameter of the wire controls the force and cooling time, with thicker wires producing larger forces but requiring more time to cool. A 0.25 mm diameter wire with an activation temperature of 90°C is the thickest available wire that cools within an acceptable length of time, in this case 4.5 s [29]. Thicker wires would simplify the design by reducing the number of required wires, but would increase actuation time and would not have a safe maximum current. Table 3.1 summarizes the properties of the chosen SMA wire.

The SMA wires were grouped together to create bundle actuators, which use many wires in parallel to increase actuator force while maintaining favorable thermal characteristics compared to using a single, thicker wire. Bundle actuators with as many as 48 wires have been created [10]. Increasing the number of wires within a bundle increases the maximum force of the actuator, but requires more space, power, and a stronger structure. The thermal characteristics of the bundle depend on the wire spacing, as higher spacing allows for faster cooling.

To determine the number of wires, N_w required for an actuator in joint n, and the radius of the component they pull on, r_n, a static analysis of the required joint torque was performed. The maximum torque generated by each actuator, $\tau_{a,n}$, is a function of the number of wires, N_w, the wire cross sectional area, A_w, the maximum wire stress, $\sigma_{w,\max}$, and r_n, as described in Eq. (3.3). A maximum stress of 172 MPa was used as recommended by the supplier [29], which results in a force that can be applied by the wire throughout its range of motion.

$$\tau_{a,n} = N_w \sigma_{w,\max} A_w r_n \tag{3.3}$$

The maximum actuator torque, $\tau_{a,n}$ must be greater than or equal to the static torque exerted by the mass of the arm and end-effector, denoted at joint n as $\tau_{m,n}$.

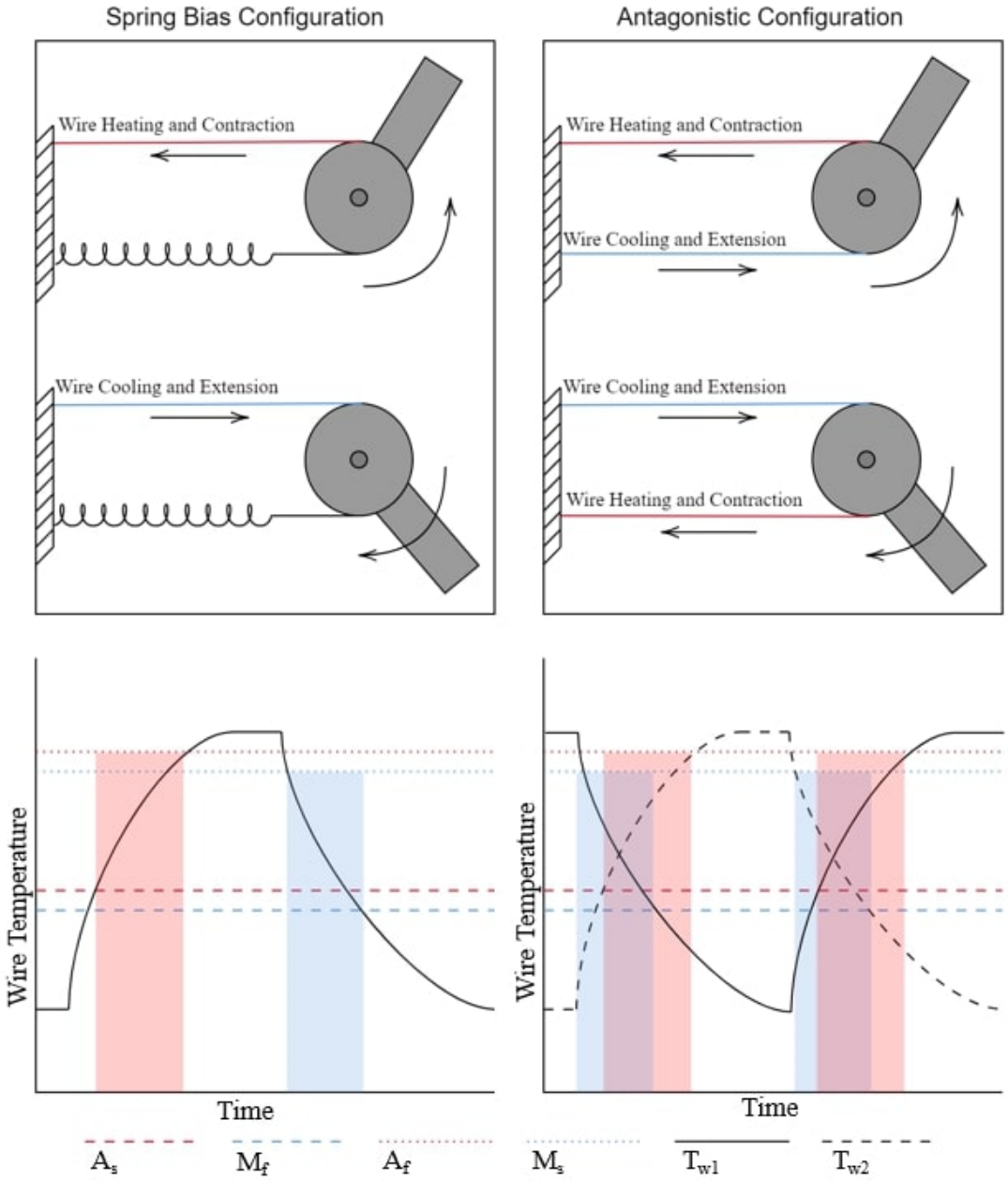

Figure 3.2: Comparison between spring bias and antagonistic configuration for an SMA actuator (above). Temperature versus time plots for a spring bias and antagonistic configuration (below). Areas of heating and contracting are shown in red, occurring when wire temperatures T_{w1} or T_{w2}, for wire 1 and wire 2, respectively, are between Austenite start and finish temperatures, A_s and A_f. Areas of cooling and biasing are shown in blue, occurring when T_{w1} or T_{w2} are between Martensite start and finish temperatures, M_s and M_f. Areas highlighted in both red and blue indicate simultaneous cooling of one wire and heating of the other.

Table 3.1: SMA Wire Properties

Property	Value
Diameter (mm)	0.25
Activation Temp. (°C)	90
Recoverable Strain (%), ϵ_{max}	4
Maximum Stress (MPa), $\sigma_{w,max}$	172
Resistance (Ω/m)	18.5
Safe Current (A)	1.05
Expected Cycles	10^5
Min. Heating Time (s)	1.5
Max. Cooling Time (s)	4.5

The static torque $\tau_{m,n}$ is a function of link mass, m_n, and the horizontal distance between the center of mass and the joint, d_n, as described in Eq. (3.4).

$$\tau_{m,n} = \sum_{i=1}^{n} m_i d_i \tag{3.4}$$

Several trade-offs must be made in the selection of r_n and N_w. Increasing the number of wires increases the actuator torque, but also requires more space and results in higher power consumption. Increasing r_n also increases actuator torque, but requires proportionally longer wires. A full design analysis of this actuator is beyond the scope of this chapter and so the decision making process is limited to finding any combination of these values that does not violate the torque limit and results in geometry that can be reasonably accommodated within the arm.

The value of d_n is determined by finding the maximum distance in the X-axis using forward kinematics, described in Eqs. (3.1) and (3.2). An assumption is made that the mass of each joint is concentrated at the geometric center of the link. As a first approximation, $m_1 = 300$ g, $m_2 = 100$ g, and $m_3 = 300$ g. A set of values for N_w and r_n were selected to satisfy the constraint that $\tau_{a,n} > \tau_{m,n}$.

The actuator design was limited to strain the wires by 4% or less, which is within the safe repeatable range for the wires [29]. The minimum wire length, L_w, for the desired range of motion between angles $q_{\min}$ and $q_{\max}$ in radians and maximum strain $\epsilon_{\max}$ is calculated using Eq. (3.5) and summarized in Table 3.2.

$$L_w = \frac{(q_{\max} - q_{\min}) r_n}{\epsilon_{\max}} \tag{3.5}$$

Since the required wire length is much longer than the length of the links, the

Table 3.2: Actuator Parameters

Joint No.	r_n (cm)	N_w	L_n (mm)
1	2.54	6	775.5
2	1.28	7	669.9
3	0.57	3	447.5

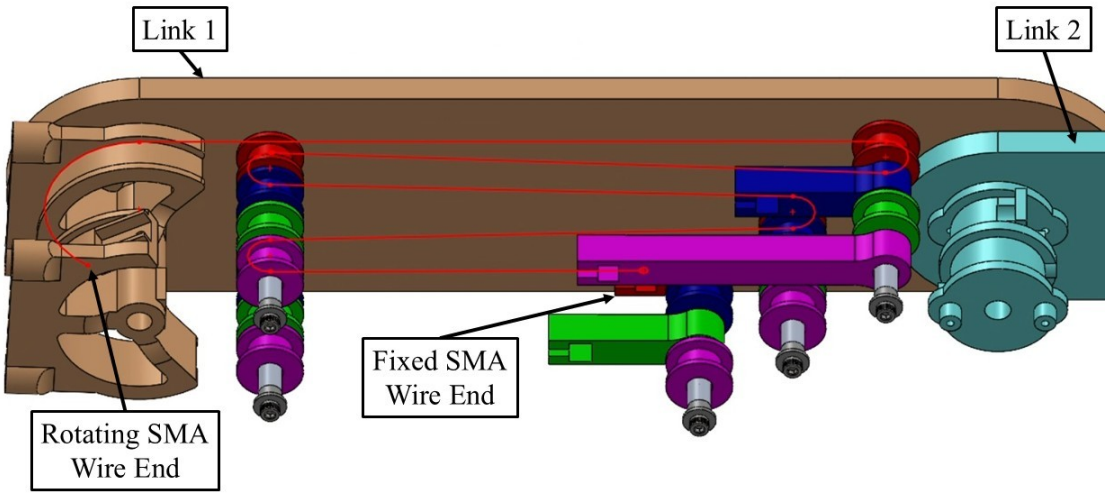

Figure 3.3: Link 1 assembly showing link 1 and 2 components, wire rollers, and fixed wire ends. The path of the joint 1 counterclockwise (CCW) actuator is shown in red.

wires must be wound around pulleys several times. These pulleys are mounted on aluminum internally threaded connecting rods that also serve to connect the two sides of each arm link, enclosing the actuators and supporting them from both sides. The two halves are connected by bolts and washers threaded into the connecting rods. Figure 3.3 shows this structure and highlights the path of the joint 1 counterclockwise (CCW) actuator. Figure 3.4 similarly displays the path of the joint 2 counterclockwise actuator. Each actuator consists of four rollers, one mounting component, and the rounded termination blocks used to convert wire force to joint torque.

Contact between wires of different actuators would result in a short circuit, increasing the current flowing through the wire and quickly overheating it. Contact is prevented by thin sheets of 3D printed PAHT-CF filament supplied by Bambu Lab separating the actuators. Contact of wires within the same actuator would not result in a short circuit, as the same voltage is applied over all wires within the same actuator. As shown in Figure 3.5, multiple SMA wires are arranged horizontally and are electrically in parallel. A set of wire separators (shown in pink), placed along the length of the actuator, prevent the tangling of wires. This design is distinct from

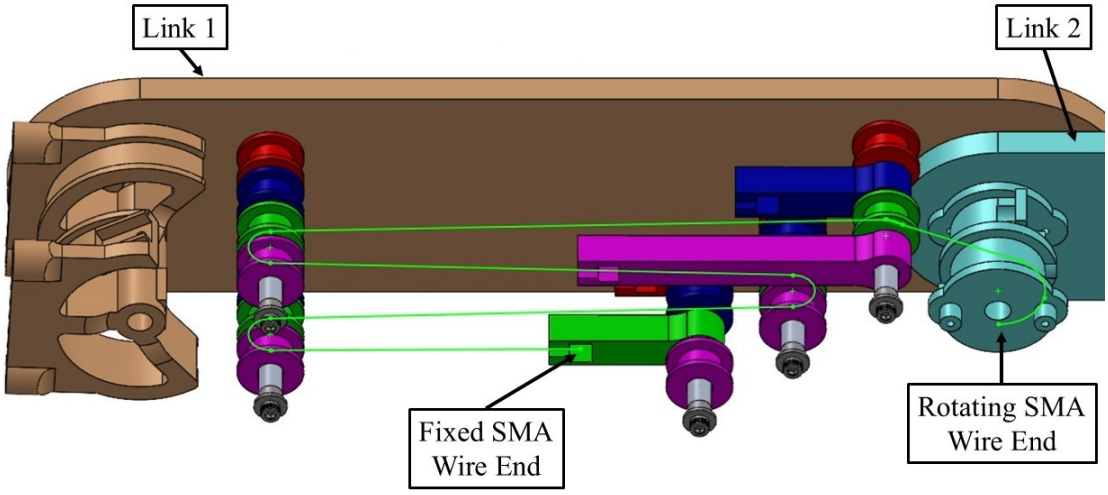

Figure 3.4: Link 1 assembly showing link 1 and 2 components, wire rollers, and fixed wire ends. The path of the joint 2 counterclockwise (CCW) actuator is shown in green.

many existing bundle actuators, which arrange SMA wires in a circle. While a circular bundle can fit more wires in a smaller space, they are generally constrained to linear wire motion without pulleys, resulting in large actuators unsuitable for mobile robotic applications [10]. Wires are kept at a distance of 1.2 mm from each other,

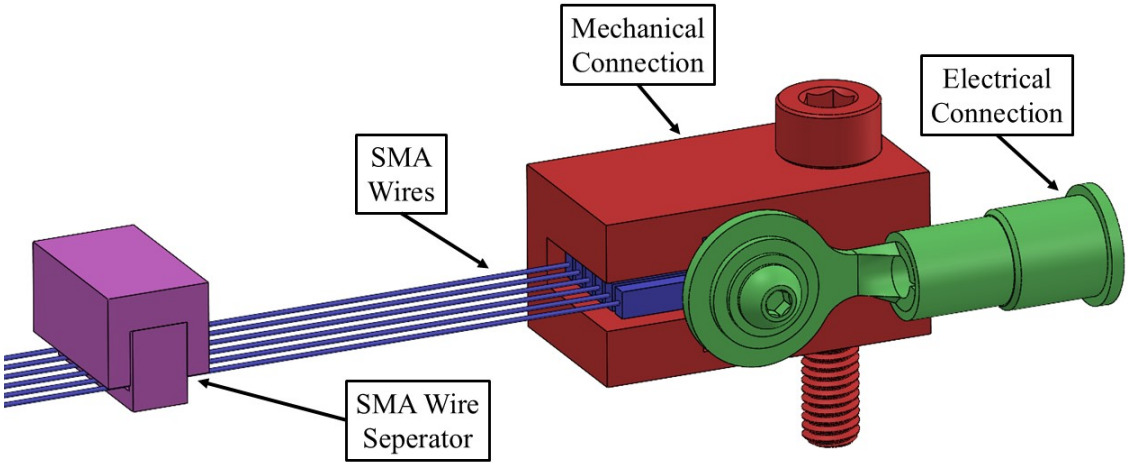

Figure 3.5: SMA actuator subassembly showing electrical connection (green), mechanical connection (red), SMA wires (blue), and SMA wire separators (pink)

nearly 5 times the diameter of the wires themselves. Because of this large spacing ratio, each wire is unlikely to impact the heating and cooling of other wires.

Finally, the fatigue of the SMA actuator must be taken into account, as functional fatigue of the wire can reduce the recoverable strain over many cycles. This reduction is a function of applied wire stress, temperature, and applied strain [29, 80]. This type of fatigue is not well understood in the literature, and no general model for the number of cycles expected from a particular design currently exists. A full fatigue analysis of the SMA wire is beyond the scope of this chapter, but guidelines from the supplier and the literature can be used to inform expected actuator life. Functional fatigue of this wire cycled at 138 MPa of stress was observed to be less than 1% over 10^5 cycles [29]. While this study uses a maximum stress of 172 MPa, this limit is only reached at a single point in each joint's range, and the overwhelming majority of cycles will be at a stress under 138 MPa. Similar guidelines of 10^5 cycles have been used elsewhere in the literature for NiTi based SMA wires [81]. Fatigue of the wires is also limited by supplying current at only 75% of the maximum current to prevent overheating, physical stops to prevent wire overstrain, and limiting wire strain to 4% strain, which is significantly less than the maximum recoverable strain of 8% that is available to NiTi SMA wires [29]. The impact of actuator fatigue could be further limited using pre-conditioning cycles, then using the conditioned length as the new nominal wire length [29, 40]. Unless each joint is consistently operating under the maximum torque scenario (i.e., full load capacity and at full horizontal extension), the expected functional fatigue of the SMA wires are anticipated to remain less than 1% over 10^5 cycles.

3.4 Topology Optimization

To reduce the mass of the arm and ensure its structural integrity under the applied loads, topology optimization techniques were applied. Topology optimization is a process in which material is iteratively removed from a base design to minimize the value of an objective function. The result of the process is an optimized lightweight part. Topology optimization has been applied to various robotics projects, usually to larger components such as the links of a robotic arm [4, 82]. This technique is well-suited for SMA-actuated robotics due to the high compressive forces applied by SMA wires within a structure that are further increased when using rollers to increase wire length.

The two halves of each arm link were identified as the largest components of the

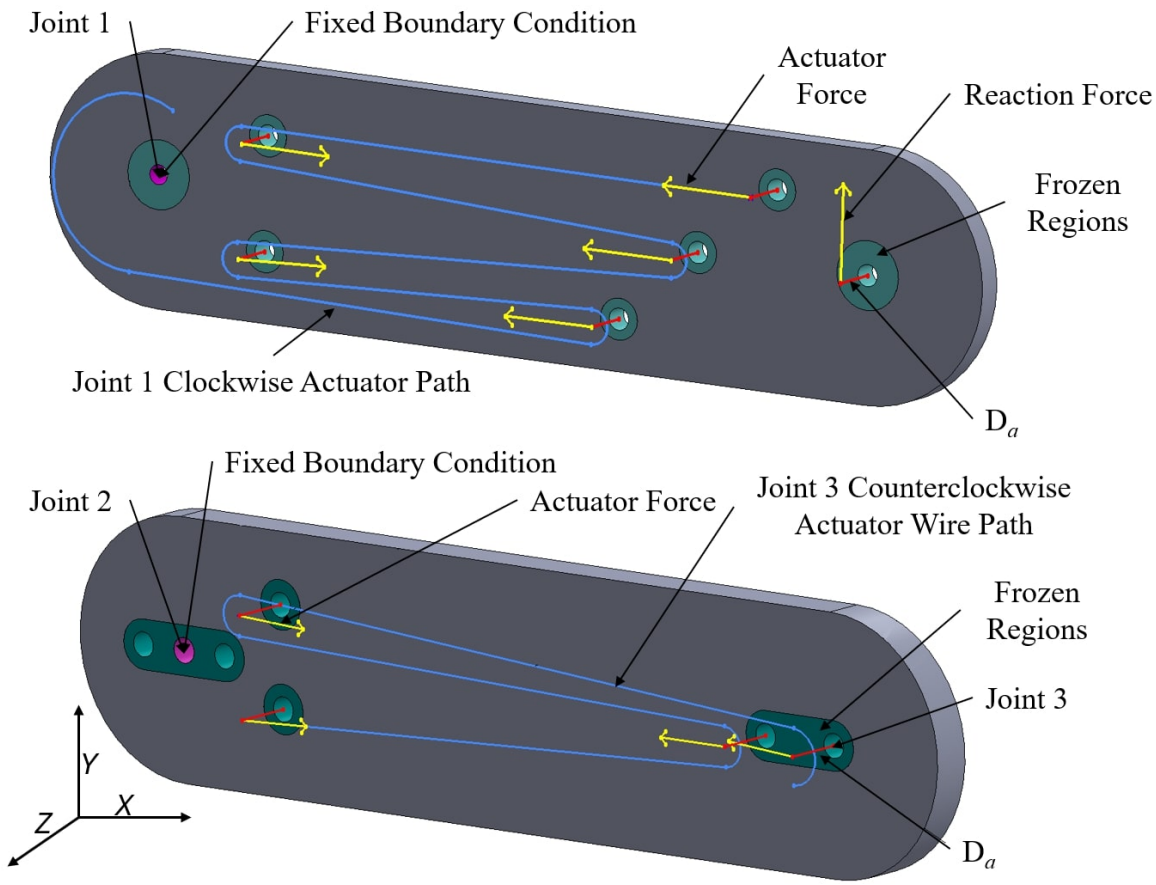

Figure 3.6: Optimization setup for links 1 and 2. Frozen regions excluded from optimization are shown in turquoise, the fixed boundary condition is shown in pink, actuator and reaction forces are shown in yellow, D_a is in red, and wire path for the joint 1 clockwise actuator and joint 3 clockwise actuator are shown in blue.

structure, and, thus, the components that would benefit most from optimization. The optimization problem was simplified by assuming symmetrical loading between the two halves of each arm link applied at a distance in the Z-direction beyond the points where rods connect the two halves, as shown in Fig. 3.6.

The forces F_x and F_y and moments M_x and M_y applied by the actuators at each load point at angle θ_w and distance D_a were calculated using Eqs. (3.6), (3.7), (3.8), and (3.9).

Table 3.3: PAHT Carbon Fiber Reinforced Filament Mechanical Properties [83]

X_{11} (MPa)	X_{22} (MPa)	X_{12} (MPa)	E_1 (GPa)	E_2 (GPa)	G_{12} (GPa)	ν (-)
92	47	125	3.86	2.18	4.23	0.25

$$F_x = N_w F_w \cos(\theta_w) \tag{3.6}$$

$$M_x = F_x D_a \tag{3.7}$$

$$F_y = N_w F_w \sin(\theta_w) \tag{3.8}$$

$$M_y = F_y D_a \tag{3.9}$$

For link 1, five load cases were considered—four cases each with one actuator applying its maximum torque and one case with all actuators applying maximum torque. Each case also includes a force at the next joint creating static equilibrium. The final load case is an unlikely edge case, as two antagonistically configured actuators would not be activated at the same time, but was considered in the case that both actuators were momentarily at their maximum stress. For link 2, three load cases were considered in the same manner as link 1.

A material profile to match the carbon fiber reinforced filament material properties was created [83]. The 3D printed material, which was printed using 100% infill, can be modelled as a transversely isotropic material. The material orientation was set such that a single 3D printing layer is on the X-Y plane as defined in Fig 3.6, as this is the plane intended to experience the smallest amount of bending. X_{11}, X_{22}, and X_{12} values represent the strength of the material under tensile, transverse, and shear stress, while E_1, E_2, and G_{12} represent the corresponding moduli of elasticity and shear modulus, and ν represents Poisson's ratio. These material properties were provided by the supplier's technical data sheet [83] and are summarized in Table 3.3.

Each link was imported into ABAQUS CAE [79] and partitioned to create a cylindrical section to be frozen around each connecting rod and joint. Tetrahedral elements with an average size of 1 mm were used. While the applied loads are in static equilibrium, a boundary condition to prevent rotation and translation of the arm was imposed on the upper joint of the link.

Table 3.4: Topology Optimization Process Parameters and Results

	Link 1	**Link 2**
Mesh Parameters		
Average Mesh Element Size (mm)	1	1
Number of Mesh Elements	125664	195180
Initial Volume (mm^3)	115203	178649
Frozen Volume (mm^3)	9490	6961
Objective Function Constraints		
Volume Limit (mm^3)	0.15	0.035
Displacement Limit (mm)	5	N/A
Minimum Member Size (mm)	20	10
Maximum Member Size (mm)	30	30
Objective Function Parameters		
Displacement Weight	0.4	0
Strain Energy Weight	0.2	1
Von Mises Stress Weight	0.4	0
Results and Post-Processing		
Pre-Opt Mass (g)	122.1	189.4
Post-Opt Mass (g)	26.9	13.7
Final Mass side 1 (g)	29.1	18.2
Final Mass side 2 (g)	28.7	20.5
Percent Reduction side 1 (%)	76.2	90.0
Percent Reduction side 2 (%)	76.5	89.2
Optimization Cycles	150	93
Maximum Tsai-Hill Value	0.71	0.4

The forces and moments generated by each actuator are applied to a reference point that is pinned to the inner face of each hole. This represents the rod that connects the two halves of the link, which transfers force from the actuator to the links. This assumes that the connecting rods do not deflect under the actuator force, which is reasonable, as they are made from aluminum and have a diameter of 0.25 in.

Excessive stress and deformation in initial optimization tests of link 1 required a modification of the objective function to decrease maximum stress and maximum displacement of the link. Von Mises stress was selected as an optimization parameter due to software restrictions within ABAQUS. Von Mises stress is not an accurate indicator of composite failure, but is suitable as an intermediate step during optimization. After optimization, the Tsai-Hill method [84] was used to verify the optimization results. The parameters of the topology optimization process are detailed in Table 3.4.

Further analysis of the resulting part was completed to ensure the part would not fail under load using the Tsai-Hill failure method. This method combines tensile,

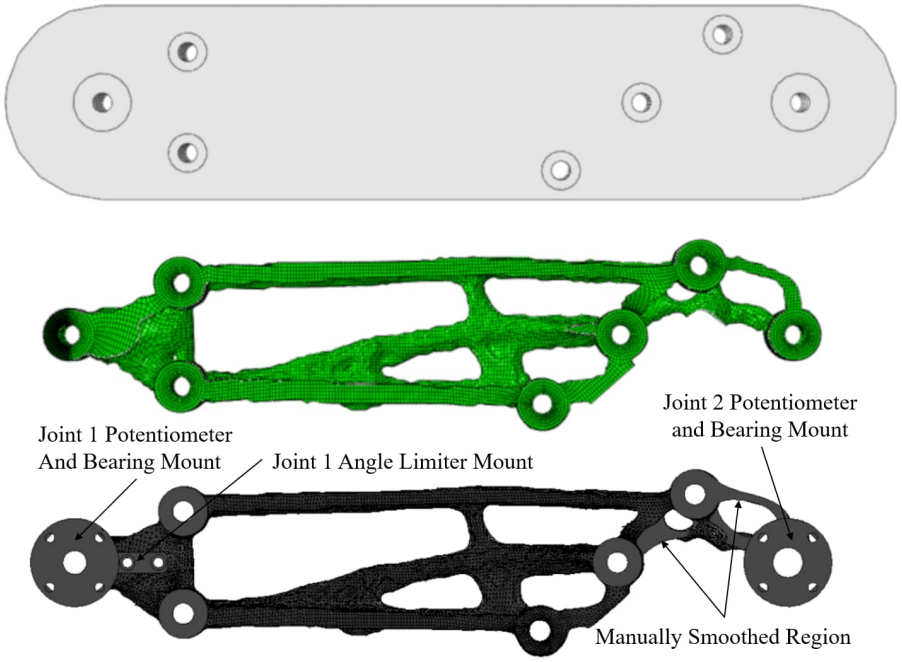

Figure 3.7: Link 1 pre-optimization (top), post-optimization (middle), and post-processed (bottom)

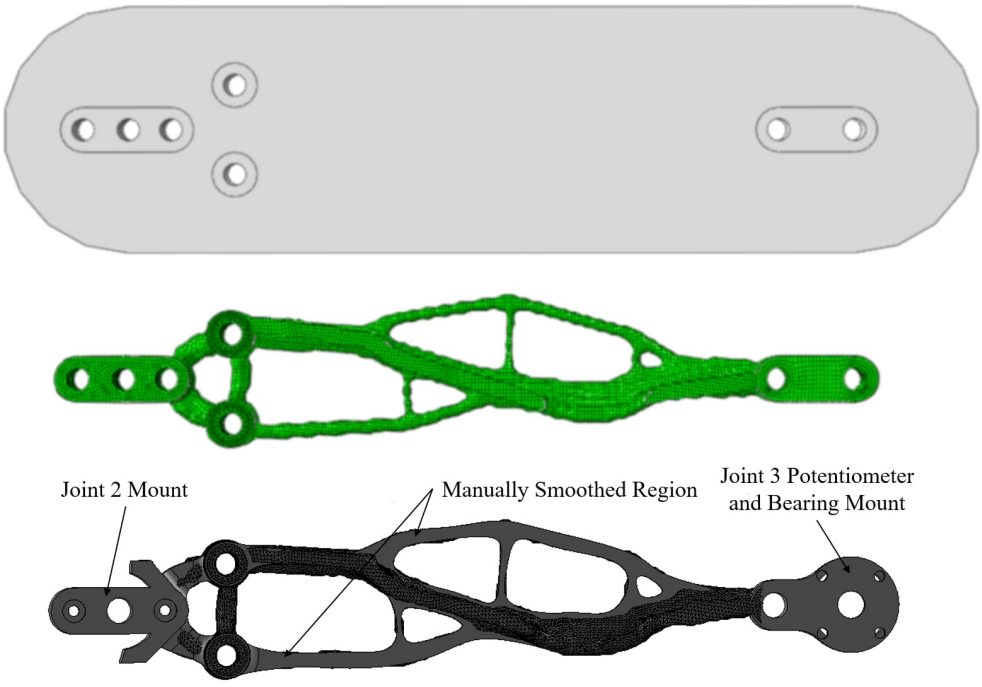

Figure 3.8: Link 2 pre-optimization (top), post-optimization (middle), and post-processed (bottom)

shear, and transverse forces simultaneously, as shown in Eq. (3.10) [84], where σ_{11} is the intra-layer stress, σ_{22} is the inter-layer stress, and τ_{12} is the shear stress, all of which are defined in Eqs (3.11), (3.12), and (3.13). The variables X_{11}, X_{22}, and S_{12} are material properties defined in Table 3.3. In Eq. (3.10), a mesh element returning a value greater than or equal to one indicates failure of the part.

$$\left(\frac{\sigma_{11}}{X_{11}}\right)^2 - \frac{\sigma_{11}\sigma_{22}}{X_{11}^2} + \left(\frac{\sigma_{22}}{X_{22}}\right)^2 + \left(\frac{\tau_{12}}{S_{12}}\right)^2 \geq 1 \tag{3.10}$$

$$\sigma_{11} = \sqrt{\sigma_x^2 + \sigma_y^2} \tag{3.11}$$

$$\sigma_{22} = \sigma_z \tag{3.12}$$

$$\tau_{12} = \sqrt{\sigma_{13}^2 + \sigma_{23}^2} \tag{3.13}$$

Across all load cases, the maximum Tsai-Hill value was 0.71 and 0.4 for links 1 and 2, respectively; both of which are well under the value of 1 that indicates failure. Fatigue analysis of the components was not considered due to the complexity of fatigue modelling of nonisotropic materials, which is beyond the scope of this chapter.

After ensuring that the parts are under their stress limits, parts were smoothed in preparation for 3D printing. Each link was smoothed in MeshLab [85], a free mesh processing software. A 15-cycle scale-dependent Laplacian Smooth [86] was used for link 1, while a 10-cycle Taubin Smooth [87] was used for link 2. Different smoothing algorithms were found to produce the best results due to the different feature sizes of the arm links. After smoothing, the mesh was imported into SolidWorks [88], where features were added to enable assembly. Flat faces on the sides of the links and cylindrical features in frozen regions are used to attach connecting rods and bearings. Bolt holes for joint potentiometers and angle-limiting features complete the assembly and prevent wire overstrain.

The optimization process resulted in significant mass reduction of the arm links. In total, mass of the links was reduced by 526.5 g (85%). A breakdown of the starting and final component masses is shown in Table 3.4. This is a significant mass reduction that will increase the flight time and reduce the required thrust of the drone it will be implemented on in future work.

3.5 Experimental Setup

This section details the arm assembly and system architecture, compares the arm to existing SMA-actuated robotic arms, and defines the tests conducted in §3.7.

3.5.1 Arm Configuration and Mass

After the arm link halves were optimized, the links were assembled into the arm structure. A base component, passive end-effector, and connecting rods were added. Actuators were separated by thin 3D printed panels to prevent short circuits.

A passive end-effector was selected for its low mass and simplicity. It is capable of picking up and moving small masses using a hook. A CAD model of the arm on its test stand is shown in Fig. 3.9, and an image of the assembled arm in Fig. 4.2. Before assembly, all parts were weighed to evaluate the arm's mass distribution and their masses are included in Table 3.5.

The assembled arm weighs only 399 g, and 546.3 g including electronics, which is significantly lower than the mass of similar lightweight aerial manipulators [82], and can manipulate masses nearly its entire weight. Shafts and bearings made up the largest portions of the arm mass and could be further reduced by only including shafts for a short length on the outer ends of each component and using lightweight bushings instead of bearings. The SMA actuators, including rollers, compose only 10.8% of the arm's mass, which is much less than that of servo-actuated arms [5].

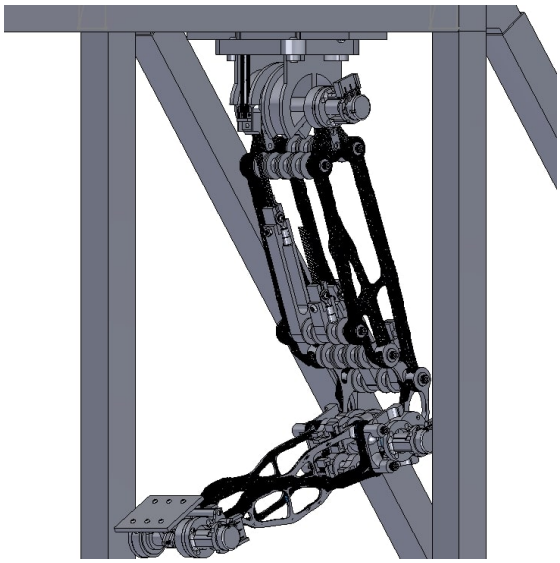

Figure 3.9: Arm CAD model, including electronics box and test stand structure

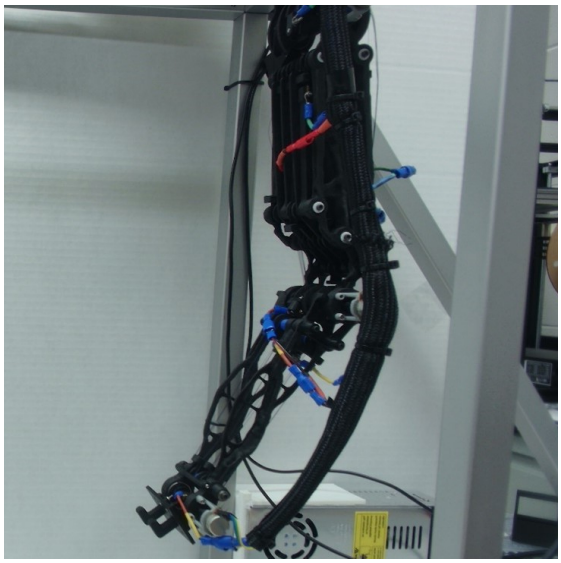

Figure 3.10: Image of the robotic arm with a passive end-effector

Table 3.5: Arm Mass Breakdown

Mechanical Structure	**Mass (g)**	**Mass (%)**
Optimized arm links	96.5	17.7
Base	33.6	6.2
End-effector	10.8	2.0
Joint limiters	6.0	1.1
Potentiometers	43.5	8.0
Connecting rods	40.5	7.4
Shafts and bearings	97	17.8
Nuts and bolts	27.8	5.1
SMA wires	6.9	1.3
SMA wire rollers and connectors	36.4	6.7
Structural subtotal	**399.0**	**73.0**
Electronics		
Electrical Connectors	24.72	4.5
Microcontroller	25.0	4.6
MOSFETs	41.22	7.5
Electrical Wires	44.9	8.2
Wire Sheath	11.5	2.1
Electronics subtotal	**147.3**	**27.0**
Total mass	**546.3**	**100.0**

3.5.2 System Architecture

The system architecture was designed in accordance with the schematic shown in Fig. 3.11. First, a set of desired waypoints is provided to the computer and are used to calculate the required joint angles at a given timestep. The desired joint angles are then sent to an Arduino Uno at a rate of 20 Hz. The Arduino outputs a pulse width modulation (PWM) signal to three of the six MOSFET circuits as defined by the adaptive PI controller, which switches power between the clockwise and counterclockwise actuators. The MOSFETs, supplied by LGDehome, increase the voltage of the PWM signal using the 12 V, 30 A power supply supplied by Anbull, applying the desired current to each actuator. Closed-loop control is achieved by measuring joint angles with a 20 kΩ Taiss brand potentiometer (part number WH148) secured to the shaft of each joint and recorded using the Arduino Uno microprocessor.

3.5.3 Arm Comparative Analysis

To highlight the difference in performance between this and other existing SMA-actuated arms and its suitability for aerial manipulation, a comparison was performed using

two metrics. A one-to-one comparison between arms is difficult, as they vary in size, strength, and degrees of freedom. Furthermore, comparison between the developed arm and traditional aerial manipulators is difficult as most papers do not publish the mass or maximum torque values of the manipulator. This arm is also significantly larger than existing arms, resulting in larger required torques to manipulate the same mass. Therefore, the ratio of the arm's maximum joint torque to mass was used as a point of comparison, as it encompasses the arm mass, payload capacity, and range. The actuator torque used in the first joint of each arm, as calculated from the theoretical strength of the actuator, is used for each case. This value does not account for the mass of the arm link the actuator provides torque to, so the mass of the arm is listed separately. The comparison, summarized in Table 3.6, shows that this arm is 25 times stronger and has a torque-mass ratio 8 times higher than the strongest existing SMA-actuated arm.

Secondly, the operating space of several SMA-actuated robotic arms were compared and are plotted in Fig. 3.12. This comparison shows the operating range of each arm as though their first joint was placed at the base of a drone, and includes both the theoretical and measured range of motion of this robotic arm. The developed arm is notably more capable of manipulation at range, which is important for manipulation tasks in front of a drone while maintaining clearance between the drone rotors and the object to be manipulated. The discrepancy between the measured (red) and

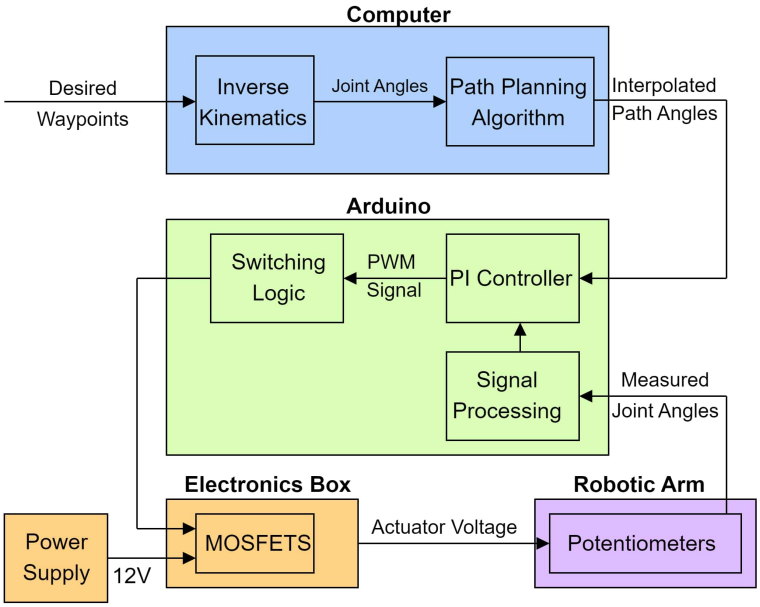

Figure 3.11: System architecture of the arm showing signal paths between computer, microcontroller (Arduino), and robotic arm

theoretical (yellow) range of motion, which is based on 4% recoverable wire strain, is explored further in §3.7. Despite its limitations, the developed arm is capable of operating at a further distance from its base than any existing SMA-actuated arm, making it much more suitable for aerial manipulation tasks. While simpler, smaller arms could more easily grasp or move objects on the ground, the increased degrees of freedom of the developed arm makes it appropriate for more complex manipulation tasks.

3.5.4 Experimental Tests

To evaluate the performance of the arm and the adaptive controller described in this section, several tests were conducted. First, the arm's range of motion was tested and compared to its theoretical range to validate the arm design by applying the maximum current to each actuator in series and measuring the joint angle.

Second, the controller's performance was evaluated for a series of step responses for all joints simultaneously, representing a movement from one point to another. The steady-state error of each joint was measured for each step response, and the test is repeated while the arm is carrying a 300 g payload.

Third, a series of path-following tests were conducted. Given a set of waypoints, the desired joint angles are determined using the path-planning algorithm defined in §3.6. The performance of the controller was evaluated by calculating the root-mean-square error (RMSE) of the end-effector's position and orientation.

Table 3.6: Comparison of Calculated Actuator Torques

Reference	Type & DOF	Joint 1 Actuator Max. Torque (Nm)	Arm Mass (g)	Torque-Mass Ratio (Nm/kg)
This study	SMA Bundle, 3-DOF	1.55	546.3	3.88
Ref. 7	SMA Spring, 2-DOF	0.061	129	0.47
Ref. 25	SMA Wire, 1-DOF	0.016	48	0.33
Ref. 89	Motor, 5-DOF	0.588	250	2.35

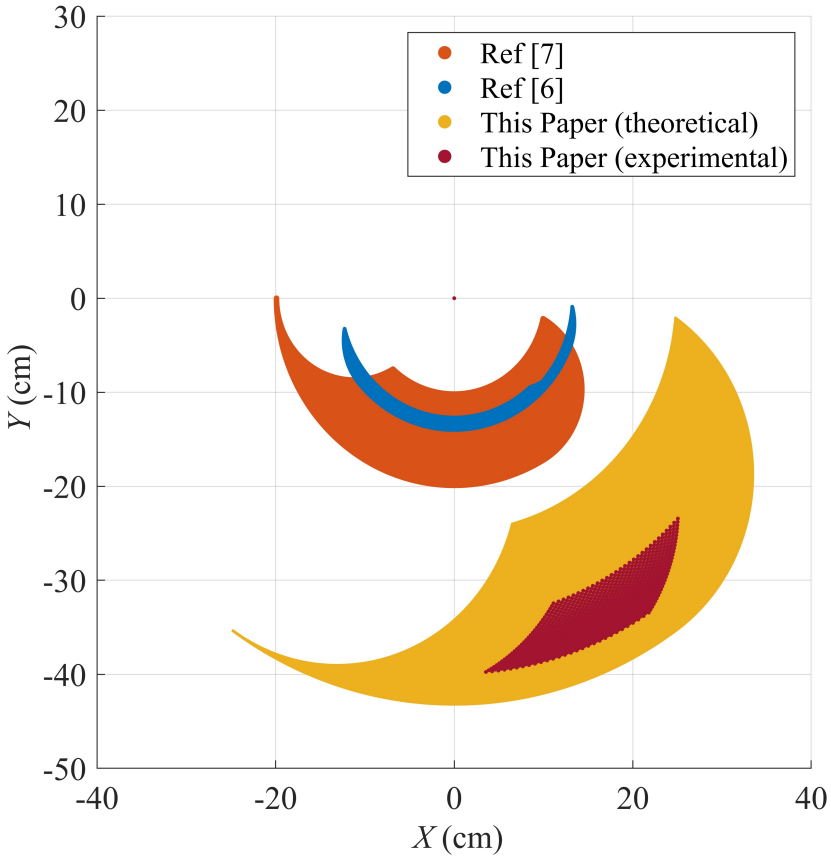

Figure 3.12: A comparison between the range of motion of three SMA-actuated robotic arms. The red region is the measured range of motion, which is discussed further in §3.7.

3.6 Path Planning and Arm Control

During path following tests, the desired behaviour of the arm is to smoothly move from one point, defined by (x_k, y_k) with an orientation, defined by end-effector angle θ_{EE_k} to another at a given time t_k. The desired orientation varies depending on the behaviour of the test being conducted. The inputs given to the path planning algorithm, $\mathbf{W}$, are a set of waypoints defined by Eq. (3.14).

$$\mathbf{W} = \begin{bmatrix} x_1 & x_2 & \dots & x_k \\ y_1 & y_2 & \dots & y_k \\ \theta_{EE_1} & \theta_{EE_2} & \dots & \theta_{EE_k} \\ t_1 & t_2 & \dots & t_k \end{bmatrix} \tag{3.14}$$

From the waypoints $\mathbf{W}$, the inverse kinematics of the arm are calculated to de-

termine the desired joint angles at each waypoint. Motion between the provided waypoints is achieved through the use of intermediate joint angle targets. Between each waypoint, a trapezoidal angular velocity profile is generated with an acceleration time of 2 s, resulting in many target angles equally spaced in time.

Closed-loop control of the arm is achieved using an adaptive PI controller with proportional gains, $\mathbf{K_p}$, and integral gains, $\mathbf{K_{i,a}}$. The controller calculates the desired currents, $\mathbf{I}$, in Eq. (3.15) using the angular joint errors, $\boldsymbol{q_e}$, which are obtained from current joint angles, $\boldsymbol{q_t}$, and desired joint angles, $\boldsymbol{q_d}$, in Eq. (3.16).

$$\mathbf{I} = \mathbf{K_p}\boldsymbol{q_e} + \mathbf{K_{i,a}} \int \boldsymbol{q_e} \tag{3.15}$$

$$\boldsymbol{q_e} = \boldsymbol{q}_{\mathrm{d}} - \boldsymbol{q}_{\mathrm{t}} \tag{3.16}$$

The error integral term is approximated in Eq. (3.17) for timesteps with length t_s. Two sets of gains are used—one for step response tests and one for path following tests. Both sets of gains are included in Table 3.8.

$$\int \boldsymbol{q_e} \approx \sum_{i=1}^{k} \boldsymbol{q_e}(i) t_s \tag{3.17}$$

A simple gain-switching control law defines the joint n element of the integral gain matrix, $K_{i,a,n}$, of the controller in Eq. (3.18). This algorithm switches the controller integral gain between 0 and the positive gain $K_{i,n}$, listed in Table 3.8, when the angular error of a joint is less than 2°. This switching rule resulted in significantly lower error than traditional proportional-integral control. By limiting the growth of the integral term, slow oscillations are prevented without sacrificing the improved steady-state response of the controller. Chatter is not expected from the addition of the gain-switching rule, as the addition of an integral term will not change the direction of motion of the actuator.

$$K_{i,a,n} = \begin{cases} K_{i,n} & \text{if } q_{e,n} < 2^\circ \\ 0 & \text{if } q_{e,n} \geq 2^\circ \end{cases} \tag{3.18}$$

Finally, current-switching logic is introduced to ensure the controller applies current to only one of the two antagonistic actuators within a joint at a time, as described by Eq. (3.19). At each timestep j, this equation determines the current applied to

Table 3.7: Actuator electrical requirements

Joint	1	2	3
Number of Wires	12	14	6
Wire Length (mm)	818	645	497
Wire Resistance (Ω)	15.1	11.9	9.2
Max Current / Wire (A)	0.75	0.75	0.75

the clockwise actuator, $I_{CW,j}$, and counterclockwise actuator, $I_{CCW,j}$.

$$\begin{bmatrix} I_{CW,j} \\ I_{CCW,j} \end{bmatrix} = \begin{cases} \begin{bmatrix} 0 & -I_j \end{bmatrix}^\intercal & \text{if } I_j < 0 \\ \begin{bmatrix} I_j & 0 \end{bmatrix}^\intercal & \text{if } I_j \geq 0 \end{cases} \tag{3.19}$$

The error introduced by the hysteresis of the SMA wires, which occurs due to differing forwards and backwards transformation paths, is reduced in this work by the closed-loop control of the actuator. The inclusion of feedforward terms in the controller may improve performance, especially for more complex controllers, but feedback control has effectively managed the errors introduced by hysteresis in previous works [6, 7].

To prevent overheating, applied current per wire was limited to 0.75 A, which is under the supplier's recommended current for a heating time of 1 second [29]. This current is a safe upper limit for continuous operation that should not result in overheating and can be easily supplied using a 12.55 V source for all wires. The applied current $\mathbf{I}$ is related to desired voltage through Ohm's Law. The resistance of each SMA wire is a function of its phase, stress, and temperature [29], which would require more complex estimators of the wire's phase. The resistance of the wire is instead assumed to be the average resistance of the SMA wire throughout its transformation. The PWM output signal from the Arduino to each MOSFET is the ratio of desired voltage to supply voltage of 12.55 V. Table 3.7 describes the electrical limits of each actuator. A power supply was used to convert 110-120 V AC to 12 V DC power. On an aerial manipulator, power would be supplied either by a separate battery or from the same battery used by the rotors.

3.7 Results and Discussion

Several experiments were conducted to validate the arm's design and controller. First, the actual range of motion for each joint was measured by applying the maximum

voltage to each actuator in series. Second, a series of step responses were tested for each joint simultaneously to measure the controller's steady-state response. Finally, the path planning algorithm was implemented and evaluated by measuring the root-mean-square error of the end-effector position and joint orientation.

The range of motion tests were completed by applying voltage in a series of step responses, applying 0.75 A of current for 30 s, and alternating the direction of motion three times. The first cycle was removed from the data to ensure initial conditions of the arm did not impact the measured range. The results of this test are shown in Fig. 3.13. These tests indicate that the arm's actual range of motion is smaller than the predicted range, which assumes 4% recoverable strain.

To explore the causes of the limited range of motion, an experiment was conducted comparing the behaviour of a full antagonistic actuator (with clockwise and counterclockwise SMA actuators), with a single SMA actuator. The results of these tests are shown in Fig. 3.14. For the single-actuator tests (shown in blue and orange),

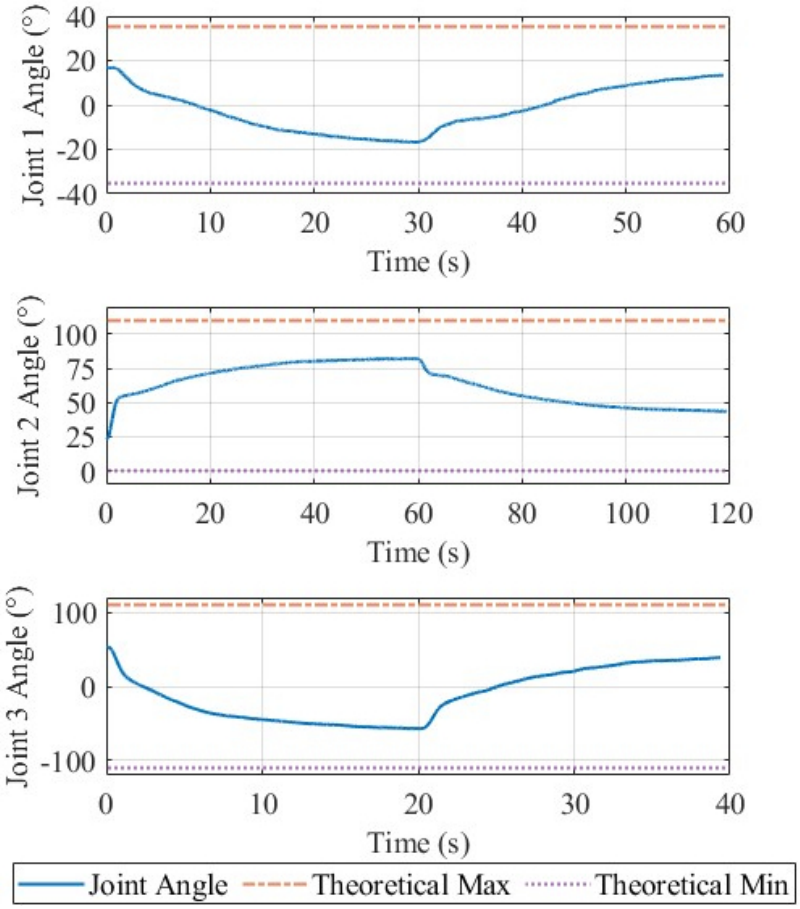

Figure 3.13: Results of the range of motion test for all three joints. The measured angle, theoretical maximum, and theoretical minimum are plotted.

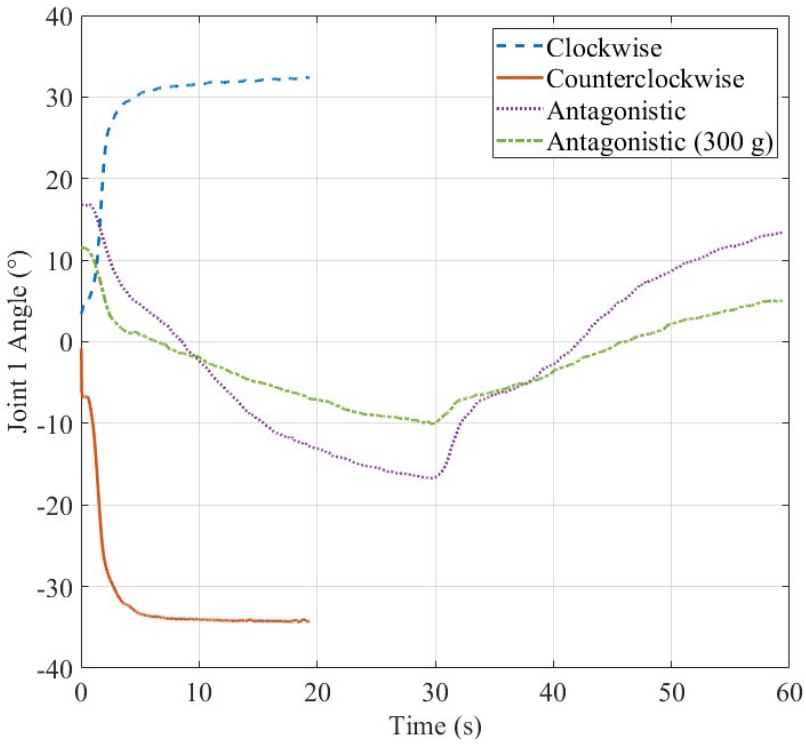

Figure 3.14: Comparison between the antagonistic configuration with and without a 300 g mass, and single-actuator range of motion tests. The single-actuator tests show a much larger range of motion, and reach their limits much more quickly than the antagonistic configuration.

the opposing actuator for joint 1 is physically removed to isolate the performance of an individual SMA actuator. These results are compared to two antagonistic tests with both actuators present—one while manipulating a 300 g mass and one while manipulating no mass. For both tests, 0.75 A of current was applied to the actuator as in previous range tests.

The results show that an individual actuator is capable of reaching the desired range of motion, but cannot when assembled into an antagonistic configuration. The results of the single-actuator tests indicate that rollers do not limit the recoverable strain of the active, contracting wires, likely due to their continuous contraction along its entire length. However, when an antagonistic wire is added, tension is applied only at the end of the passive wire. Friction between the roller and the shaft, as well as friction between the wire and roller, as force is increased, results in a lower tension force after the roller than before it that would compound as the number of rollers increases.

Preliminary off-arm tests were conducted to determine the impact of rollers on an antagonistic configuration. Tests using zero or one roller were able to achieve

Table 3.8: Controller Gains

Test	Joint No.	K_p	K_i for $q_e < 2^\circ$
Step Response	1	16	7e-4
	2	18	8e-4
	3	1.5	5e-5
Path Following	1	14	3e-4
	2	12	1e-4
	3	2	1e-5

4% recoverable strain. This strain was reduced as the number of rollers increased, as measured by images taken of the system, a comparison between this and other SMA-systems can inform avenues for future work. The full arm system differs from existing systems in two important ways. First, the actuator is spooled over four rollers, while the bulk of existing SMA-actuated systems use one or no rollers at all. One SMA-actuated system using similar rollers to those in this project also observed a recoverable strain of only 40% that of an unspooled wire [90]. Secondly, this work is the first to use large bundle actuators over rollers, which may dramatically increase the friction between the rollers and the shafts supporting them. This is supported by the differences between the test carrying a 300 g mass and the test without it, where range of motion is further reduced when wire stress is increased despite all wires being under their maximum stress.

Three potential sources of the observed range reduction are identified.

1. Friction between rollers and wires or between rollers and connecting shafts is higher than expected.

2. The roller design results in a non-homogeneous distribution of strain along the wire's length.

3. The portions of wire along the circular faces they connect to are unable to slide along its length and limit motion.

Step response tests were completed by providing the arm with nine joint angles for each joint ranging across its range of motion and repeated when carrying a 300 g mass. Each test moves from the arm's resting angle to its maximum and minimum limits, then to the center of its range. For the tests carrying the 300 g mass, the target angle of the third joint was set to zero to ensure that the end-effector did not drop the mass and invalidate the test results. The gains for the PI controller were

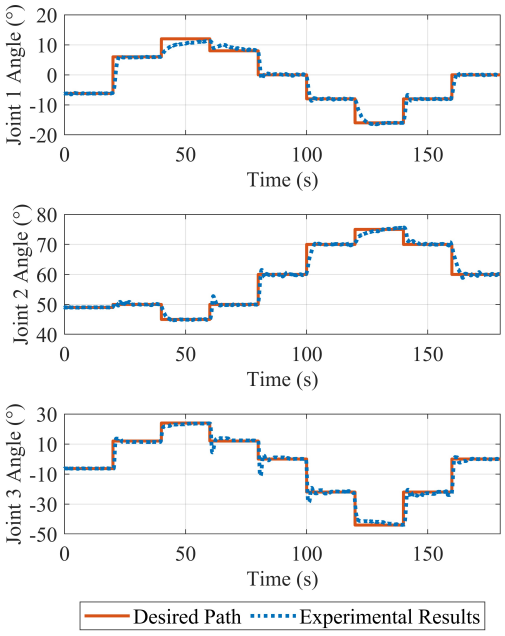

Figure 3.15: Angular position of each joint during a series of unloaded step response tests.

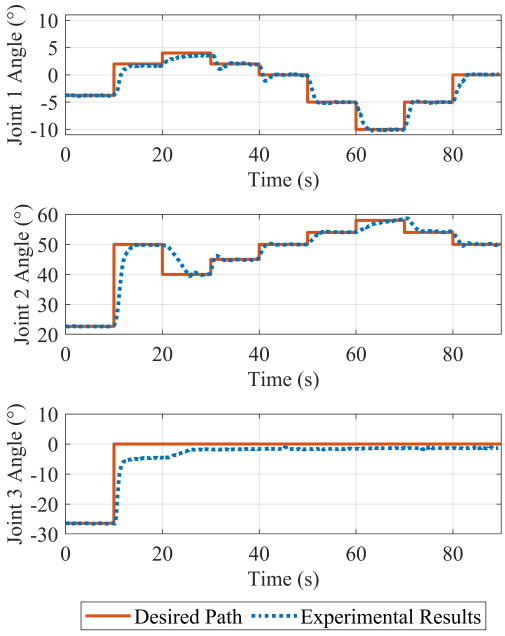

Figure 3.16: Angular position of each joint during a series of step response tests while carrying a 300 g mass.

determined via trial and error, and the same gains were used for both sets of tests as summarized in Table 3.8. To evaluate the efficacy of the controller, the steady-state error magnitude for each step response is calculated as the average error during the last two seconds of each step. The average and maximum observed steady-state error across all responses is shown by joint in Table 3.9.

The results of these tests show that the behaviour of the arm varies across its range of motion. This is clear in Figures 3.15 and 3.16, as well as in the large difference between average and maximum steady-state error in Table 3.9. This is particularly noticeable near the extremities of each joint's range, where the arm moves more slowly and takes much longer to reach its target. Attempts to compensate for this by increasing controller gains led to unacceptably large oscillations near the center of the joint's range.

Path-following tests were conducted by selecting four waypoints for the arm to move to. Points were selected such that the arm would move across its operating space while requiring simultaneous motion from all joints. The end-effector position and orientation are calculated at each timestep based on the forward kinematics of the arm. A second test was completed with a different path while holding a 300 g mass. The results from the first test are shown in Fig. 3.17 and the second are shown in

Table 3.9: Step Response Test Results. Payload = 300 g

	Joint 1	Joint 2	Joint 3
Avg SSE with payload (°)	0.137	0.124	1.754
Max SSE with payload (°)	0.499	0.210	4.684
Avg SSE without payload (°)	0.079	0.348	0.445
Max SSE without payload (°)	0.158	1.530	1.142

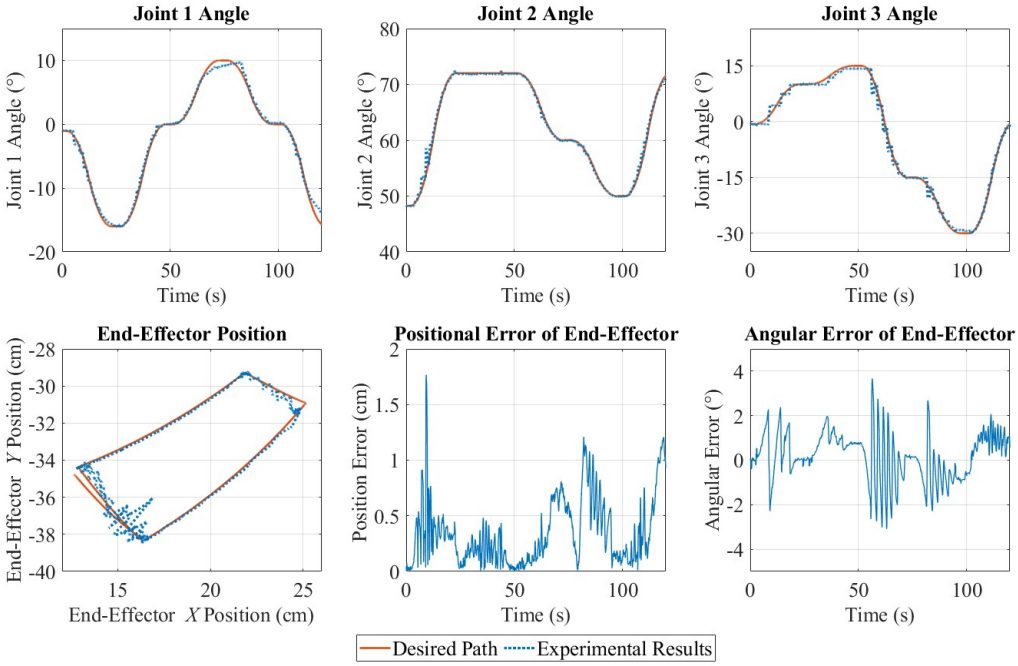

Figure 3.17: Joint angles, end-effector position, and angular error for an unloaded path following test

Fig. 3.18. Both figures show the joint angles over time, the position of the end-effector in 2D space, and the position and angular error of the end-effector. Both tests showed low positional and angular errors, especially when considering the large mass being manipulated when compared to the mass of the arm. The results of these tests are summarized in Table 3.10.

Results from the step response tests show that the controller is capable of achieving fine angular control of each joint. However, the arm is unable to reach the extremities of its range of motion within the given amount of time. Despite this shortcoming, the average steady-state error of the first two joints was below 0.35°. The third joint was more difficult to control under these conditions, and its controller is not as robust to the difference in payload as the first two joints.

The path-planning algorithm results in smooth paths that the arm was able to

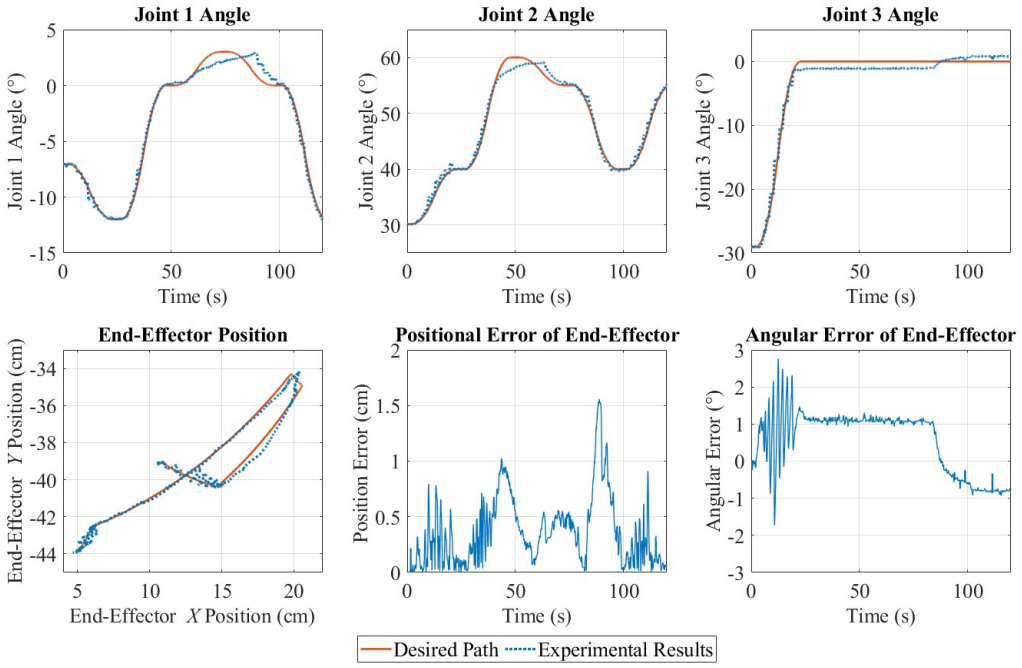

Figure 3.18: Joint angles, end-effector position, and angular error for a path following test carrying a 300 g mass

Table 3.10: Path Following Test Results. Payload = 300 g

	Position (cm)	**Orientation** (°)
RMSE	0.480	0.984
Max Error	1.768	2.761
RMSE with Payload	0.477	1.052
Max Error with Payload	1.558	3.676

follow with low positional and angular error. However, the controller's efficacy is significantly reduced at the extremities of each joint's range, which is particularly noticeable in the plots of joint 1 and 2 angle in Fig. 3.18, resulting in position errors of up to 1.5 cm. It is also notable that positional error is reduced to less than one millimeter at the defined waypoint time T_s, which is extremely precise. The root-mean-square error of the end-effector position of 0.4780 cm and 0.477 cm is over 2.5 times less than previous tests in SMA-actuated path following [7]. Notably, this is more precise than step responses, although this may be due to non-optimal controller gains. The controller is remarkably robust to varying payload masses, and performs similarly when manipulating a 300 g mass than when manipulating no mass at all with no change in controller gains. The controller is less effective during movement between waypoints, particularly for joint 3, at which point each actuator oscillates around the

desired angle. This is likely due to the required time for the opposing actuator to be heated, which could be improved by integrating an anti-slack mechanism to the controller. Under dynamic loads or in unpredictable environments, a more advanced controller may be necessary to achieve similar performance to that achieved during static load testing.

The precision of the arm system is well within the precision required for complex aerial manipulation tasks. In [91], cubic structures were assembled with a 100% success rate with a positional accuracy of 3 cm and angular accuracy of 5° which was easily achieved by the arm controller during path-following tests (as shown in Figs. 3.17 and 3.18). More precise tasks, such as drilling a hole [92], have been achieved with an end-effector accuracy of 2.5 mm, which this arm achieved at the set points of the path planning tests.

3.8 Conclusion

This chapter documented the development of an SMA-actuated robotic arm for aerial manipulation tasks. Topology optimization of the arm links resulted in a mass reduction of 661.3 g, resulting in an arm capable of manipulating payloads over half its own mass. This high payload-mass ratio makes the arm an excellent candidate for an aerial manipulator on a small or medium-sized drone. The arm has a significantly larger manipulation range than existing SMA-actuated arms, and is the first SMA-actuated arm capable of simultaneous position and orientation control.

Initial range of motion testing showed that the antagonistic actuators' recoverable strain was significantly lower than anticipated, opening an avenue for future work. These results suggest that a further study on the effect of roller radius, number, and material would improve the capacity and reliability of SMA-actuated systems. A general model of strain reduction over rollers would make these systems more robust and would increase the fidelity of SMA actuator simulations. Similarly, an investigation of the heat transfer between wires within the actuator bundle could be used to inform the design of future SMA-actuated robotic arms. Further studies could also investigate the performance degradation of the SMA actuator in an applied setting, where the effect of varying cyclical loading as the arm moves throughout its workspace could be observed in a practical environment.

An adaptive PI controller was applied to each joint and experimentally validated through a set of experiments, in which the arm followed a step response and desired path, both of which were able to achieve low positional and angular errors. The arm's

high payload to mass ratio makes it an excellent candidate for aerial manipulation using smaller drone bases than those found in the literature, allowing for tasks to be completed in confined spaces, indoors, or near workers where safety must be emphasized. The SMA actuator's design represents a 25-fold increase in torque when compared to existing SMA-actuated arms. This increased payload is large enough to include gripper manipulators, simple tools, or sensor payloads, making it applicable to construction or inspection tasks.

Chapter 4

Multi-Level Impedance Control of a Shape Memory Alloy Actuated Robotic Arm

4.1 Introduction

Aerial manipulation is a field of robotics that couples drone platforms with robotic systems. An aerial manipulator consists of a flying platform, such as a helicopter or quadrotor, and a manipulator. By enabling flight, the range and mobility of a manipulator can be greatly increased, allowing robots to reach locations that would otherwise be inaccessible. Currently, the mass of the manipulator is the largest restriction in the field, limiting complex arms to large drones [2]. This restriction makes current aerial manipulators unsuitable for tasks near people or in small spaces.

The low mass and high energy density of SMA actuators makes them an excellent candidate for reducing the mass of aerial manipulators. However, this has not been achieved due to several gaps in the literature regarding the design and control of SMA-actuated robotic arms. Specifically, increases to arm range and payload capacity must be achieved before they can be effectively integrated into an aerial manipulator. Additionally, impedance control and state estimation techniques, both of which would allow for more precise interactions between the arm and its environment, have not been completed for multi-DOF, SMA-actuated arms.

This chapter addresses both the design and control gaps in the literature identified in Chapter 2. A 3-DOF, SMA-actuated robotic arm is developed that includes all six actuators within its base. This arm distinguishes itself from the arm developed in

Chapter 3 by the static wire placement, which allows for longer wires to be contained within the base of the arm frame. This arm is sized to match a potential drone for future aerial manipulation tasks. This design requires cable-driven manipulation and couples the motion of each arm joint to multiple actuators in the base frame.

To address the control limitations present in the literature, a novel, SMA-driven compliant actuator is introduced in this chapter. This actuator decouples the SMA actuator and load components through springs, enabling direct torque measurement as well as simultaneous control of the clockwise and counterclockwise actuators. This strategy allows for separate position control of each actuator, which can be extended to torque control given the actuator's known spring constant and measured deflection. Simultaneous deflection of both actuators allows for wires to stay within their transformation temperature at all times. A new bidirectional controller is introduced to prevent wire slack and is compared to existing antagonistic controller performance. Additionally, this work investigates the application of an extended Kalman filter (EKF) in the developed robotic arm. The methodology for integrating multiple SMA actuator estimators into a control system is addressed and used in the impedance controller experiments.

In this chapter, the design of a 3-degree-of-freedom, SMA-actuated arm is discussed in §4.2. §4.2 also presents the design of a novel compliant actuator capable of simultaneous control of antagonistic actuators. §4.3 discusses the simulation and modeling of the SMA actuators, the compliant joint, and the robotic arm as a whole. A formulation of an extended Kalman filter is described that addresses the unique dynamics of the compliant joint. Controllers for actuator position and joint torque are introduced in §4.4, alongside higher level impedance and position controllers. A comparison is conducted between the proposed position controller and traditional antagonistic control methods. Finally, the results of experimental tests and validation of the proposed controllers are included in §4.6 with a brief conclusion in §4.7.

4.2 Arm Design

A new SMA-actuated arm design is introduced in this work to experimentally validate the proposed controller. Unlike existing SMA-actuated arms, which integrate SMA actuators within arm links [7, 26], this design mounts all SMA actuators in a fixed position within the base structure of the arm. This increases the available range of motion of the arm without requiring multiple rollers to extend wire length. Previous work has shown that using multiple rollers can significantly reduce the effective range

of motion of SMA-actuated arms [26]. This has the additional benefit of maintaining the SMA wires at a fixed angle, removing any changes in heat transfer coefficients due to the angle of the arm links.

A set of stiff cables and rollers transfer joint torque from the actuators fixed in the base to each individual joint. This strategy has been employed before in other aerial manipulation projects to reduce the mass of the arm links [4], but not in SMA-actuated works.

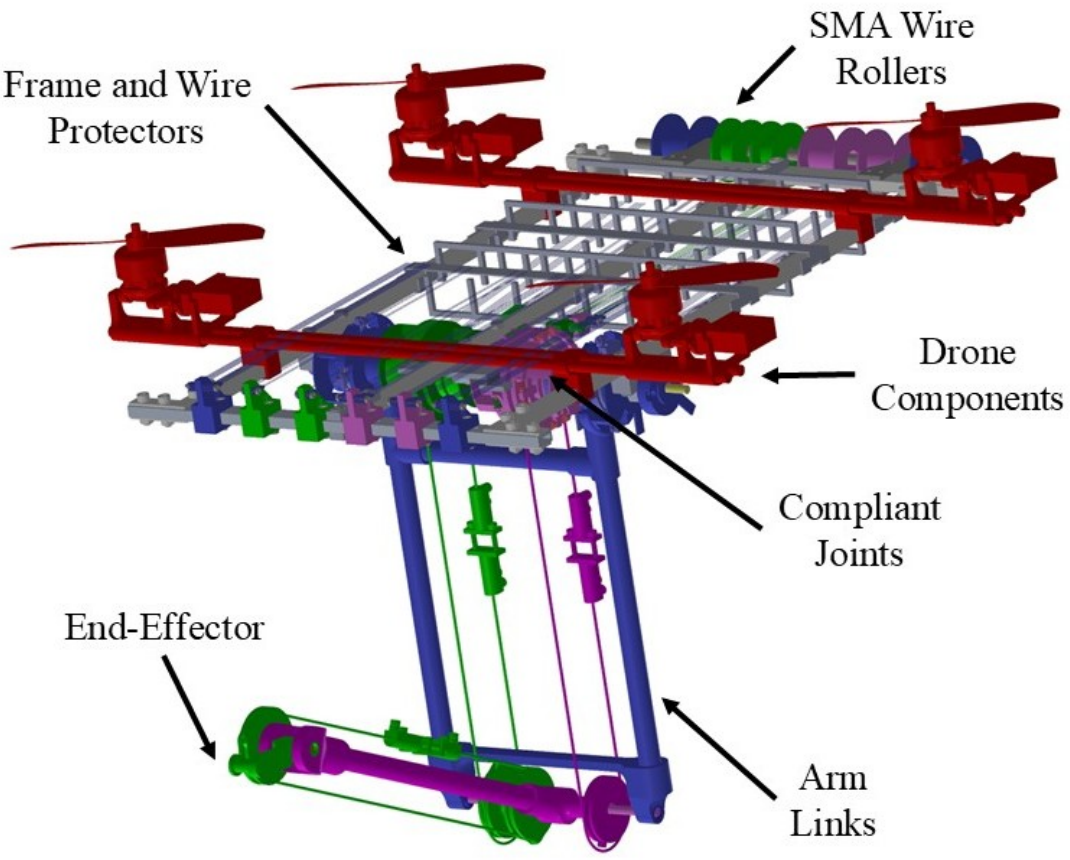

Figure 4.1: CAD model of the robotic arm showing link 1 (blue), link 2 (pink) and link 3 (green), and future drone (red) components.

4.2.1 Arm Structure

The structure of the arm, shown as a CAD model in Figure 4.1 and an image in Figure 4.2, is a 20 by 40 cm rectangular frame made from 0.25x0.5 in hollow aluminum structural tubes (McMaster Carr #6546K47). The frame includes mounting points for drone rotors, easily enabling the arm structure to also function as a drone frame, as shown in Figure 4.1. This frame supports the SMA actuator mounting points, the SMA actuator rollers, and the shaft for joint 1 of the robotic arm. The arm links, each 25 cm long, are manufactured from three hollow carbon fiber tubes with

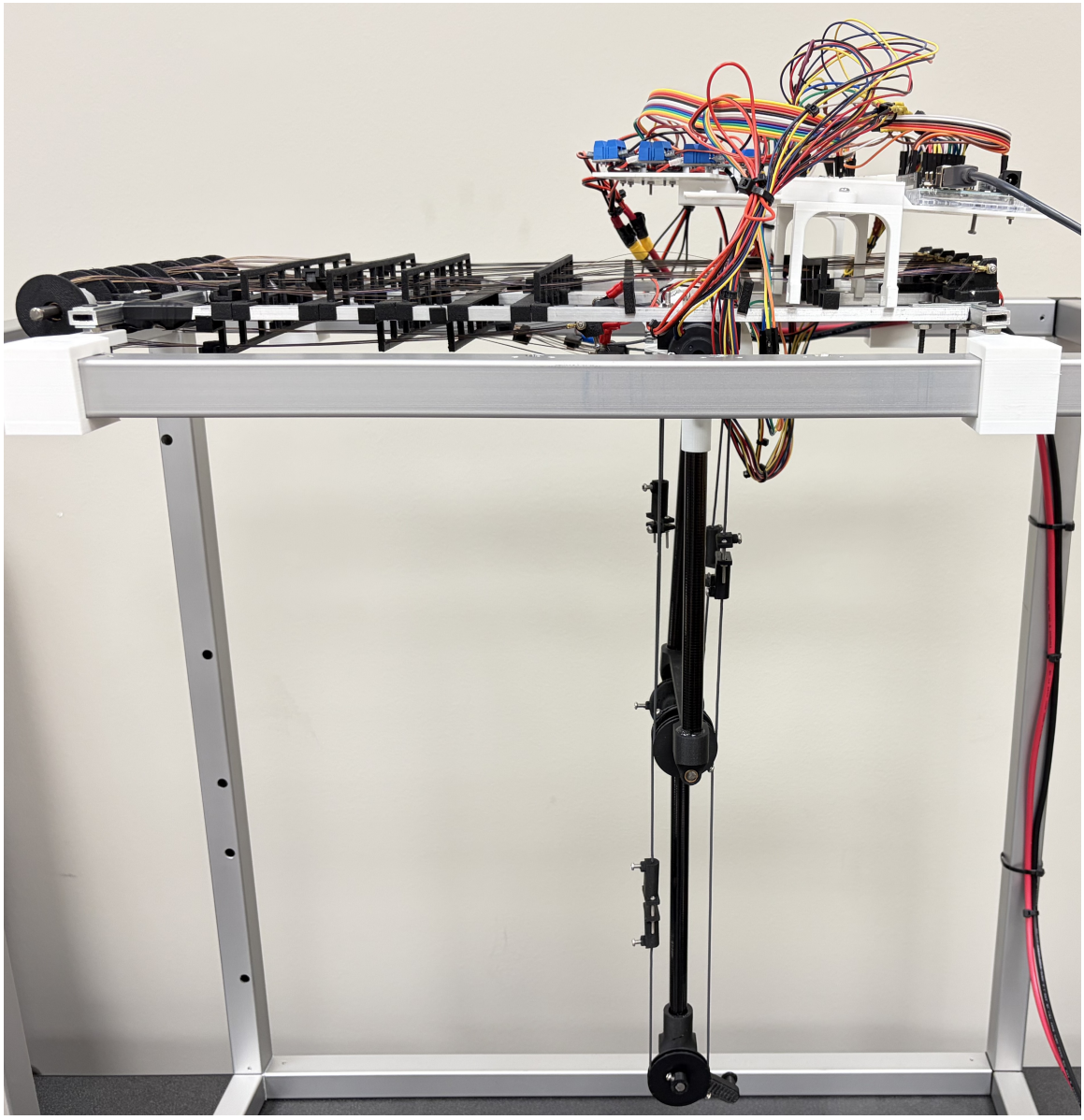

Figure 4.2: Image of the robotic arm and test stand

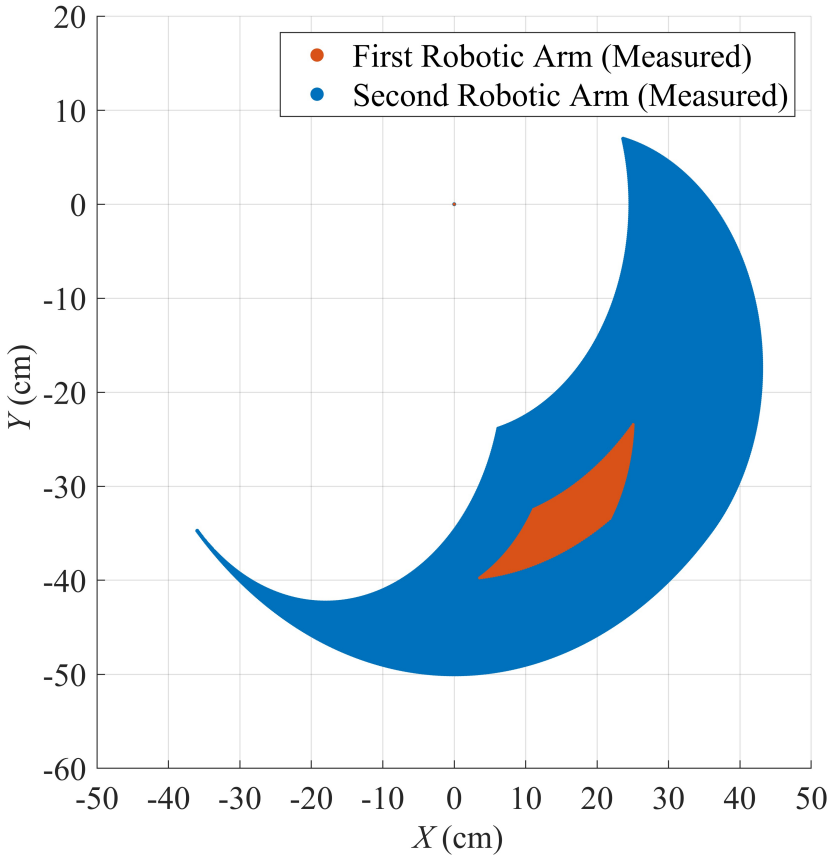

Figure 4.3: Comparison between the measured operating spaces of the first (Chapter 3, orange) and second (Chapter 4, blue) robotic arms.

a diameter of 0.485 in and wall thickness of 0.055 in (McMaster Carr #5287T614) epoxied to 3D printed components at the tube ends. SMA actuators are located on the frame itself, resulting in torque being transferred to joints 2 and 3 via a set of rollers and stiff cables. Power is supplied to the actuators via a set of 6 MOSFETs (supplied by LGDehome) with a maximum current of 15 A and a 12 V, 30 A AC-DC power converter (supplied by Anbull). The amount of current sent to each actuator is controlled by a PWM signal from an Arduino Mega, which also prevents overcurrent draw from the power converter.

A preliminary comparison of the operating spaces, as measured by the maximum angles each joint could reach by the encoders, was conducted between the arms developed in Chapter 3 and this chapter. This comparison, detailed in Figure 4.3, shows that the improved arm design has a dramatically improved operating space. While the range of motion of each joint matches a recoverable strain of 2.5% -3%, instead of

the predicted 4%, it still results in an operating space larger than any SMA-actuated arm. The reduction in recoverable strain is partially due to the deflection implied by the compliant joint, which requires the SMA actuator to move over a larger angle than the load component. Additionally, a stiffer joint would likely increase the range of motion, as it would more easily apply the force required to stretch the SMA wire, at the cost of sensing precision.

4.2.2 SMA Actuator Design

The developed SMA actuators are composed of multiple SMA wires in parallel to increase the available torque of the actuator. Flexinol brand high-temperature (90°C) wires with a diameter of 0.31 mm and length of 0.75 m were used. The wires span the length of the frame to maximize the range of motion of the arm. A single roller is used to reduce friction issues previously seen with multiple rollers in [26]. This design allows for all actuators to remain stationary as the arm moves, simplifying the structure and maintaining constant heat transfer parameters.

The moving ends of the SMA actuators are electrically connected in parallel and mechanically connected to a stiff cable (McMaster Carr #3461T633), as shown in Figure 4.4. The stiff cable attaches directly to the components of the compliant actuator and makes the compliant actuators significantly thinner than if they had to accommodate the full width of all SMA wires.

The full arm, including the frame, weighs less than a kilogram. The majority of the mass is concentrated in the frame, metal shafts, and wire rollers. The SMA wires themselves only constitute 7.2% of the arm mass, which is significantly less than if DC or stepper motors were used. Table 4.1 lists the masses of each arm component.

4.2.3 Compliant Actuator Design

The arm is actuated by three custom-designed compliant joints, shown in Figure 4.5. Each compliant joint includes two antagonistically arranged SMA actuators—one for clockwise motion and another for counterclockwise motion. The SMA actuators are separated from a central load component by a set of springs, as shown in Figure 4.5. The load component is directly attached to the load cable that transfers torque to the robotic arm joints. The structure of joint 1's compliant actuator is fundamentally the same, but has the load component mounted to the link itself.

These rotating components, which rotate on a shared shaft, are connected to each other via a set of small compression springs. By including multiple compression

Table 4.1: Summary of arm component masses

Component	Mass (g)	Mass (%)
Rollers	50.8	5.2
SMA Wires	70.0	7.2
Shafts	141.5	14.5
SMA Wire Guards	22.3	2.3
SMA Mounting Points	20.3	2.1
Aluminum Framing and Hardware	261.4	26.8
Link 1 Structure	50.8	5.2
Link 2 Structure	40.0	4.1
End-Effector	4.6	0.5
Stiff Cables	30.0	3.1
Stiff Cable Rollers	28.9	3.0
Compliant Joint 1	50.7	5.2
Compliant Joint 2	30.7	3.1
Compliant Joint 3	27.0	2.8
Encoders	148.7	15.2
Total	977.7	100

Table 4.2: Robotic arm and SMA actuator parameters

Parameter	**Joint 1**	**Joint 2**	**Joint 3**
Wire Length (m)	0.75	0.75	0.75
Wire Diameter (mm)	0.31	0.31	0.31
Number of Wires	10	10	4
Wire Maximum Stress (MPa)	180	180	180
Actuator Mounting Radius (mm)	14.3	9.5	9.5
Calculated Maximum Torque (Nm)	1.8	1.2	0.3
Spring Coefficient (Nm/°)	0.36	0.24	0.06
Joint Damping Coefficient (°/s)	0.07	0.07	0.02
Calculated Range of Motion (°)	127.4	180	180
Measured Range of Motion (°)	92	121	106
Link Length (m)	0.25	0.25	0.05

springs along the circumference of a circle, the angular stiffness of the equivalent spring they construct can be increased while keeping the assembly as small as possible. Torsion springs would make the compliant actuator much wider, requiring a larger arm link. The springs will be slightly angled when compressed, but the low angular deflection of 5°maintains the compression springs within their linear range. This assumption is verified by experimental results in §4.6. Actuator parameters (e.g., the number and length of wires, actuator stiffness) are included in Table 4.2. The size of the joint is further reduced by sizing holes to self-tap when bolts are tightened, allowing components to connect without adding nuts or washers.

Figure 4.6 shows a exploded view of the compliant joint, color-coded to show groups of components that rotate together. The joint angle encoder at the center of the joint measures angle relative to magnet adhered to the shaft (yellow), and the deflection encoders measure angles relative to magnets adhered to the clockwise (green) and counterclockwise (red) components. The load component (blue) attaches to the stiff torque transfer cable. This stiff cable transfers torque from the actuator to the robotic arm joints, whose angles are measured by the joint angle encoder. This work uses the HD High Resolution Kit produced by Pheonix America, which includes the magnetic encoder with a resolution of 1500 pulses per revolution and a target magnet with a bore diameter of 0.25 in. Resolution is improved to 6000

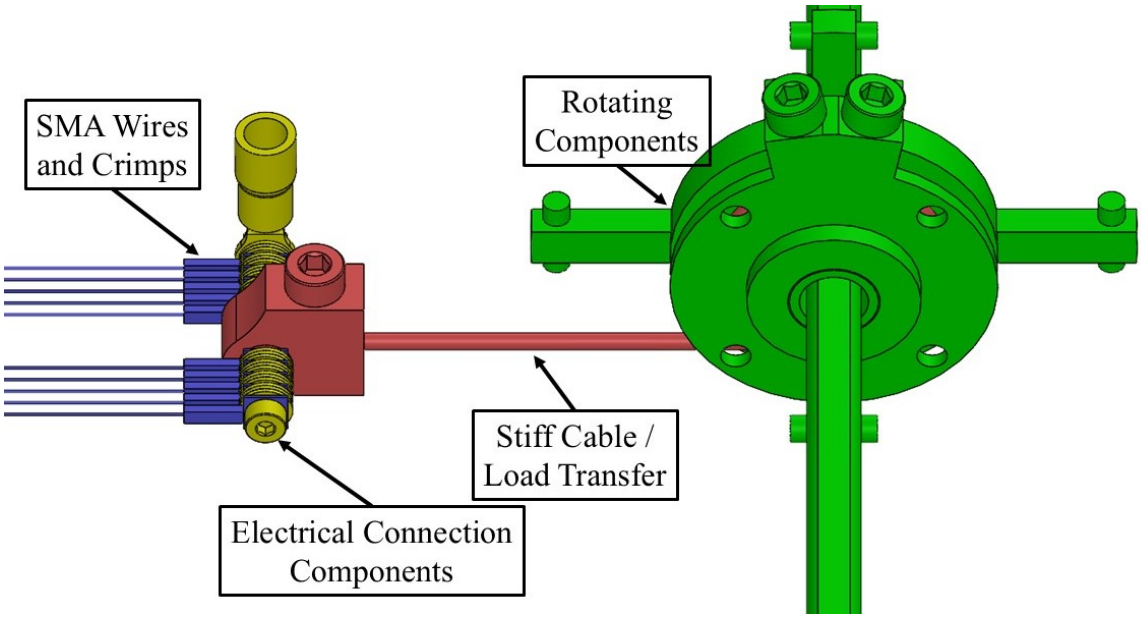

Figure 4.4: CAD model of a single SMA actuator showing SMA wires (blue), stiff cables (red), electrical connection components (yellow), and rotating components (green)

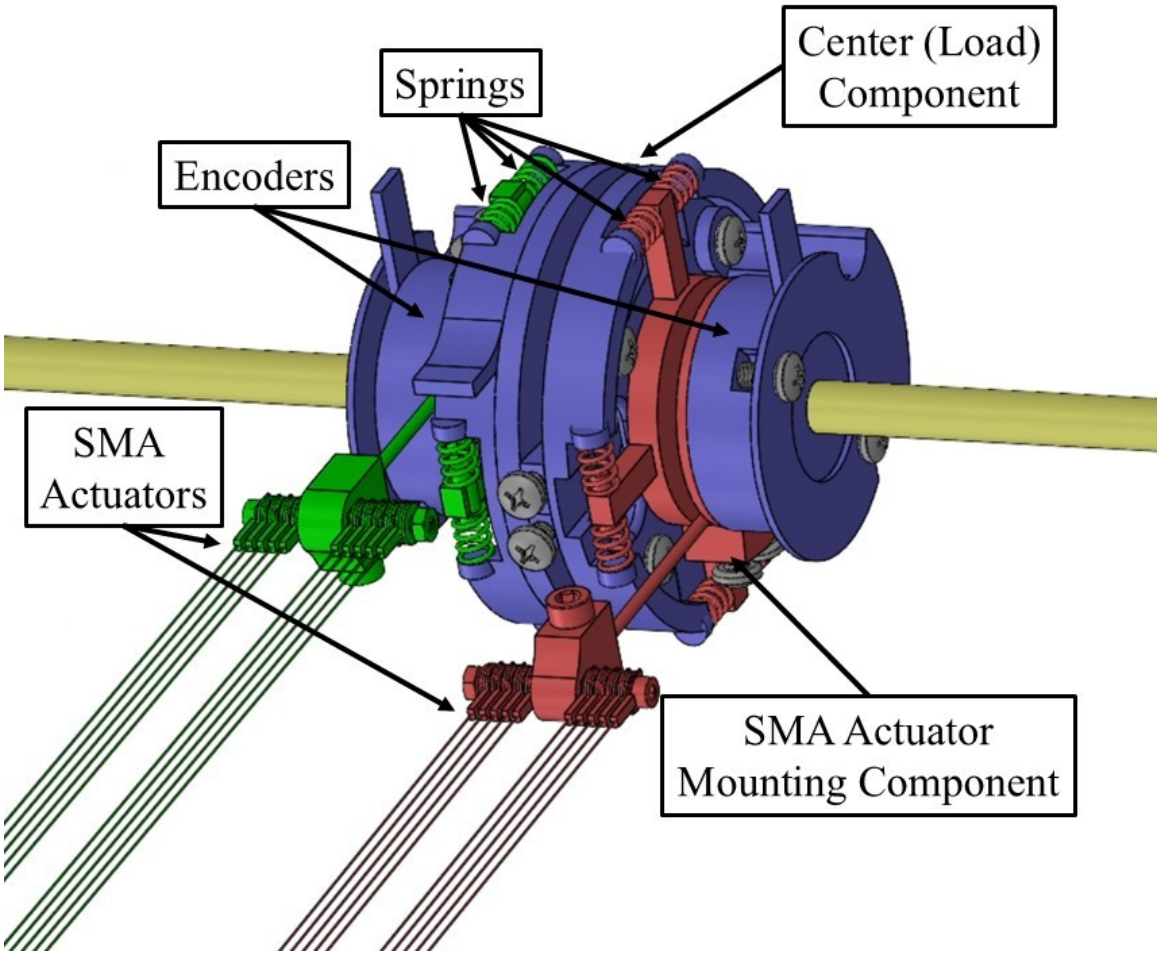

Figure 4.5: CAD model of the compliant joint highlighting the center and actuator mounting components. The relative angles of clockwise (CW) (green) and counter-clockwise (CCW) (red) SMA actuators are measured by encoders connected to the central load component (blue). The joint angle is measured relative to a magnet adhered to the shaft (yellow)

pulses per revolution (0.06 °per pulse) by counting both rising and falling edges of the quadrature signal. These pulses are counted by an Arduino MEGA, which is reported to the control computer at a rate of 10 Hz. The relatively low communication rate is to ensure quadrature steps are not missed during serial communication, and is an acceptable rate for SMA actuators whose actuation time is on the order of seconds.

The compliant actuator provides two significant benefits over traditional SMA actuators. First, it provides a direct measurement of wire stress. Given the deflection of each actuator, the known spring constant, and the geometric properties of the actuator, a measured deflection can be directly translated to a measured wire stress or joint torque. Second, it allows for more precise control of antagonistic actuators.

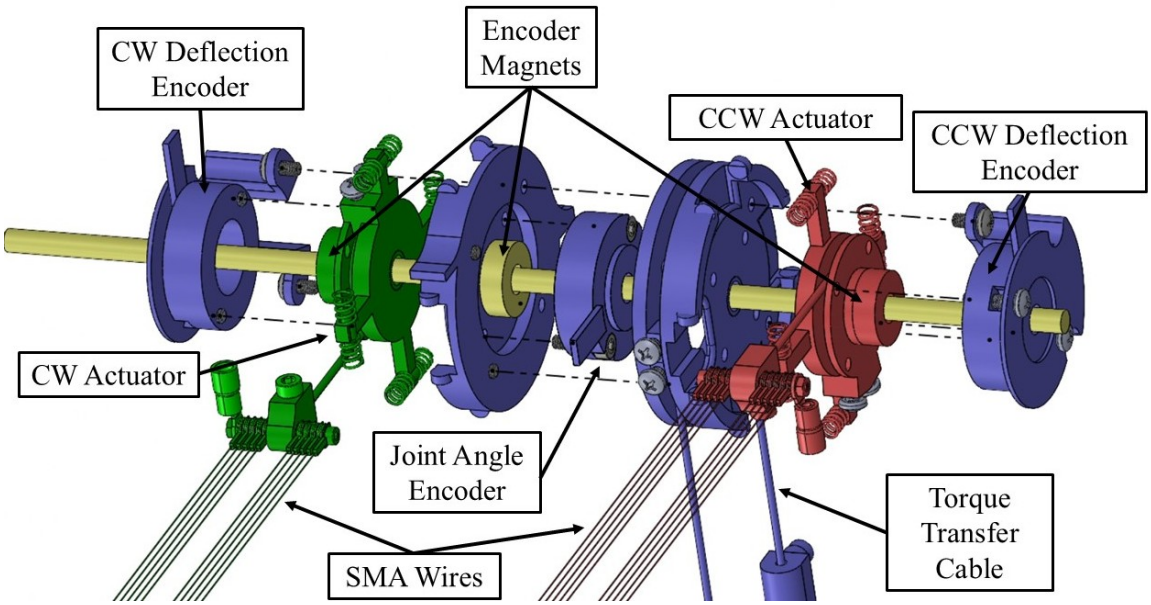

Figure 4.6: Exploded view of the compliant joint color-coded to show co-rotating components. The relative angles of clockwise (CW) (green) and counterclockwise (CCW) (red) SMA actuators are measured by encoders connected to the central load component (blue). The joint angle is measured relative to a magnet adhered to the shaft (yellow)

Traditional antagonistic actuators use an "active" wire where voltage is applied, and a "passive" wire where no voltage is applied. This method introduces several control issues, including the introduction of slack in the passive wires, potential overstressing of the wires, and delays when switching direction. The compliant joint eliminates these problems entirely by replacing the "passive" wire with a second "active" wire that targets a very small deflection. Maintaining both wires in tension completely eliminates wire slack and the issues it introduces. Additionally, it prevents wire overstress by measuring the stress directly—allowing for the system to be disabled if an unsafe condition is approached. This simultaneous control strategy is discussed further in §4.4.

4.3 Arm and Actuator Simulation

This section documents the simulation methods and mathematical models governing the actuator-arm system that are used in the EKF stage of the high-level controller. The equations governing the heat transfer and transformation of each SMA wire are discussed, followed by a description of the equations defining the compliant joint.

The forward and inverse kinematics of the arm are defined and applied in the full simulation employing the EKF.

4.3.1 Wire Heat Transfer Model

The heat transfer of the wire is defined as a combination of Joule heating and convective heat transfer to the air, as solved in [25]. It solves for the derivative of temperature, dT/dt, from current wire temperature, T, ambient temperature, T_{amb}, applied voltage, V, wire surface area, A_w, the mass of the wire, m_w, the specific heat capacity, c_p, wire phase, ξ. The definitions of these equations are shown in Equations (4.1), (4.2), and (4.3) [25]. The final equation, Eq. (4.4) [25], solves for the temperature derivative that is applied later in this work.

$$m_w c_p \frac{dT}{dt} = \frac{V^2}{R(\xi)} - h(T)A_w(T - T_{amb}) \tag{4.1}$$

The heat transfer coefficient $h(T)$ is calculated from the first and second-order constants h_0 and h_2 in Eq. (4.2) [25].

$$h(T) = h_0 + h_2 T^2 \tag{4.2}$$

Wire resistance $R(\xi)$ is calculated assuming a linear transition from martensite resistance R_m and austenitic resistance R_a in Eq. (4.3) [25].

$$R(\xi) = R_m \xi + (1 - \xi)R_a \tag{4.3}$$

Eq. (4.1) is solved for the time derivative of temperature, $\frac{dT}{dt}$, in Eq. (4.4).

$$\frac{dT}{dt} = \frac{\frac{V^2}{R(\xi)} - h(T)A_w(T - T_{amb})}{m_w c_p} \tag{4.4}$$

4.3.2 Wire Constitutive Model

This work uses the 1-dimensional constitutive model of an SMA wire for forward and backwards transformation that is defined in Eq. (4.5) [93]. The martensite and austenite transformation start temperatures, M_s and A_s, and end temperatures, M_f and A_f, define the beginning and end temperatures of each transformation direction, at which wire phase ξ reaches ξ_M or ξ_A at the completion of their transformation. The constants $a_A = \pi/(A_f - A_s)$, and $a_M = \pi/(M_s - M_f)$ simplify the phase transformation equations, and $b_A = -a_A/C_A$, and $b_M = -a_M/C_M$ define the effect of wire

stress on transformation temperature, where C_A and C_M are parameters defining the relationship between wire stress, σ, and temperature.

$$\xi = \begin{cases} \frac{\xi_M}{2}(\cos[a_A(T - A_s) + b_A\sigma] + 1) & \text{if } A_s + \frac{\sigma}{C_A} \leq T \leq A_f + \frac{\sigma}{C_A} \\ \frac{1-\xi_A}{2}\cos[a_m(T - M_F) + b_m\sigma] + \frac{1+\xi_A}{2} & \text{if } M_s + \frac{\sigma}{C_M} \leq T \leq M_f + \frac{\sigma}{C_M} \end{cases} \tag{4.5}$$

The derivative of phase, $\dot{\xi}$, is defined in Eq.(4.6) [93], by the partial derivatives of Eq. (4.5). The partial derivative with respect to temperature T is defined in Eq. (4.7) [93] and with respect to stress in Eq. (4.8) [93].

$$\dot{\xi} = \xi_T(T, \sigma)\dot{T} + \xi_\sigma(T, \sigma)\dot{\sigma} \tag{4.6}$$

$$\xi_T(T, \sigma) = \begin{cases} -\frac{\xi_M}{2}\sin(a_A(T - A_s - \frac{1}{c_A}\sigma))a_A & \text{if } A_s < T - \frac{\sigma}{c_A} < A_f \text{ and } \dot{T} - \frac{\dot{\sigma}}{c_A} > 0 \\ -\frac{1-\xi_A}{2}\sin(a_M(T - M_f - \frac{1}{c_M}\sigma))a_M & \text{if } M_f < T - \frac{\sigma}{c_M} < M_s \text{ and } \dot{T} - \frac{\dot{\sigma}}{c_M} > 0 \\ 0, & \text{otherwise.} \end{cases} \tag{4.7}$$

$$\xi_\sigma(T, \sigma) = \begin{cases} -\frac{1}{c_A}\xi_T(T, \sigma) & \text{if } A_s < T - \frac{\sigma}{c_A} < A_f \text{ and } \dot{T} - \frac{\dot{\sigma}}{c_A} > 0 \\ -\frac{1}{c_M}\xi_T(T, \sigma) & \text{if } M_f < T - \frac{\sigma}{c_M} < M_s \text{ and } \dot{T} - \frac{\dot{\sigma}}{c_M} > 0 \\ 0, & \text{otherwise.} \end{cases} \tag{4.8}$$

The wire constitutive model, shown in Eq. (4.9) [93], relates the derivatives of temperature, $\dot{T}$, stress, $\dot{\sigma}$, and strain, $\dot{\epsilon}$, where Ω is the phase transformation constant defined by $\Omega = -E\sigma_0$, Θ is a thermal expansion coefficient of the wire, and E is the Young's Modulus of the wire, computed as $E(\xi) = E_A + \xi(E_M - E_A)$, where E_A and E_M are the Young's Modulus of the wire at the austenite and martensite phase.

$$\dot{\sigma} = E\dot{\epsilon} + \Omega\dot{\xi} + \Theta\dot{T} \tag{4.9}$$

The actuator kinematics and fixed wire mounting radius define the strain of the wire, ϵ, from the angle of the actuator component in degrees, θ_a, by the constant actuator mounting radius, r, and the initial wire length, L_w, in Eq. (4.10) [93].

$$\epsilon = \frac{\pi r}{180 L_w} \theta_a \tag{4.10}$$

4.3.3 Compliant Joint Kinematics

The compliant joint mechanically connects three coaxial components through two sets of springs, as discussed in §4.2.3. Each joint measures three angles—the two deflection angles ϕ_{CW} and ϕ_{CCW} and the center load component angle θ_c. The compliant joint torques are modeled as a set of kinematic equations and ignore the very small inertia of the SMA actuator itself, which is orders of magnitude smaller than that of the load component. The model of the SMA wires is used to solve for the actuator component angles, $\boldsymbol{\theta}_a$, which is solved for each joint n in Eq. (4.11). The robotic arm dynamics model solves for link angles, $\mathbf{q}$, which are then solved to obtain load component angles, $\boldsymbol{\theta}_C$.

$$\theta_{a,n} = \begin{cases} \theta_{c,n} + \phi_{CW,n} & \text{if clockwise} \\ \\ \theta_{c,n} - \phi_{CCW,n} & \text{if counterclockwise} \end{cases} \tag{4.11}$$

4.3.4 Forward Kinematics

The forward kinematics of the arm define the position of the tip of the end-effector, $\begin{bmatrix} X_{EE} & Y_{EE} \end{bmatrix}$, as well as its orientation relative to the base plane, q_{EE}. The locations of the encoders at the base of the arm and pulleys connecting them requires a trasformation from measured encoder angles, $\boldsymbol{\theta}_c$, to relative link angles, $\mathbf{q}$, in Eq. (4.12).

$$\begin{bmatrix} q_1 \\ q_2 \\ q_3 \end{bmatrix} = \begin{bmatrix} \theta_{c1} - 90^\circ \\ \theta_{c2} \\ \theta_{c3} - \theta_{c2} \end{bmatrix} \tag{4.12}$$

To simplify the notation in the following equations, the cosine and sine of joint angle n will be defined as c_n and s_n respectively. If the sum of two angles is used, the joint angles will be displayed in sequence (e.g., the cosine of $q_1 + q_2$ is represented as c_{12}.

$$\mathbf{P} = \begin{bmatrix} X_{EE} \\ Y_{EE} \\ q_{EE} \end{bmatrix} = \begin{bmatrix} L_1 c_1 + L_2 c_{12} + L_3 c_{123} \\ L_1 s_1 + L_2 s_{12} + L_3 s_{123} \\ q_{123} \end{bmatrix} \tag{4.13}$$

4.3.5 Inverse Kinematics

Beginning from the desired end-effector position and orientation, $\mathbf{P}$, wrist position, $\begin{bmatrix} P_x & P_y \end{bmatrix}$, is calculated in Eq. (4.14) from the desired end-effector orientation, q_{EE}, as measured relative to the horizontal axis of the base.

$$\begin{bmatrix} P_x \\ P_y \end{bmatrix} = \begin{bmatrix} X_{EE} - L_3 \cos(q_{EE}) \\ Y_{EE} - L_3 \cos(q_{EE}) \end{bmatrix} \tag{4.14}$$

The angle of joint 2 is determined from the triangle formed by the base joint and wrist position. An elbow-down configuration is always selected due to the range constraints on the joints, as shown in Eq. (4.15).

$$q_2 = \arccos\left(\frac{P_x^2 + P_y^2 - L_1^2 - L_2^2}{2L_1L_2}\right) \tag{4.15}$$

The angle of joint 1 is then calculated in Eq. (4.16) using:

$$q_1 = \arctan\left(\frac{P_y}{P_x}\right) - \arctan\left(L_2 \sin\left(\frac{q_2}{L_1 + L_2 c_2)}\right)\right) \tag{4.16}$$

Finally, the angle of joint 3 is determined in Eq. (4.17) to satisfy the orientation constraint.

$$q_3 = q_{EE} - q_1 - q_2 \tag{4.17}$$

4.3.6 Forward Dynamics

The forward dynamics of the arm determine the acceleration of each joint when provided joint torques, velocities, positions, and end-effector forces. The acceleration, $\ddot{\mathbf{q}}(k)$, is defined in Eq. (4.18) [67], where $\mathbf{C}(\mathbf{q}(k), \dot{\mathbf{q}}(k))$ represents the centrifugal and coriolis matrix, $\mathbf{G}(\mathbf{q}(k))$ represents the torque due to gravity, and $\boldsymbol{\tau}(k)$ represents applied joint torque. This equation is solved at each simulation timestep index, k.

$$\ddot{\mathbf{q}}(k) \;=\; \mathbf{M}(\mathbf{q}(k))^{-1}\Big(\boldsymbol{\tau}(k) - \mathbf{C}(\mathbf{q}(k), \dot{\mathbf{q}}(k))\,\dot{\mathbf{q}}(k) - \mathbf{G}(\mathbf{q}(k))\Big) \tag{4.18}$$

In the simulation of the arm, a forward Euler approximation is used in Eqs. (4.19) and (4.20) to calculate the simulated joint angular velocity, $\dot{\mathbf{q}}$, and position, $\mathbf{q}$, based on timestep duration, t_s.

$$\dot{\mathbf{q}}(k) = \dot{\mathbf{q}}(k-1) + \ddot{\mathbf{q}} t_s \tag{4.19}$$

$$\mathbf{q}(k) = \mathbf{q}(k-1) + \mathbf{q}t_s \tag{4.20}$$

The gravity compensation matrix, $\mathbf{G}(\mathbf{q}(k))$ calculates the joint torques required to maintain the arm in static equilibrium with link lengths, L_n, which assume masses concentrated at distance along the link, l_{cn}. The inertia matrix $\mathbf{M}$ and coriolis/centrifugal matrix $\mathbf{C}(\mathbf{q}(k), \dot{\mathbf{q}}(k))$, are defined as Eqs. (1) and (2) in Appendix A.

$$\mathbf{G}(q(k)) = g \begin{bmatrix} l_{c1}m_1c_1 + (L_1 + l_{c2})m_2c_{12} + (L_1 + L_2 + l_{c3})m_3c_{123} \\ l_{c2}m_2c_{12} + (L_2 + l_{c3})m_3c_{123} \\ l_{c3}m_3c_{123} \end{bmatrix} \tag{4.21}$$

Then, the net torques applied by the compliant actuators, $\boldsymbol{\tau}_{net}$, are modeled by the sum of the two spring torques with spring coefficients, K, and damping forces with coefficients, $\mathbf{B}$, as shown in Eq. (4.22). Damping coefficients were approximated by running simulations of the arm with varying coefficients, then selecting the values that resulted in both stable simulations and matched experimental results. A more thorough investigation of damping coefficients may improve results, as would a more complex friction model. However, the high torque and low angular velocity of the arm joints reduce the impact of errors in friction modeling on the EKF performance. The approximated values of $\mathbf{B}$ are included in Eq. (4.23).

$$\boldsymbol{\tau}_{net} = \mathbf{K}(\boldsymbol{\phi}_{CW} - \boldsymbol{\phi}_{CCW}) - \mathbf{B}\dot{\boldsymbol{\theta}}_C \tag{4.22}$$

$$\boldsymbol{B} = \begin{bmatrix} 0.07 & 0.07 & 0.02 \end{bmatrix} \tag{4.23}$$

4.3.7 Extended Kalman Filter

An extended Kalman filter (EKF) is a statistical method that combines nonlinear system models with experimental data to provide an estimated state. An amount of uncertainty, represented by a Gaussian distribution, is included in the estimated and measured states. This filter is often used in applications where there is high model uncertainty or sensor noise. The extended Kalman filter handles the nonlinear system model by linearizing it about the current state at each timestep. Not all system states need to be measured for the EKF to provide estimates for each state, so long as

they are observable. Other filtering methods, such as the unscented or particle filter, function similarly but do not require functions to be differentiable [94]. However, they require increased computational resources and require more complex tuning. In this work, an EKF was used given its simplicity and the high computational requirements for modeling the actuator and arm system.

Several simplification steps were conducted to model the SMA-actuated robotic arm system. While an EKF could theoretically be designed to accommodate the nonlinear behaviour of the robotic arm and its interactions with each actuator, such a system would have a very large number of state variables, dramatically increasing the simulation complexity and computation requirements. Existing SMA-based EKF simulations [16] simplify this problem by considering stress as a variable defined by the dynamics of the robotic arm. However, this cannot be applied to antagonistic configurations, which introduce an additional variable to be resolved. Additionally, this would require an accurate model of the inverse dynamics of a multi-degree-of-freedom robotic arm as opposed to the simple spring-mass-damper systems EKFs have been applied to thus far.

This work simplifies the system first by giving each actuator a separate estimator that is then mathematically linearized through a simulation of the forward dynamics of the robotic arm. Each estimator considers the angle of the center load component of the compliant actuator to be a system input. Additionally, a switching behaviour defined in §4.3.2 is added to ensure the model reflects the changing direction of wire transformation. Thus, the Jacobian of the system state update function is changed at each timestep to match the wire transformation direction. The goal of implementing the EKF to this control system is to provide a better estimate for joint deflection angles than can be provided by the encoder, which is limited by its resolution. While a low-pass filter could effectively filter out encoder noise, the EKF also provides insight into states of the system that cannot be easily measured.

The state vector, $\mathbf{x}$, is defined as the actuator wire's stress, temperature, phase, and actuator angle. For the remainder of §4.3.7, the subscript n defining the joint number of the actuator is omitted for clarity, as all variables in this section share the same joint number.

$$\mathbf{x} = \begin{bmatrix} \sigma & T & \xi & \theta_a \end{bmatrix}^\intercal$$

The input vector, $\mathbf{u}$, is simply the voltage supplied by the low-level controller in §4.4.1, V, squared in Eq. (4.24).

$$\mathbf{u} = V^2 \tag{4.24}$$

At each timestep, the EKF calculates the estimated state, $\hat{\mathbf{x}}$, from the previous state and input vector through the state transition function, f, as defined in Eq. (4.25) [94].

$$\hat{\mathbf{x}}_{k|k-1} = f(\hat{\mathbf{x}}_{k-1}, \mathbf{u}_{k-1}) \tag{4.25}$$

The state transition function, f, updates each state at a rate of 100 Hz using the derivative of the state matrix, $\mathbf{dx}_{k-1}$, which is defined in matrix form in Eq. (4.28). The wire stress derivative is defined in Eq. (4.9), the wire phase derivative is defined in Eq. (4.6), and the temperature derivative is defined in Eq. (4.4). The derivative of the joint angle is calculated from the relationship of the spring deflection and stress, defining it to be a ratio of the wire cross-sectional area, mounting radius, number of wires, and angular spring coefficient. The motion of the central component is treated as a system input, as shown in Eq. (4.26). To represent the difference in definitions for $\dot{\theta}_a$ for clockwise and counterclockwise actuators, Eqs. (4.28) and (4.30) include a sign term S, where $S = 1$ for a clockwise actuator and $S = -1$ for a counterclockwise actuator.

$$\dot{\theta}_a = \begin{cases} \dot{\theta}_C + \dot{\sigma}\frac{a_w r N_w}{K} & \text{if clockwise} \\ \dot{\theta}_C - \dot{\sigma}\frac{a_w r N_w}{K} & \text{if counterclockwise} \end{cases} \tag{4.26}$$

$$\mathbf{dx}_{k-1} = \begin{bmatrix} \dot{\sigma} & \dot{T} & \dot{\xi} & \dot{\theta}_a \end{bmatrix}^\intercal \tag{4.27}$$

$$\mathbf{dx}_{k-1} = \begin{bmatrix} 0 & \Theta & \Omega & \frac{E\pi r}{180 L_w} \\ 0 & 0 & 0 & 0 \\ 0 & \xi_T(T,\sigma) & 0 & \xi_\sigma(T,\sigma) \\ S\frac{a_w r N_w}{K} & 0 & 0 & -1 \end{bmatrix} \begin{bmatrix} \dot{\sigma} \\ \dot{T} \\ \dot{\xi} \\ \dot{\theta}_a \end{bmatrix} + b \tag{4.28}$$

$$b = \begin{bmatrix} 0 \\ \frac{V^2/R - h(T)A_w(T - T_{amb})}{m_w c_p} \\ 0 \\ \dot{\theta}_C \end{bmatrix} \tag{4.29}$$

This equation can be rearranged to the form $\mathbf{Adx} = \mathbf{b}$ as below, and can then be

solved for $\mathbf{dx}$ in the form $\mathbf{dx} = \mathbf{A}^{-1}\mathbf{b}$.

$$\begin{bmatrix} -1 & \Theta & \Omega & \frac{E\pi r}{180L_w} \\ 0 & -1 & 0 & 0 \\ 0 & \xi_T(T,\sigma) & -1 & \xi_\sigma(T,\sigma) \\ S\frac{a_w r N_w}{K} & 0 & 0 & -1 \end{bmatrix} \begin{bmatrix} \dot{\sigma} \\ \dot{T} \\ \dot{\xi} \\ \dot{\theta}_a \end{bmatrix} = b \tag{4.30}$$

While only $\dot{T}$ and $\dot{\xi}$ directly include state variables, $\dot{\sigma}$ and $\dot{\theta}_a$ are functions of $\dot{T}$ and $\dot{\xi}$, and therefore are also functions of state variables. The structure of the Jacobian, $\mathbf{F}_k$, of the state transition function, f, is shown in Eq. (4.31). Individual elements of the Jacobian are solved symbolically and are shown in Appendix B.

$$\mathbf{F}_k = \begin{bmatrix} J_{11} & J_{12} & 0 & 0 \\ 0 & J_{22} & 0 & 0 \\ J_{31} & J_{32} & 0 & 0 \\ J_{41} & J_{42} & 0 & 0 \end{bmatrix} \tag{4.31}$$

The predicted covariance estimate $\mathbf{P}_{k|k-1}$ is defined by the state transition matrix, $\mathbf{F}_k$, previous covariance estimate, and process covariance, $\mathbf{Q}_{k-1}$, as shown in Eq. (4.32) [94].

$$\mathbf{P}_{k|k-1} = \mathbf{F}_k \mathbf{P}_{k-1|k-1} \mathbf{F}_k^\intercal + \mathbf{Q}_{k-1} \tag{4.32}$$

In the update phase, the residual covariance, $\mathbf{S_k}$, is calculated from the observation matrix Jacobian, $\mathbf{H}_k$, and measurement covariance, $\mathbf{R}_k$, in Eq. (4.33) [94]. In this case, the measurement matrix, $h(\hat{\mathbf{x}}_{k|k-1})$, is defined as

$$h(\hat{\mathbf{x}}_{k|k-1}) = \begin{bmatrix} 0 & 0 & 0 & 1 \\ 1 & 0 & 0 & 0 \\ 0 & 0 & 1 & 0 \end{bmatrix}$$

$$\mathbf{S_k} = \mathbf{H}_k \mathbf{P}_{k|k-1} \mathbf{H}_k^\intercal + \mathbf{R}_k \tag{4.33}$$

The measurement matrix, $\mathbf{z}_k$, is defined as the observable or calculable states of the system. In this case, since actuator angle and stress are both directly measured, the wire phase can also be measured indirectly.

Wire stress is estimated as:

$$\sigma = \begin{cases} K\phi_{CW} & \text{if clockwise} \\ K\phi_{CCW} & \text{if counterclockwise} \end{cases} \tag{4.34}$$

The total wire strain ϵ, is calculated from the joint kinematics in Eq. (4.10) (presented again below) and then separated into the reversible SMA wire transformation strain ϵ_t and elastic wire strain ϵ_s in Eqs. (4.35) and (4.36).

$$\epsilon = \frac{\pi r}{180L}\theta_a$$

$$\epsilon_s = \frac{\sigma}{E} \tag{4.35}$$

$$\epsilon_t = \theta_a \frac{\pi r}{180L} - \phi\frac{K}{E} \tag{4.36}$$

Finally, given the maximum wire strain ϵ_m and the phase to transformation strain relationship, the phase of the wire can be indirectly measured using in Eq. (4.37). This provides the final observation matrix in Eq. (4.38).

$$\xi = \theta_a \frac{\pi r}{180L\epsilon_m} - \phi\frac{K}{E\epsilon_m} \tag{4.37}$$

$$\mathbf{z}_k = \begin{bmatrix} K\phi \\ 0 \\ \theta_a \frac{\pi r}{180L\epsilon_m} - \phi_n \frac{K}{E\epsilon_m} \\ \theta_a \end{bmatrix}^\intercal \tag{4.38}$$

The innovation residual, $\tilde{\mathbf{y}}_k$, and Kalman gain, $\mathbf{K}_k$, are defined by Eqs. (4.39) [94] and (4.40) [94].

$$\tilde{\mathbf{y}}_k = \mathbf{z_k} - h(\hat{\mathbf{x}}_{k|k-1}) \tag{4.39}$$

$$\mathbf{K}_k = \mathbf{P}_{k|k-1}\mathbf{H}_k^\intercal \mathbf{S}_k^{-1} \tag{4.40}$$

The last step of the filter updates the state and covariance estimates for timestep k using the identity matrix Iin Eqs. (4.41) [94] and (4.42) [94].

$$\mathbf{x}_{k|k} = \hat{\mathbf{x}}_{k|k-1} + \mathbf{K}_k\tilde{\mathbf{y}}_k \tag{4.41}$$

$$\mathbf{P}_{k|k-1} = (\mathbf{I} - \mathbf{K}_k\mathbf{H}_k)\mathbf{P}_{k|k-1} \tag{4.42}$$

4.3.8 Path Planning

The path planning algorithm is used during position and orientation tracking tests. Given a series of waypoints, $\mathbf{W}$, defined by end-effector X-positions, $\mathbf{X}_w$, Y-positions, $\mathbf{Y}_w$, end-effector angle, $\boldsymbol{\theta}_{EE,w}$, and time, $\mathbf{t}_w$, a set of desired joint angles are determined using the following method. Each waypoint is defined by an end-effector X and Y-position, orientation, and time in equation (4.43).

$$\mathbf{W} = \begin{bmatrix} \mathbf{X}_w & \mathbf{Y}_w & \boldsymbol{\theta}_{EE,w} & \mathbf{T}_w \end{bmatrix} \tag{4.43}$$

Joint positions, $\mathbf{q}$, for each waypoint are calculated using the inverse kinematics algorithm described in §4.3.5 from the end-effector position and orientation defined by the waypoint. Then, a minimum-jerk trajectory is generated to determine the intermediate joint angles between each waypoint. For each segment of the path between two waypoints, N and $N+1$, time is normalized between starting time t_f and ending time t_0, to normalized time γ in equation (4.44).

$$\gamma = \frac{t - t_0}{\Lambda}, \text{where } \Lambda = t_f - t_0 \tag{4.44}$$

On each segment, a minimum-jerk trajectory is applied to each joint. The minimum jerk trajectory is defined in Equation (4.45) [67].

$$s(\gamma) = 10\gamma^3 - 15\gamma^4 + 6\gamma^5 \tag{4.45}$$

The first and second derivatives of this trajectory with respect to time are defined in Equations (4.46) and (4.47).

$$\dot{s}(\gamma) = \frac{30\gamma^2 - 60\gamma^3 + 30\gamma^4}{\Lambda} \tag{4.46}$$

$$\ddot{s}(\gamma) = \frac{60\gamma - 180\gamma^2 + 120\gamma^3}{\Lambda^2} \tag{4.47}$$

To create the final joint space paths and their derivatives, $s(\gamma)$, $\dot{s}(\gamma)$, and $\ddot{s}(\gamma)$ are multiplied by $\mathbf{q}(N+1) - \mathbf{q}(N)$ to project the minimum jerk trajectory to the desired joint ranges.

4.4 Arm and Actuator Control

This section outlines the three modes of control used to test the robotic arm performance: two that rely on the compliant joint and one that is commonly used in the literature as a method of comparison. A total of four controllers are introduced. The low-level position control tracks the desired deflection of a single SMA actuator. The mid-level controller feeds a desired deflection to the clockwise and counterclockwise actuators that is calculated from a desired joint torque. Finally, two high-level controllers are defined, both of which provide desired joint torques to each of the three joints. The high-level position controller determines this torque using a PID controller, while the high-level impedance controller determines the desired torque based on the impedance controller constants. The structure of the impedance control system is shown in Fig. 4.7 and the position control system is shown in Fig. 4.8. Finally, a common antagonistic controller is defined in order to compare it against the multi-level position controller.

4.4.1 Low-Level Actuator Position Control

Low-level control of each actuator seeks to drive the measured deflection of each half of the compliant joint, $\boldsymbol{\phi}_m$, to a desired angle, $\boldsymbol{\phi}_d$, by applying a voltage $\mathbf{V}$ to each wire. The maximum voltage applied by this controller is limited to prevent overheating and damaging the wire. The applied voltage is determined using a PID controller defined in Eq. (4.48) with proportional gains, $\mathbf{K_p}$, integral gains, $\mathbf{K_i}$, and derivative gains,

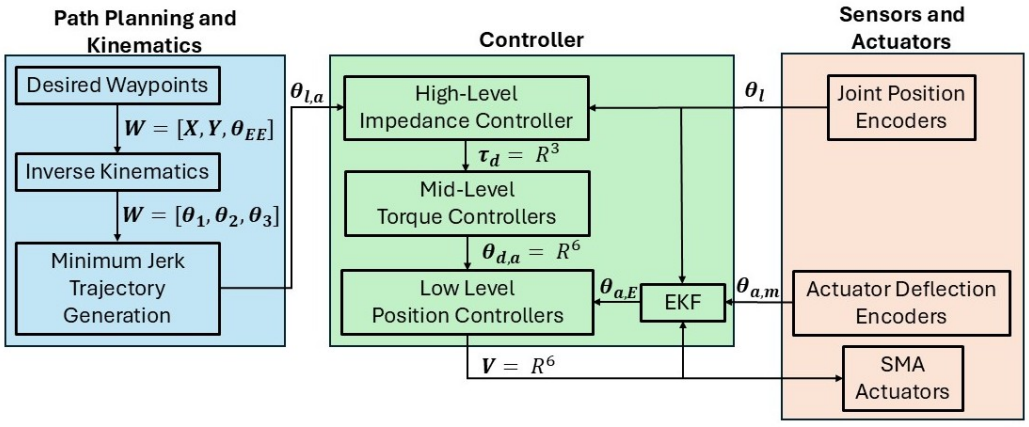

Figure 4.7: Arm control structure for impedance control showing the interaction between path planning, controller, and sensor and actuator components

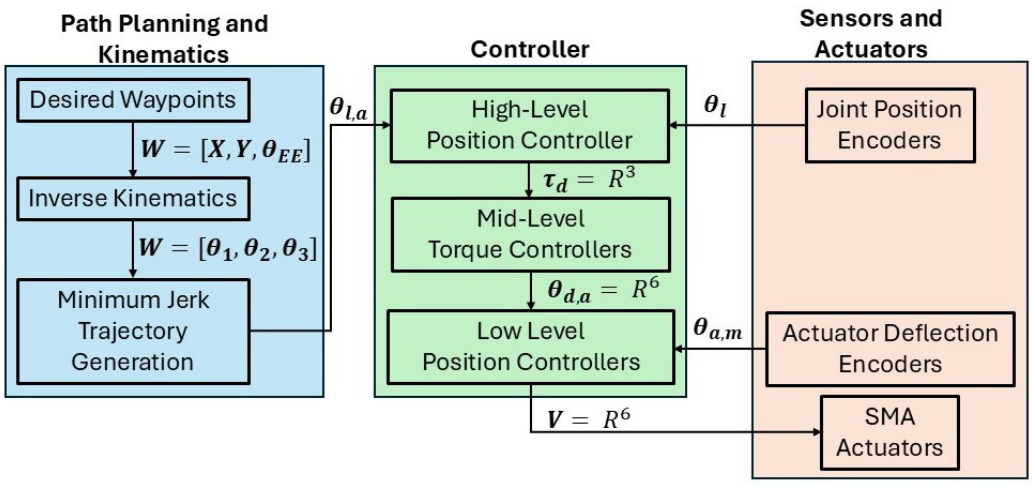

Figure 4.8: Arm control structure for path following position control showing the interaction between path planning, controller, and sensor and actuator components

$\mathbf{K_d}$, where

$$\mathbf{V} = \mathbf{K_p}(\phi_d - \phi_m) + \mathbf{K_i}\sum_{i=1}^{k}(\phi_d(i) - \phi_m(i)) + \mathbf{K_d}\dot{\phi}_m \tag{4.48}$$

and $\dot{\phi}_m$ is approximated in Eq. (4.49) at timestep k as:

$$\dot{\phi}_m = \frac{\phi_m(k) - \phi_m(k-1)}{t_s} \tag{4.49}$$

Controller gains for the low-level controller are:

$$\mathbf{K_p} = \begin{bmatrix} 22 & 22 & 22 \end{bmatrix}^\intercal$$

$$\mathbf{K_i} = \begin{bmatrix} 0.025 & 0.025 & 0.025 \end{bmatrix}^\intercal$$

$$\mathbf{K_d} = \begin{bmatrix} 2 & 2 & 2 \end{bmatrix}^\intercal$$

If the low-level controller is being used for the impedance controller, the EKF described in §4.3.7 replaces the measured deflections ϕ_m in the above equations with the estimated deflection ϕ_e, which is defined by the difference between the center component angle, θ_c, and actuator angle, θ_a, in Eq. (4.50).

$$\phi_e = |(\theta_c - \theta_a)| \tag{4.50}$$

Similar to the work in Chapter 3, the hysteresis of the SMA wire is managed by the feedback control of the low-level controller. Feedback control has been used

without a hysteresis model to effectively manage the errors introduced by hysteresis in previous works [6, 7]. This work similarly observed low errors in the experimental results to be discussed in §4.6.

4.4.2 Mid-Level Joint Torque Control

The compliant joint allows for two extensions of traditional SMA wire control. First, it allows for easy control of both wires simultaneously. In a stiff, antagonistic actuator, only the net torque provided by the two actuators can be measured. The deflection of each half of the actuator provides a simple measurement of wire strain and stress, allowing for measurements to be used in individual controllers. Second, the springs within the joint transform wire stress control, normally a complex task requiring simulation, into simple position control, which is much more easily achieved. The decomposition of torque control into separate position controllers is defined in the following equations.

To keep both wires active, a minimum desired deflection angle is defined as ϕ_{min}. For a positive desired torque $\tau_{cmd,n}$, the desired deflections for the clockwise and counterclockwise actuators are defined in Eq. (4.51) by:

$$\begin{bmatrix} \phi_{CW,n} \\ \phi_{CCW.n} \end{bmatrix} = \begin{cases} \begin{bmatrix} \phi_{min} \\ \frac{\tau_{cmd}}{K_n} + \phi_{min} \end{bmatrix} & \text{if } \tau_{cmd,n} \geq 0 \\ \begin{bmatrix} \frac{\tau_{cmd}}{K_n} + \phi_{min} \\ \phi_{min} \end{bmatrix} & \text{if } \tau_{cmd,n} < 0 \end{cases} \tag{4.51}$$

The addition of the secondary wire controller targeting a deflection of ϕ_{min} is a simple method of preventing wire slack from occurring while ensuring that wires are not overstressed. For joint n, the measured joint torque used to evaluate the efficicey of the following controllers is defined by Eq. (4.52).

$$\tau_n = K_n(\phi_{CW,n} - \phi_{CCW,n}) \tag{4.52}$$

4.4.3 High-Level Position Control

One mode of operation of the arm is position and orientation control of the end-effector, which follows a path defined by the path planning algorithm. This mode uses a high-level PID controller to drive the measured joint angle, q_m, to a desired joint

angle, q_d. The controller output is the desired joint torque, which is fed into the mid- and low-level controllers defined previously to determine the voltage applied to each actuator. The desired torque of the controller is determined based on proportional gain, $\mathbf{K_{pg}}$, integral gain,$\mathbf{K_{ig}}$, and derivative gain, $\mathbf{K_{dg}}$, and is described in Eq. (4.53).

$$\boldsymbol{\tau} = \mathbf{K_{pg}}(\mathbf{q_d} - \mathbf{q_m}) + \mathbf{K_{ig}} \sum_{i=1}^{k} (\mathbf{q_d}(i) - \mathbf{q_m}(i)) + \mathbf{K_{dg}}\dot{\mathbf{q}}_m \tag{4.53}$$

This method of control has several advantages when compared to traditional antagonistic SMA control methods. First, this multi-level control method eliminates slack from the wires. Since each actuator is tasked with maintaining a minimum deflection, neither actuator's wires slacken. This eliminates the potential for a slack wire to short-circuit with another actuator. Second, by maintaining the minimum deflection, each actuator is kept within the wire's range of transformation temperatures at all times. This dramatically reduces the delay imposed by traditional antagonistic actuators when changing directions by removing the time the wire takes to heat from room temperature to its transformation temperature.

4.4.4 Joint Space Impedance Controller

Impedance control is a method that combines position and torque control into a single controller. A virtual spring/damper is applied to each joint of the robotic arm, which determines a desired joint torque. This results in compliant behaviour, as the arm allows itself to be moved in a predetermined, controlled manner when external forces are applied. The commanded joint torque is calculated from the virtual spring coefficients, $\boldsymbol{\kappa}$, damping coefficients $\boldsymbol{\beta}$, and gravity compensation torque $\mathbf{G}$ as described in equation (4.54) [67]. Inertial terms are omitted due to the relatively low acceleration of the SMA-actuated arm.

$$\boldsymbol{\tau}_{cmd} = \boldsymbol{\kappa}(\mathbf{q}_d - \mathbf{q}_m) + \boldsymbol{\beta}(\dot{\boldsymbol{q}}_d - \dot{\boldsymbol{q}}_m) + \mathbf{G} \tag{4.54}$$

To prevent wire overstress, a torque limit, $\boldsymbol{\tau}_l$, is defined. At every timestep k, Eq. (4.55) limits the commanded torque to a predefined limit based on a wire stress of 180 MPa.

$$\tau_{cmd,n} = \begin{cases} \tau_{cmd,n} & \text{if } \tau_{cmd,n} < \tau_{l,n} \\ \tau_{l,n} & \text{if } \tau_{cmd,n} \geq \tau_{l,n} \end{cases} \tag{4.55}$$

4.4.5 Antagonistic Control

Traditional antagonistic SMA actuator control methods are used in this paper as a method of comparison. This controller alternates the active wire between the clockwise and counterclockwise actuators. With this method, the low-level controller is disabled, and actuator voltages are applied based only on joint error. The PID controller with gains $\mathbf{K_{pa}}$, $\mathbf{K_{ia}}$, and $\mathbf{K_{da}}$ is described in Eq. (4.56).

$$\mathbf{V} = \mathbf{K_{pa}}(\mathbf{q_d} - \mathbf{q_m}) + \mathbf{K_{ia}} \sum_{i=1}^{k} (\mathbf{q_d}(i) - \mathbf{q_m}(i)) + \mathbf{K_{da}} \dot{\mathbf{q}}_m \tag{4.56}$$

Antagonistic behaviour is achieved through a switching behaviour that applies voltage to only one actuator per joint at a time. This behaviour is mathematically described in Eq. (4.57).

$$\begin{bmatrix} V_{cw} \\ V_{ccw} \end{bmatrix} = \begin{cases} \begin{bmatrix} V \\ 0 \end{bmatrix} \text{ if } V \geq 0 \\ \\ \begin{bmatrix} 0 \\ V \end{bmatrix} \text{ if } V < 0 \end{cases} \tag{4.57}$$

4.5 Experimental Design

This section defines the tests used to evaluate the performance of each controller and to validate the torque measurement of the compliant joints.

4.5.1 Test 1: Low-Level Controller Step Responses

First, the performance of the low-level actuator position controller is evaluated. The low-level controller drives the angular deflection of a single joint to a desired angle. To prevent the arm from moving during the test, the joint's load component is held at an angle of 0° using a stiff wire. Then, a series of step responses are provided as target angles with a magnitude of 1° spaced 5 s apart, with an additional 5 seconds added to the first step to allow the wire to warm from room temperature. The controller performance is evaluated by the steady-state angular error, with results shown in Figure 4.9.

4.5.2 Test 2: Mid-Level Controller Torque Tracking

Second, the performance of the mid-level joint torque controller is evaluated by providing a sinusoidal target torque. The sinusoidal path has a period of 20 s and amplitude of 1.2 Nm, with an offset of 0.15 Nm. The controller is evaluated based on the root-mean-square-error (RMSE) of torque error, which is determined from the joint deflection as measured by the encoder. The low deflection angles ($< 5°$) allow for a linear relationship between deflection and torque to be used. The results of the joint 1 torque tracking are discussed and displayed in Figure 4.10.

4.5.3 Test 3: Torque Measurement Validation

To ensure that the measured joint torque matches the actual torque applied to it, a series of static tests were conducted. For each test, the joint is commanded to apply a torque equal to the torque that would be applied by a mass after compensating for the arm's own mass. Then, once the arm reached a steady-state angle as expected, the torque measured by the joint is recorded. The measured torques are tared by the measured torque with no mass to account for static friction. Tests were repeated with masses in increments of 100 g up to 400 g, as shown in Figure 4.11.

4.5.4 Test 4: High-Level Position Control and Comparison

A comparison is conducted between the proposed multi-level position controller and traditional antagonistic control methods. A sinusoidal target path is provided for the first arm joint with an amplitude of 35° and period of 20 s. Each controller is then instructed to follow this desired path, and their performances are evaluated on their RMSE, maximum error, and the time each requires to reach the desired path.

4.5.5 Test 5: End-Effector Position and Orientation Tracking

The high-level position and orientation controller is evaluated in a path-tracking test. Starting and ending waypoints are provided, and the end-effector position and orientation errors are measured at each timestep. The controller is then evaluated based on the RMSE of the end-effector position and orientation.

4.5.6 Test 6: Impedance Control

Finally, the impedance controller testing is completed. A step response is provided to the desired joint angles and the arm is allowed to move with no external forces. The step response is provided to move the end-effector to the point $X = 0.25$ m, $Y = -0.3$ m, $q_{EE} = -90°$ with gains $\boldsymbol{\kappa} = \begin{bmatrix} 0.1 & 0.1 & 0.02 \end{bmatrix}^\intercal$ and $\boldsymbol{\beta} = \begin{bmatrix} 0.04 & 0.04 & 0.003 \end{bmatrix}^\intercal$. The steady-state error is then measured once the arm motion is completed. Then, at 25 s, a force is manually applied to the end-effector by pushing the end-effector to a new point to provide a deflection to each joint angle. The controller's response to the applied force is measured by the RMSE between the controller's target and measured torque, and EKF internal states are recorded.

4.6 Results and Discussion

This section documents a series of tests measuring the performance of each level of the controller. First, the low-level actuator position controller is evaluated, followed by the mid-level torque controller. The measured torque is then validated in a series of tests using a static mass. Then, a comparison between the proposed multi-level controller and traditional antagonistic controllers is performed. Finally, the full impedance controller is tested and its performance is evaluated.

4.6.1 Low-Level Actuator Position Control

First, the efficacy of the low-level controller is evaluated through a series of step response tests. The low-level controller seeks to drive the relative angle of one actuator of the compliant joint to a desired position. For these tests, joint 1 is mechanically fixed in position so that only the joint deflection changes. Figure 4.9 shows the low-level controller applied to a series of sequential step responses, each increasing or decreasing the target angle by 1°. PID gains were determined by manual tuning based on experimental results. The position controller demonstrated excellent performance with an average steady-state error of 0.017° and maximum steady-state error of 0.04° across all step responses between 1 and 4°, which approaches the encoder resolution of 0.02°. Larger steady-state errors were observed at lower deflection angles, which are avoided in future experiments by the introduction of the minimum deflection target.

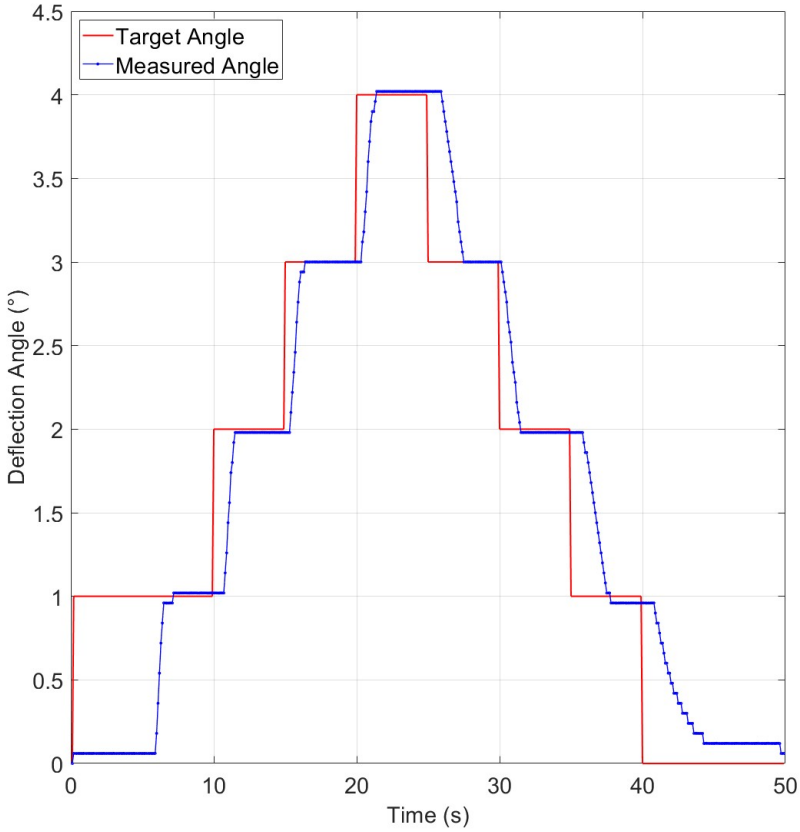

Figure 4.9: Low-level controller step responses for $K_p = 22$, $K_i = 0.025$, $K_d = 2$

4.6.2 Mid-Level Joint Torque Control

The mid-level controller for each joint tracks a desired joint torque over time. To measure the torque tracking ability of the controller, a sinusoidal target torque is provided to joint 1 at an angle of 0°, as shown in Figure 4.10. The root-mean-square error (RMSE) of target torque is calculated from the encoder deflection over one full cycle of the sinusoidal path and was measured to be 0.04 Nm, or only 2.3 % of the joint's maximum torque. The highest errors occur at the start of the test and when switching directions. The initial joint error occurs because of the imprecise starting procedure, which targets a small actuator deflection to preheat the wires. The error observed when the joint changes direction is due to the delay created by the integral term of the low-level controller. A smaller integral gain could reduce this effect, but would also increase error during the rest of the test. Preheating the wires would also improve the behaviour of the tracking during the early stages of the test. While a comparison with other SMA-actuated torque controllers is not feasible given the

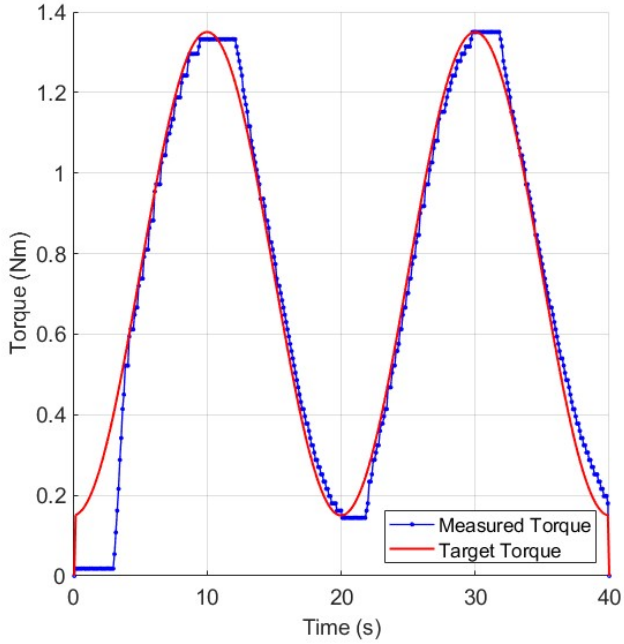

Figure 4.10: Mid-level torque controller tracking a desired sinusoidal torque for joint 1.

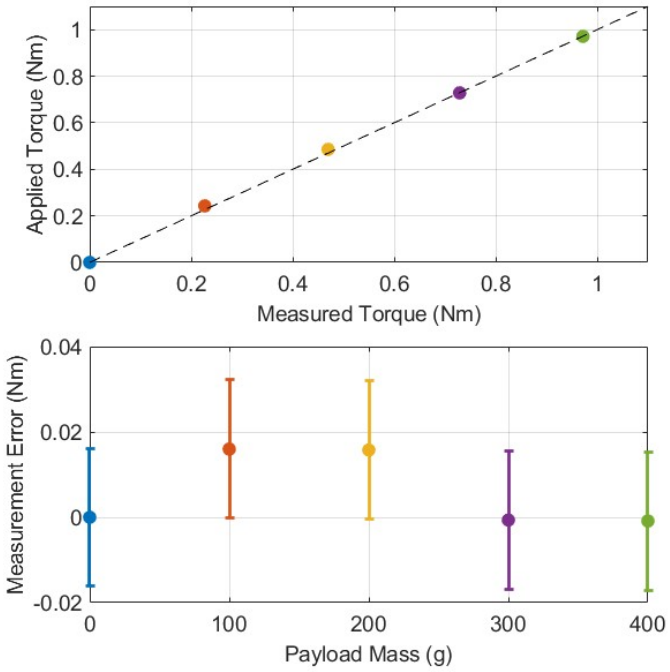

Figure 4.11: Actuator torque validation and error measurement for joint 2 using masses ranging from 0-400 g

wide ranges of applied torque, this performance meets expectations given the system's relatively low sensing resolution of 0.016 Nm.

The torque measurements of the joint are validated in a series of static measurement tests. Across all tests, the arm maintained its desired holding position of 45° with less than 0.1° error, demonstrating that the gravity compensation term properly accounts for the mass of the arm. With the arm's position kept constant, the measured torques and the measurement residuals with error bars are recorded and plotted in Fig. 4.11. A line with a slope of 1 is plotted to compare measured data to ideal measurements. The low measurement errors support the previous assumption that a linear spring approximation is valid.

4.6.3 High-Level Position Control

The proposed multi-level control method described in §4.4.3 is compared to traditional SMA antagonistic control methods, described in §4.4.5. A full cycle of a sinusoidal path with a period of 20 s is provided as a target joint position for each controller. The comparison between these two methods of control is shown in Figure 4.12 and an evaluation of their performance is described in Table 4.3.

The multi-level controller resulted in a 3-fold reduction in angular position error when compared to traditional antagonistic control, and exhibited less lag from the signal input. Both controllers experienced a larger error between 7.5 and 10 s as the joint approaches its maximum angle, where more force is required to reach. The multi-level controller's starting error of 2.3° is due to the controller's starting sequence (not shown), which keeps both actuators in tension but does not use feedback control to maintain a desired angle. Despite this initial error, the multi-level controller crosses the target path and begins small oscillations within 2.8 s, while the antagonistic controller takes a full 7.5 s. Similarly, the multi-level controller reaches the target path within 1.8 s after changing direction, while the antagonistic controller requires 3.9 s. In summary, the proposed controller performed significantly better than the

Table 4.3: Evaluation of Multi-Level and Antagonistic Position Controllers

Measurement	Multi-Level Controller	Antagonistic Controller
Root-Mean-Square Error (°)	1.7	6.3
Maximum Error (°)	3.9	20.6
Time to Bounded Tracking Error (s)	2.8	7.5

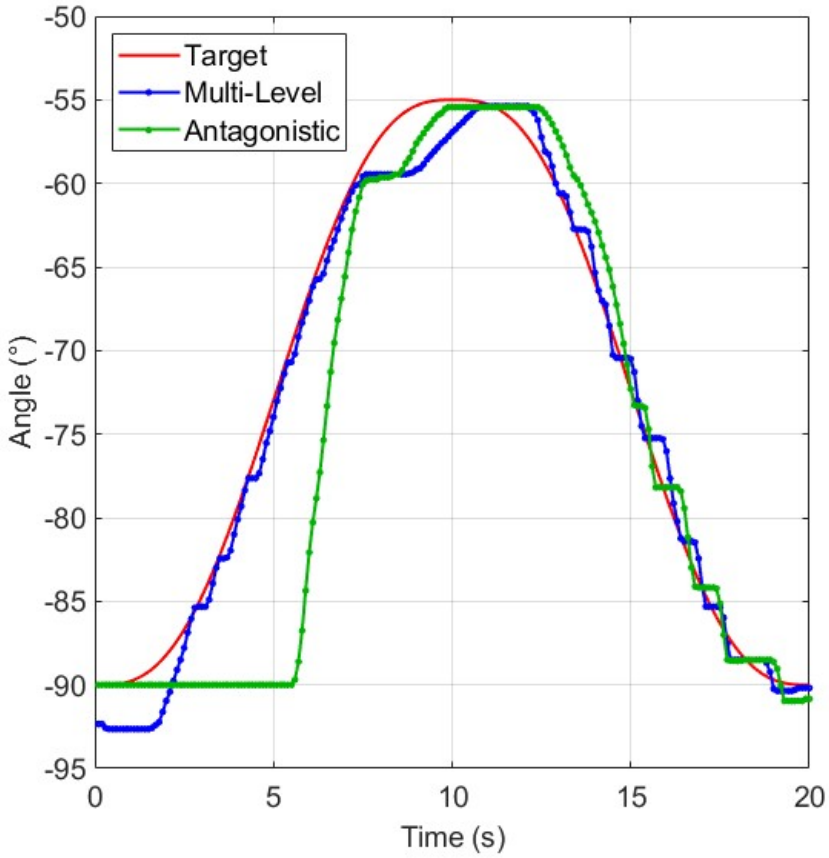

Figure 4.12: Multi-level (blue) and antagonistic (green) controller comparison for a sinusoidal path-following test.

antagonistic controller when measured by RMSE and time to reach the desired path when starting or switching directions. A summary of these metrics is included in Table 4.3.

For demonstration, the multi-level position controller is used in an end-effector path-following test using the path-planning algorithm described in §4.3.8. The results of this experiment are shown in Fig. 4.13 and summarized in Table 4.4. While the measured errors are larger than those in a previous work by the authors in [26], they are similar to those in other SMA-actuated robotic arms [7]. However, larger errors are expected given the larger workspace and faster motion of the end-effector in this experiment.

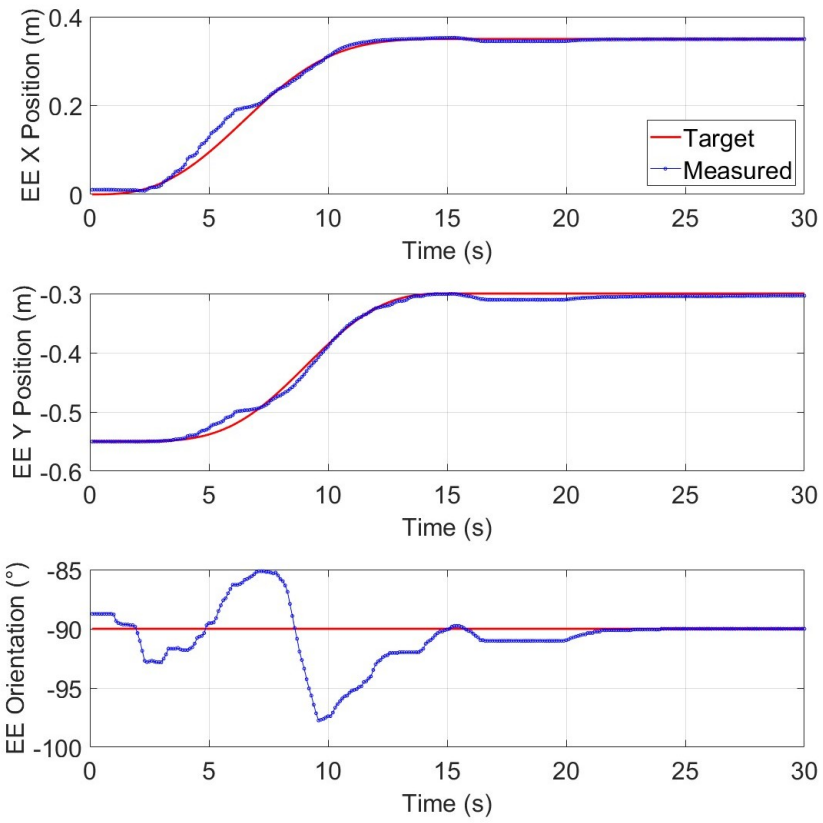

Figure 4.13: End-effector (EE) position and orientation tracking results provided a path across the arm's workspace.

Table 4.4: End-Effector Position and Orientation Tracking Results

Measurement	Position (cm)	Orientation (°)
Root-Mean-Square Error	1.3	2.5
Maximum Error	4.7	7.7
Steady-State Error	0.36	0

4.6.4 High-Level Impedance Control

The high-level impedance control seeks to achieve compliant behaviour in the robotic arm by determining a desired joint torque from that joint's angular position and velocity. While an arm with an impedance controller will push more strongly the further it is from its target, the amount it "pushes" is controlled and limited, unlike the behaviour of a PID controller.

The results of testing the joint space impedance controller are shown in Figure 4.14. While the controller shows some steady-state position error, this is expected given the relatively low gains used and lack of an integral correction term in

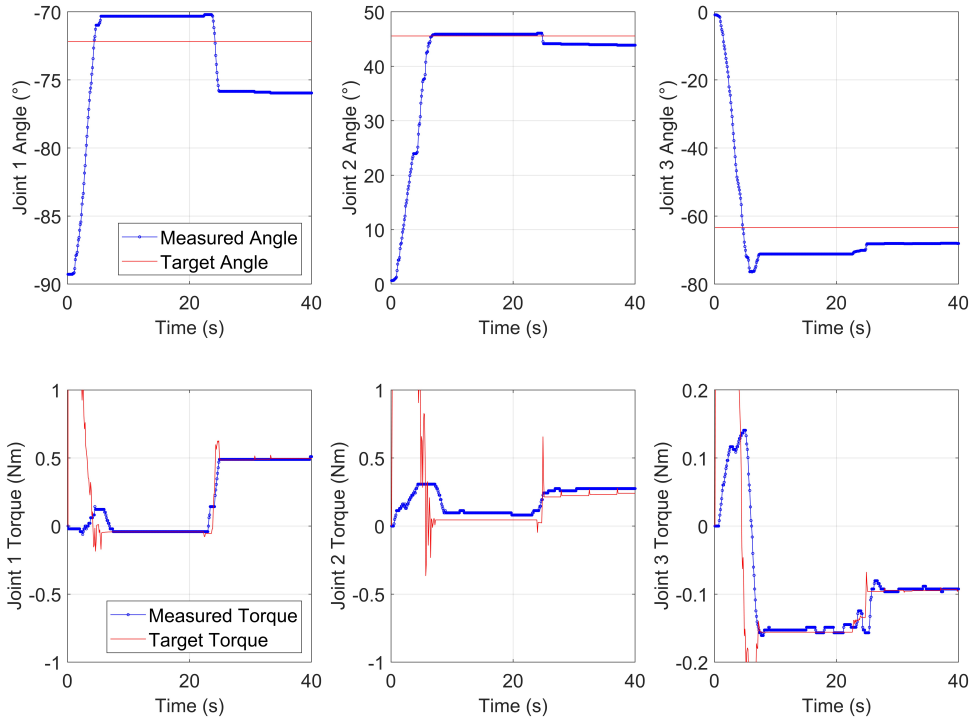

Figure 4.14: Joint space impedance controller results displaying joint angles (top row) and joint torques (bottom row). A disturbance is manually applied at 25 seconds.

Table 4.5: Impedance Controller Steady-State Torque Errors

Measurement	Joint 1	Joint 2	Joint 3
Steady-State Torque Error (Nm)	0.013	0.034	0.002
Steady-State Torque Error (% of maximum)	0.8	2.1	0.0

impedance controllers. At around 25 s, the end-effector is manually moved to a new setpoint, resulting in a corresponding increase in desired joint torques. The controller shows excellent adjustment to the applied force, reaching a new steady-state torque for each joint in roughly three seconds. This is remarkably fast for the chosen SMA wire, which requires at least 6 seconds to cool and transform. These results highlight the advantage of the compliant actuator, which allows for one actuator to quickly heat before the other has finished cooling. The steady-state torque error is also extremely low for an SMA-actuated system, as summarized in Table 4.5. For joint 3, the steady-state error is too small for the sensor resolution to detect. Note that the step provided in target position necessarily results in unreachable target torques for the first few seconds of the experiment.

4.6.5 EKF Results

The measurable EKF states: wire stress and phase, alongside actuator angle, are shown during the impedance controller test in Figure 4.15. For brevity, only results for the clockwise and counterclockwise actuators within joint 2 are displayed given the high number of states represented by all six estimators. The results show that noise in angular measurements are correctly propagated to estimates of stress and phase. Additionally, it is shown that one wire contracts and one extends, as represented by

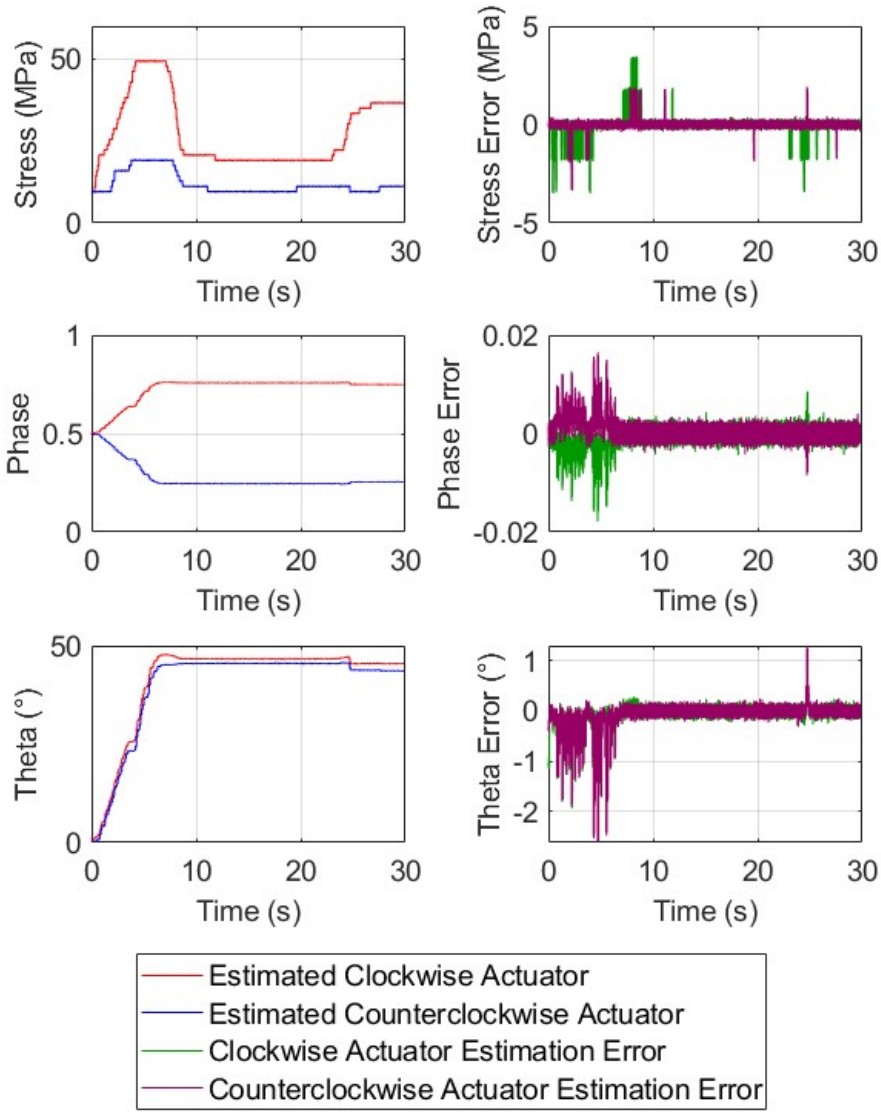

Figure 4.15: Plots of estimated wire stress and phase, and actuator angle for joint 2 during the impedance control tests. Error plots display the difference between estimated and measured states.

the diverging phase plots in Fig. 4.15.

While tests of the impedance control that used direct measurements of wire stress performed very similarly to those using estimated stress, more complex controllers or future works with noisier sensors would likely benefit further from the proposed EKF formulation. Few direct conclusions of the efficacy of the EKF can be made at this time, but it serves as a practical and useful extension of existing SMA state estimation projects.

4.7 Conclusion

In this chapter, a novel control strategy for an SMA-actuated robotic arm is introduced. Compliant joints are integrated into a 3-DOF, 6-actuator robotic arm. These compliant joints allow for simultaneous control of both the clockwise and counter-clockwise actuators and provide a direct measurement of applied joint torque. A multi-level controller is designed that controls both wires to eliminate wire slack and maintain wires in a pre-heated state, resulting in improved position tracking performance when compared to traditional antagonistic control. Performance could be further improved through an investigation and optimization of the heat transfer of wires within the SMA bundle. Additionally, a framework for implementing an EKF for each actuator with the simulated dynamics of the robotic arm is introduced and applied to a high-level impedance controller. While the addition of the EKF did not substantially improve controller results, it serves as a demonstration of experimentally integrating state estimation techniques into complex, SMA-actuated systems. The final result is a robotic arm actuated by SMA wires that is capable of interacting compliantly with its environment, a capability that has not been demonstrated in existing works. This behaviour allows the robotic arm to interact with its environment in a controlled and predictable manner, which is ideal for delicate aerial manipulation tasks. Future work could implement temperature sensing strategies to further verify the EKF performance, or extend the joint-space impedance controller to a task-space controller.

Chapter 5

Conclusion

In this thesis, an SMA-actuated robotic arm was developed that makes two key contributions to SMA-actuated robotics.

First, two SMA-actuated arm designs with improved strength, range, and degrees of freedom are introduced. The first arm was designed using multiple rollers to increase the length of the SMA wires within the confines of the arm link. The forces applied by these actuators were calculated and used for topology optimization of the two arm links, which resulted in a mass reduction of 661.3 g. The resulting arm has a mass of only 546.3 g, 399 g of which comprises the mechanical structure of the arm. The arm was able to manipulate a mass of 300 g, roughly, three quarters the mass of the arm itself. The combined mass of the arm, electronics, and 300 g payload of 846.3 g is well within the payload capacity of small to medium sized drones. The second design integrates SMA actuators within the arm frame instead of within the arm links, keeping the wires at a static angle. This design has a heavier base, but significantly less inertia in the arm links. A novel compliant joint design is introduced that couples each actuator to the robotic arm by a set of springs, providing mechanical compliance as well as allowing for the introduction of new controllers.

Second, a novel bidirectional position controller is introduced and applied to an impedance controller. This controller achieves a desired joint torque by determining the required deflections between each actuator and the load component. This allows for both the clockwise and counterclockwise actuators to maintain tension at all times, significantly improving position tracking control while providing direct measurements of joint torque. These joint torque measurements were used in the first experimentally achieved impedance control of an SMA-actuated robotic arm.

Third, an extended Kalman filter is implemented into the controller, providing an estimated state for each wire's stress, phase, temperature, and angle. A novel

formulation of the EKF state transition function is developed to account for the external dynamics of the robotic arm and the influence of each actuator on the others. The EKF was found to accurately track the measured states and the modeled sensor noise did not measurably impact the controller's performance. The low impact of the EKF indicates that a simpler filter, such as a low pass filter, may be sufficient for impedance control tasks.

This work highlights multiple opportunities for future research in SMA-actuated robotic arm control. It has shown that the application of SMA actuators to robotic systems, in some cases, results in significant reductions in the recoverable strain of antagonistic actuators. These results suggest that a further study on the effect of roller radius, number, and material would improve the capacity and reliability of SMA-actuated systems. A general model of strain reduction over rollers would make these systems more robust and would increase the fidelity of SMA actuator simulations. Further studies could also investigate the performance degradation of the SMA actuator in an applied setting, where the effect of varying cyclical loading as the arm moves throughout its workspace could be observed in a practical environment.

The simultaneous control of antagonistic SMA actuators, as enabled by the compliant joint, could be expanded in many ways. Speed could be improved using a temperature model and dynamic control of the maximum current, rather than a single safe current. Additionally, further experiments using different, or time-varying, minimum deflection angles, could further improve torque tracking control.

Several avenues for high-level SMA-actuated arm control are also identified. The joint space impedance controller could be extended to a task-space impedance or admittance controller, further improving the arm's ability to interact with its environment. Additionally, the increased range and payload make it capable of experimental validation of drone-arm control systems tailored to the unique dynamics of SMA actuators.

The arm's high payload-to-mass ratio makes it an excellent candidate for future aerial manipulation tasks. Its increased range and payload when compared to existing SMA-actuated robotic arms make it the first capable of using gripper manipulators, simple tools, or sensor payloads. By reducing the mass of the manipulator while maintaining a large payload, larger and more complex end-effectors can be used without sacrificing flight time or requiring a larger drone frame.

This improved performance makes the developed arms suitable for construction and inspection tasks that are being explored for motor-driven aerial manipulators. The arm's low mass would result in improved performance when used as an aerial

manipulator, decreasing power consumption and required drone size. This is key to expanding aerial manipulation to confined spaces, indoors, or near workers where safety must be emphasized.

References

[1] J. M. Jani, M. Leary, A. Subic, and M. A. Gibson, "A review of shape memory alloy research, applications and opportunities," *Materials & Design (1980-2015)*, vol. 56, pp. 1078–1113, 2014.

[2] H. Bonyan Khamseh, F. Janabi-Sharifi, and A. Abdessameud, "Aerial manipulation—a literature survey," *Robotics and Autonomous Systems*, vol. 107, pp. 221–235, 2018.

[3] H. Klippstein, H. Hassanin, A. Sanchez, Y. Zweiri, and L. Seneviratne, "Additive manufacturing of porous structures for unmanned aerial vehicles applications," *Advanced Engineering Materials*, vol. 20, no. 9, May 2018.

[4] A. Alakhras, I. Sattar, M. Alvi, M. Qanbar, M. Jaradat, and M. Alkaddour, "The design of a lightweight cable aerial manipulator with a CoG compensation mechanism for construction inspection purposes," *Applied Sciences*, vol. 12, no. 3, pp. 1173–1190, Jan. 2022.

[5] A. Suarez, A. E. Jimenez-Cano, V. M. Vega, G. Heredia, A. Rodriguez-Castaño, and A. Ollero, "Lightweight and human-size dual arm aerial manipulator," in *2017 International Conference on Unmanned Aircraft Systems (ICUAS)*, 2017, pp. 1778–1784.

[6] H. Ashrafiuon, M. Eshraghi, and M. H. Elahinia, "Position control of a three-link shape memory alloy actuated robot," *Journal of intelligent material systems and structures*, vol. 17, no. 5, pp. 381–392, 2006.

[7] A. Golgouneh, B. Holschuh, and L. Dunne, "A controllable biomimetic SMA-actuated robotic arm," in *2020 8th IEEE RAS/EMBS International Conference for Biomedical Robotics and Biomechatronics (BioRob)*, 2020, pp. 152–157.

[8] Y. Sun, Y. Liu, F. Pancheri, and T. C. Lueth, "LARG: A Lightweight Robotic Gripper With 3-D Topology Optimized Adaptive Fingers," *IEEE/ASME Transactions on Mechatronics*, vol. 27, no. 4, pp. 2026–2034, 2022.

[9] Y. Li, M. Congr, D. Liu, and Y. Du, "Design and analysis of a novel lightweight, versatile soft-rigid robot," in *2021 IEEE International Conference on Robotics and Automation (ICRA)*, 2021, pp. 11 871–11 877.

[10] M. J. Mosley and C. Mavroidis, "Design and control of a shape memory alloy wire bundle actuator," in *International Design Engineering Technical Conferences and Computers and Information in Engineering Conference*, American Society of Mechanical Engineers, 2000, pp. 973–979.

[11] T. Luong, C. Park, M. Doh, Y. Ha, and H. Moon, "Impedance control of antagonistically driven sma springs," in *2022 19th International Conference on Ubiquitous Robots (UR)*, 2022, pp. 307–312.

[12] A. A. Araujo, E. A. Tannuri, and A. Forner-Cordero, "Simulation of model-based impedance control applied to a biomechatronic exoskeleton with shape memory alloy actuators," in *2012 4th IEEE RAS & EMBS International Conference on Biomedical Robotics and Biomechatronics (BioRob)*, IEEE, 2012, pp. 1567–1572.

[13] L. Manfredi, F. Velsink, H. Khan, and A. Cuschieri, "A variable impedance actuator based on shape memory alloy," *MESSE BREMEN WFB Wirtschaftsförderung Bremen GmbH: Bremen, Germany*, pp. 167–170, 2016.

[14] M. Elahinia, J. Koo, M. Ahmadian, and C. Woolsey, "Backstepping control of a shape memory alloy actuated robotic arm," *Journal of Vibration and Control*, vol. 11, no. 3, pp. 407–429, 2005.

[15] Y. H. Teh and R. Featherstone, "An architecture for fast and accurate control of shape memory alloy actuators," *The International Journal of Robotics Research*, vol. 27, no. 5, pp. 595–611, 2008.

[16] M. H. Elahinia, H. Ashrafiuon, M. Ahmadian, and W. T. Baumann, "Design of extended kalman filter for a shape memory alloy manipulator," in *International Design Engineering Technical Conferences and Computers and Information in Engineering Conference*, vol. 5, Sep. 2003, pp. 1663–1670.

[17] M. Elahinia, M. Ahmadian, and H. Ashrafiuon, "Design of a kalman filter for rotary shape memory alloy actuators," *Smart Materials and Structures*, vol. 13, p. 691, May 2004.

[18] S. Mohan and A. Banerjee, "Self-sensing shape memory alloy wire actuator based on modified boyd and lagoudas model," in *65th Congress of Indian Society of Theoretical and Applied Mechanics*, 2020.

[19] A. Mohtat and A. Yousefi-Koma, "Online estimation and identification of shape memory alloy-actuated flexible structures through unscented kalman filtering," *Journal of Intelligent Material Systems and Structures*, vol. 21, no. 16, pp. 1589–1602, 2010.

[20] F. G. Costa, J. Ueyama, T. Braun, G. Pessin, F. S. Osório, and P. A. Vargas, "The use of unmanned aerial vehicles and wireless sensor network in agricultural applications," in *2012 IEEE International Geoscience and Remote Sensing Symposium*, 2012, pp. 5045–5048.

[21] H. Li, B. Wang, L. Liu, G. Tian, T. Zheng, and J. Zhang, "The design and application of smartcopter: An unmanned helicopter based robot for transmission line inspection," in *2013 Chinese Automation Congress*, IEEE, 2013, pp. 697–702.

[22] S. Siebert and J. Teizer, "Mobile 3d mapping for surveying earthwork projects using an unmanned aerial vehicle (uav) system," *Automation in Construction*, vol. 41, pp. 1–14, 2014.

[23] P. Chermprayong, K. Zhang, F. Xiao, and M. Kovac, "An integrated delta manipulator for aerial repair: A new aerial robotic system," *IEEE Robotics Automation Magazine*, vol. 26, no. 1, pp. 54–66, 2019.

[24] M. Orsag, C. Korpela, S. Bogdan, and P. Oh, "Valve turning using a dual-arm aerial manipulator," in *2014 International Conference on Unmanned Aircraft Systems (ICUAS)*, IEEE, 2014, pp. 836–841.

[25] S. Quintanar-Guzmán, "Nonlinear observation and control of a lightweight robotic manipulator actuated by shape memory alloy (SMA) wires," Ph.D. dissertation, University of Luxembourg, Luxembourg, 2019.

[26] A. Cormier, M. C. Bazzocchi, and M. Martinez, "A shape memory alloy actuated robotic arm for aerial manipulation," *Journal of Intelligent Material Systems and Structures*, vol. 36, no. 20, pp. 1325–1341, 2025.

[27] A. Cormier and M. C. Bazzocchi, "Multi-level impedance control of a shape memory alloy actuated robotic arm," under review, submitted December 2025.

[28] C. Liang and C. Rogers, "Design of shape memory alloy actuators," 1992.

[29] Dynalloy Inc. "Technical Characteristics of FLEXINOL Actuator Wires," Accessed: Feb. 6, 2024.

[30] C. Liang and C. Rogers, "One-dimensional thermomechanical constitutive relations for shape memory materials," *Journal of Intelligent Material Systems and Structures*, vol. 1, no. 2, pp. 207–234, 1990.

[31] L. Brinson, "One-dimensional constitutive behavior of shape memory alloys: Thermomechanical derivation with non-constant material functions and redefined martensite internal variable," *Journal of Intelligent Material Systems and Structures*, vol. 4, no. 2, pp. 229–242, 1993.

[32] J. G. Boyd and D. C. Lagoudas, "A thermodynamical constitutive model for shape memory materials. Part I. The monolithic shape memory alloy," *International Journal of Plasticity*, vol. 12, no. 6, pp. 805–842, 1996.

[33] L. C. Brinson and M. S. Huang, "Simplifications and comparisons of shape memory alloy constitutive models," *Journal of Intelligent Material Systems and Structures*, vol. 7, no. 1, pp. 108–114, 1996.

[34] H. Rodrigue, W. Wang, M.-W. Han, T. J. Kim, and S.-H. Ahn, "An overview of shape memory alloy-coupled actuators and robots," *Soft Robotics*, vol. 4, no. 1, pp. 3–15, 2017.

[35] H. Yang, M. Xu, W. Li, and S. Zhang, "Design and implementation of a soft robotic arm driven by SMA coils," *IEEE Transactions on Industrial Electronics*, vol. 66, no. 8, pp. 6108–6116, 2018.

[36] J.-H. Lee, Y. S. Chung, and H. Rodrigue, "Long shape memory alloy tendon-based soft robotic actuators and implementation as a soft gripper," *Scientific reports*, vol. 9, no. 1, p. 11 251, 2019.

[37] R. Featherstone and Y. H. Teh, "Improving the speed of shape memory alloy actuators by faster electrical heating," in *Experimental Robotics IX*, M. H. Ang and O. Khatib, Eds., Berlin, Heidelberg: Springer Berlin Heidelberg, 2006, pp. 67–76.

[38] H. Rodrigue, W. Wang, M.-W. Han, T. J. Kim, and S.-H. Ahn, "An overview of shape memory alloy-coupled actuators and robots," *Soft Robotics*, vol. 4, no. 1, pp. 3–15, 2017.

[39] S. S. Cheng, Y. Kim, and J. P. Desai, "New actuation mechanism for actively cooled sma springs in a neurosurgical robot," *IEEE Transactions on Robotics*, vol. 33, no. 4, pp. 986–993, 2017.

[40] J.-H. Guan, Y.-C. Pei, and J.-T. Wu, "A driving strategy of shape memory alloy wires with electric resistance modeled by logistic function for power consumption reduction," *Mechanical Systems and Signal Processing*, vol. 160, p. 107 839, 2021.

[41] S. Furst, J. Crews, and S. Seelecke, "Stress, strain, and resistance behavior of two opposing shape memory alloy actuator wires for resistance-based self-sensing applications," *Journal of Intelligent Material Systems and Structures*, vol. 24, pp. 1951–1968, Nov. 2013.

[42] J. Prechtl, S. Seelecke, P. Motzki, and G. Rizzello, "Self-sensing control of antagonistic sma actuators based on resistance-displacement hysteresis compensation," in *ASME 2020 Conference on Smart Materials, Adaptive Structures and Intelligent Systems*, ser. Smart Materials, Adaptive Structures and Intelligent Systems, Sep. 2020, V001T03A001.

[43] M. Elahinia and M. Ahmadian, "An enhanced sma phenomenological model: Ii. the experimental study," *Smart Materials and Structures*, vol. 14, pp. 1309–1319, 2005.

[44] S. Quintanar-Guzmán, S. Kannan, A. Aguilera-González, M. A. Olivares-Mendez, and H. Voos, "Operational space control of a lightweight robotic arm actuated by shape memory alloy wires: A comparative study," *Journal of Intelligent Material Systems and Structures*, vol. 30, no. 9, pp. 1368–1384, 2019.

[45] N. T. Tai, N. B. Kha, and K. K. Ahn, "Model predictive control for shape memory alloy cylinder," in *2009 ICCAS-SICE*, 2009, pp. 3766–3770.

[46] N. Nikdel, P. Nikdel, M. A. Badamchizadeh, and I. Hassanzadeh, "Using neural network model predictive control for controlling shape memory alloy-based manipulator," *IEEE Transactions on Industrial Electronics*, vol. 61, no. 3, pp. 1394–1401, 2014.

[47] A. Srivastava, C. Ward, and R. V. Patel, "Adaptive neural preisach model and model predictive control of shape memory alloy actuators," in *2017 IEEE International Conference on Advanced Intelligent Mechatronics (AIM)*, 2017, pp. 1179–1184.

[48] F. O. Maria Joseph and T. Podder, "Sliding mode control of a shape memory alloy actuated active flexible needle," *Robotica*, vol. 36, no. 8, pp. 1188–1205, 2018.

[49] H. Zhou and N. Ma, "Modeling and experimental implementation of a flexible sma wire-based gripper for confined space operation," *Journal of Intelligent Material Systems and Structures*, vol. 33, no. 17, pp. 2161–2175, 2022.

[50] S. Dilibal and E. D. Engeberg, "Finger-like manipulator driven by antagonistic nickel-titanium shape memory alloy actuators," in *2015 International Conference on Advanced Robotics (ICAR)*, IEEE, 2015, pp. 152–157.

[51] K. Andrianesis and A. Tzes, "Development and control of a multifunctional prosthetic hand with shape memory alloy actuators," *Journal of Intelligent Robotic Systems*, vol. 78, pp. 257–289, 2015.

[52] S. Matsubara, S. Okamoto, and J. H. Lee, "Prosthetic hand using shape memory alloy type artificial muscle," in *Proceedings of the International MultiConference of Engineers and Computer Scientists (IMECS 2012)*, March 14–16, 2012, vol. II, Hong Kong, Mar. 2012.

[53] V. Farias, L. Solis, L. Melendez, C. Garcia, and R. Velazquez, "A four-fingered robot hand with shape memory alloys," in *AFRICON 2009*, 2009, pp. 1–6.

[54] F. Simone, A. York, and S. Seelecke, "Design and fabrication of a three-finger prosthetic hand using SMA muscle wires," in *Bioinspiration, Biomimetics, and Bioreplication 2015*, SPIE, vol. 9429, San Diego, California, United States, Mar. 2015, p. 94290T.

[55] C. Pfeiffer, K. DeLaurentis, and C. Mavroidis, "Shape memory alloy actuated robot prostheses: Initial experiments," in *Proceedings 1999 IEEE International Conference on Robotics and Automation*, vol. 3, 1999, pp. 2385–2391.

[56] J. Jeong et al., "Soft wearable robot with shape memory alloy (sma)-based artificial muscle for assisting with elbow flexion and forearm supination/pronation," *IEEE Robotics and Automation Letters*, vol. 7, no. 3, pp. 6028–6035, 2022.

[57] J. Jeong et al., "Wrist assisting soft wearable robot with stretchable coolant vessel integrated sma muscle," *IEEE/ASME Transactions on Mechatronics*, vol. 27, no. 2, pp. 1046–1058, 2022.

[58] A. Golgouneh et al., "Design of a hybrid sma-pneumatic based wearable upper limb exoskeleton," in *Proceedings of the 2021 ACM International Symposium on Wearable Computers*, ser. ISWC '21, Virtual, USA, 2021, pp. 179–183.

[59] H. Talebi, H. Golestanian, M. Zakerzadeh, and H. Homaei, "Thermoelectric heat transfer modeling of shape memory alloy actuators," in *The 22nd Annual International Conference on Mechanical Engineering*, Apr. 2014.

[60] I. Hassanzadeh, N. Nikdel, Nazila, N. Talebi, and M. A. Badamchizadeh, "Design of augmented ekf for shape memory alloy actuated manipulator," *International Journal of Engineering Science and Technology*, vol. 2, Jul. 2010.

[61] F. Lazzari, D. Magrin, M. Prandini, J. Romanò, L. Garavaglia, and S. Pittaccio, "Modeling and state estimation for the advanced control of a multimaterial shape memory based actuator," M.S. thesis, Politecnico di Milano, 2021.

[62] H. Gurung and A. Banerjee, "Development of an extended kalman filter for the self-sensing application of a spring-biased shape memory alloy wire actuator," *Smart Materials and Structures*, vol. 25, p. 025 012, Feb. 2016.

[63] N. T. Tai and K. K. Ahn, "Output feedback direct adaptive controller for a sma actuator with a kalman filter," *IEEE Transactions on Control Systems Technology*, vol. 20, no. 4, pp. 1081–1091, 2012.

[64] Z. Sun, Y. Li, B. Zi, and B. Chen, "Development and dynamic state estimation for robotic knee–ankle orthosis with shape memory alloy actuators," *Journal of Mechanical Design*, vol. 146, no. 1, p. 013 302, 2024. DOI: 10.1115/1.4063565.

[65] D. Zhang, X. Zhao, J. Han, X. Li, and B. Zhang, "Active modeling and control for shape memory alloy actuators," *IEEE Access*, vol. 7, pp. 162 549–162 558, 2019.

[66] J. Lee, M. Jin, and K. K. Ahn, "Precise tracking control of shape memory alloy actuator systems using hyperbolic tangential sliding mode control with time delay estimation," *Mechatronics*, vol. 23, pp. 310–317, Apr. 2013.

[67] K. M. Lynch and F. C. Park, *Modern Robotics: Mechanics, Planning, and Control*. Cambridge University Press, 2017, pp. 1–544.

[68] L. Roveda, D. Riva, G. Bucca, and D. Piga, "External joint torques estimation for a position-controlled manipulator employing an extended kalman filter," in *2021 18th International Conference on Ubiquitous Robots (UR)*, 2021, pp. 101–107.

[69] L. Roveda and D. Piga, "Sensorless environment stiffness and interaction force estimation for impedance control tuning in robotized interaction tasks," *Autonomous Robots*, vol. 45, pp. 1–18, Mar. 2021.

[70] A. Wahrburg, J. Bös, K. D. Listmann, F. Dai, B. Matthias, and H. Ding, "Motor-current-based estimation of cartesian contact forces and torques for robotic manipulators and its application to force control," *IEEE Transactions on Automation Science and Engineering*, vol. 15, no. 2, pp. 879–886, 2018.

[71] T. Murakami, F. Yu, and K. Ohnishi, "Torque sensorless control in multidegree-of-freedom manipulator," *IEEE Transactions on Industrial Electronics*, vol. 40, no. 2, pp. 259–265, 1993.

[72] K. D. Kallu, W. Jie, and M. C. Lee, "Sensorless reaction force estimation of the end effector of a dual-arm robot manipulator using sliding mode control with a sliding perturbation observer," *International Journal of Control, Automation and Systems*, vol. 16, May 2018.

[73] H. Mohammadi, G. Khademi, D. Simon, A. van den Bogert, and H. Richter, "Upper body estimation of muscle forces, muscle states, and joint motion using an extended kalman filter," *IET Control Theory Applications*, vol. 14, Jan. 2021.

[74] S. Quintanar-Guzmán, S. Kannan, M. A. Olivares-Mendez, and H. Voos, "Lightweight robotic arm actuated by shape memory alloy (SMA) wires," in *2016 8th International Conference on Electronics, Computers and Artificial Intelligence (ECAI)*, 2016, pp. 1–6.

[75] H. Su et al., "Pneumatic soft robots: Challenges and benefits," *Actuators*, vol. 11, no. 3, 2022.

[76] F. Daerden, D. Lefeber, B. Verrelst, and R. Van Ham, "Pleated pneumatic artificial muscles: Actuators for automation and robotics," in *2001 IEEE/ASME International Conference on Advanced Intelligent Mechatronics.*, vol. 2, 2001, pp. 738–743.

[77] F. Carpi, R. Kornbluh, P. Sommer-Larsen, and G. Alici, "Electroactive polymer actuators as artificial muscles: Are they ready for bioinspired applications?" *Bioinspiration Biomimetics*, vol. 6, no. 4, p. 045 006, Nov. 2011.

[78] K. J. Kim and S. Tadokoro, *Electroactive Polymers for Robotic Applications: Artificial Muscles and Sensors*. Springer London, 2007.

[79] Dassault Systems. "Abaqus/CAE," Accessed: Feb. 6, 2024.

[80] Z. Moumni, Y. Zhang, J. Wang, and X. Gu, "A global approach for the fatigue of shape memory alloys," *Shape Memory and Superelasticity*, vol. 4, pp. 385–401, Oct. 2018.

[81] G. Eggeler, E. Hornbogen, A. Yawny, A. Heckmann, and M. Wagner, "Structural and functional fatigue of niti shape memory alloys," *Materials Science and Engineering: A*, vol. 378, no. 1, pp. 24–33, 2004.

[82] P. Yao, K. Zhou, Y. Lin, and P. Tang, "Light-weight topological optimization for upper arm of an industrial welding robot," *Metals*, vol. 9, no. 9, pp. 1020–1048, Sep. 2019.

[83] Bambu Labs. "Bambu Filament Technical Data Sheet V3.0," Accessed: Feb. 6, 2024.

[84] J. Aboudi, S. M. Arnold, and B. A. Bednarcyk, *Practical micromechanics of composite materials*. Butterworth-Heinemann, 2021.

[85] P. Cignoni, M. Callieri, M. Corsini, M. Dellepiane, F. Ganovelli, and G. Ranzuglia, "MeshLab: an Open-Source Mesh Processing Tool," in *Eurographics Italian Chapter Conference*, 2008.

[86] M. Desbrun, M. Meyer, P. Schröder, and A. H. Barr, *Implicit fairing of irregular meshes using diffusion and curvature flow*, New York, NY, USA, Jan. 1999.

[87] G. Taubin, "A signal processing approach to fair surface design," in *Proceedings of the 22nd annual conference on Computer graphics and interactive techniques*, New York, NY, USA: Association for Computing Machinery, 1995, pp. 351–358.

[88] Dassault Systems. "3DEXPERIENCE SOLIDWORKS Offers," Accessed: Feb. 6, 2024.

[89] C. D. Bellicoso, L. R. Buonocore, V. Lippiello, and B. Siciliano, "Design, modeling and control of a 5-dof light-weight robot arm for aerial manipulation," in *2015 23rd Mediterranean Conference on Control and Automation (MED)*, IEEE, Torremolinos, Spain, 16-19 June 2015, pp. 853–858.

[90] A. Pathak, "The development of an antagonistic SMA actuation technology for the active cancellation of human tremor," Ph.D. dissertation, University of Michigan, USA, 2010, p. 265.

[91] Q. Lindsey, D. Mellinger, and V. Kumar, "Construction with quadrotor teams," *Autonomous Robots*, vol. 33, pp. 323–336, 2012.

[92] C. Ding, L. Lu, C. Wang, and C. Ding, "Design, sensing, and control of a novel uav platform for aerial drilling and screwing," *IEEE Robotics and Automation Letters*, pp. 3176–3183, Feb. 2021.

[93] C. Liang and C. A. Rogers, "One-dimensional thermomechanical constitutive relations for shape memory materials," *Journal of Intelligent Material Systems and Structures*, vol. 8, no. 4, pp. 285–302, 1997.

[94] D. Simon, "The discrete-time extended kalman filter," in *Optimal State Estimation: Kalman, HInfinity, and Nonlinear Approaches*, Hoboken, NJ: John Wiley & Sons, 2006, ch. 13.2.3, 14, 15, pp. 407–410.

Appendix A: Arm Dynamics Matrix Definitions

This appendix defines the robot arm inertia matrix $\mathbf{M}$ and the Coriolis/centrifugal matrix $\mathbf{C}$. Each element of the two matrices (e.g., M_{11} are defined separately below.

$$\mathbf{M} = \begin{bmatrix} M_{11} & M_{12} & M_{13} \\ M_{21} & M_{22} & M_{23} \\ M_{31} & M_{32} & M_{33} \end{bmatrix} \tag{1}$$

$$\begin{aligned}
M_{11} &= L_1^2 M_1 + L_1^2 M_2 + L_1^2 M_3 + L_2^2 M_2 + L_2^2 M_3 + L_3^2 M_3 \\
&\quad + 2L_1 L_2 M_2 \cos(q_2) + 2L_1 L_2 M_3 \cos(q_2) + 2L_2 L_3 M_3 \cos(q_3) \\
&\quad + 2L_1 L_3 M_3 \cos(q_2 + q_3)
\end{aligned}$$

$$\begin{aligned}
M_{12} &= L_2^2 M_2 + L_2^2 M_3 + L_3^2 M_3 + L_1 L_2 M_2 \cos(q_2) + L_1 L_2 M_3 \cos(q_2) \\
&\quad + 2L_2 L_3 M_3 \cos(q_3) + L_1 L_3 M_3 \cos(q_2 + q_3)
\end{aligned}$$

$$M_{13} = L_3 M_3 (L_3 + L_1 \cos(q_2 + q_3) + L_2 \cos(q_3))$$

$$\begin{aligned}
M_{21} &= L_2^2 M_2 + L_2^2 M_3 + L_3^2 M_3 + L_1 L_2 M_2 \cos(q_2) + L_1 L_2 M_3 \cos(q_2) \\
&\quad + 2L_2 L_3 M_3 \cos(q_3) + L_1 L_3 M_3 \cos(q_2 + q_3)
\end{aligned}$$

$$M_{22} = L_2^2 M_2 + L_2^2 M_3 + L_3^2 M_3 + 2L_2 L_3 M_3 \cos(q_3)$$

$$M_{23} = L_3 M_3 (L_3 + L_2 \cos(q_3))$$

$$M_{31} = L_3 M_3 (L_3 + L_1 \cos(q_2 + q_3) + L_2 \cos(q_3))$$

$$M_{32} = L_3 M_3 (L_3 + L_2 \cos(q_3))$$

$$M_{33} = L_3^2 M_3$$

$$\mathbf{C} = \begin{bmatrix} C_{11} & C_{12} & C_{13} \\ C_{21} & C_{22} & C_{23} \\ C_{31} & C_{32} & C_{33} \end{bmatrix} \tag{2}$$

$$\begin{aligned}
C_{11} &= -q_{3d}\big(L_1 L_3 M_3 \sin(q_2 + q_3) + L_2 L_3 M_3 \sin(q_3)\big) \\
&\quad - q_{2d}\big(L_1 L_3 M_3 \sin(q_2 + q_3) + L_1 L_2 M_2 \sin(q_2) + L_1 L_2 M_3 \sin(q_2)\big) \\
C_{12} &= -L_1 q_{1d}\big(L_3 M_3 \sin(q_2 + q_3) + L_2 M_2 \sin(q_2) + L_2 M_3 \sin(q_2)\big) \\
&\quad - L_1 q_{2d}\big(L_3 M_3 \sin(q_2 + q_3) + L_2 M_2 \sin(q_2) + L_2 M_3 \sin(q_2)\big) \\
&\quad - L_3 M_3 q_{3d}\big(L_1 \sin(q_2 + q_3) + L_2 \sin(q_3)\big) \\
C_{13} &= -L_3 M_3 (L_1 \sin(q_2 + q_3) + L_2 \sin(q_3))(q_{1d} + q_{2d} + q_{3d}) \\
C_{21} &= q_{1d}\big(L_1 L_3 M_3 \sin(q_2 + q_3) + L_1 L_2 M_2 \sin(q_2) + L_1 L_2 M_3 \sin(q_2)\big) \\
&\quad - L_2 L_3 M_3 q_{3d} \sin(q_3) \\
C_{22} &= -L_2 L_3 M_3 q_{3d} \sin(q_3) \\
C_{23} &= -L_2 L_3 M_3 \sin(q_3)(q_{1d} + q_{2d} + q_{3d}) \\
C_{31} &= q_{1d}\big(L_1 L_3 M_3 \sin(q_2 + q_3) + L_2 L_3 M_3 \sin(q_3)\big) + L_2 L_3 M_3 q_{2d} \sin(q_3) \\
C_{32} &= L_2 L_3 M_3 \sin(q_3)(q_{1d} + q_{2d}) \\
C_{33} &= 0
\end{aligned}$$

Appendix B: EKF Jacobian Definition

This appendix defines the symbolic forms of the EKF transformation Jacobian for forward transformation, J_f, backwards transformation, J_b, and no transformation, J_n. Each nonzero term of the Jacobian is defined separately.

$$J_f = \begin{bmatrix} J_{f1,1} & J_{f1,2} & 0 & 0 \\ 0 & J_{f2,2} & 0 & 0 \\ J_{f3,1} & J_{f3,2} & 0 & 0 \\ J_{f4,1} & J_{f4,2} & 0 & 0 \end{bmatrix}$$

$$J_{f1,1} = -\frac{\Omega {a_A}^2 \xi_M \cos\left(\frac{a_A\left(\sigma + A_s c_A - T c_A\right)}{c_A}\right) N}{D^2}$$

$$\begin{aligned} N = {} & 180 L_w V^2 c_A - 180 L_w \Theta V^2 + 180 A_w L_w R T \Theta h_0 - 180 A_w L_w R \Theta T_{\text{amb}} h_0 \\ & - 180 A_w L_w R T c_A h_0 + 180 A_w L_w R T_{\text{amb}} c_A h_0 + 180 A_w L_w R T^3 \Theta h_2 \\ & + 180 S E L_w V^2 c_A \epsilon_{\max} - 180 A_w L_w R T^3 c_A h_2 - 180 A_w L_w R T^2 \Theta T_{\text{amb}} h_2 \\ & + 180 A_w L_w R T^2 T_{\text{amb}} c_A h_2 + \pi E R c_p \dot{\theta}_C m_w r - 180 A_w S E L_w R T c_A \epsilon_{\max} h_0 \\ & + 180 A_w S E L_w R T_{\text{amb}} c_A \epsilon_{\max} h_0 - 180 A_w S E L_w R T^3 c_A \epsilon_{\max} h_2 \\ & + 180 A_w S E L_w R T^2 T_{\text{amb}} c_A \epsilon_{\max} h_2) \end{aligned}$$

$$D = 90 L_w R c_p m_w \left(2 c_A + \Omega a_A \xi_M \sin\left(\frac{a_A\left(\sigma + A_s c_A - T c_A\right)}{c_A}\right) + 2 S E c_A \epsilon_{\max}\right)$$

$$J_{f3,1} = -\frac{{a_A}^2 \xi_M \cos\left(\frac{a_A\left(\sigma + A_s c_A - T c_A\right)}{c_A}\right)\left(SE\epsilon_{\max} + 1\right) N}{D^2}$$

$$\begin{aligned}
N = {} & 180 L_w V^2 c_A \\
& - 180 L_w \Theta V^2 \\
& + 180 A_w L_w R T \Theta h_0 \\
& - 180 A_w L_w R \Theta T_{\text{amb}} h_0 \\
& - 180 A_w L_w R T c_A h_0 \\
& + 180 A_w L_w R T_{\text{amb}} c_A h_0 \\
& + 180 A_w L_w R T^3 \Theta h_2 \\
& + 180 S E L_w V^2 c_A \epsilon_{\max} \\
& - 180 A_w L_w R T^3 c_A h_2 \\
& - 180 A_w L_w R T^2 \Theta T_{\text{amb}} h_2 \\
& + 180 A_w L_w R T^2 T_{\text{amb}} c_A h_2 \\
& + \pi E R c_p \dot{\theta_C} m_w r \\
& - 180 A_w S E L_w R T c_A \epsilon_{\max} h_0 \\
& + 180 A_w S E L_w R T_{\text{amb}} c_A \epsilon_{\max} h_0 \\
& - 180 A_w S E L_w R T^3 c_A \epsilon_{\max} h_2 \\
& + 180 A_w S E L_w R T^2 T_{\text{amb}} c_A \epsilon_{\max} h_2)
\end{aligned}$$

$$D = 90 L_w R c_p m_w \left(2 c_A + \Omega a_A \xi_M \sin\left(\frac{a_A\left(\sigma + A_s c_A - T c_A\right)}{c_A}\right) + 2 S E c_A \epsilon_{\max}\right)$$

$$J_{f4,1} = \frac{2S\Omega {a_A}^2 \epsilon_{\max} \xi_M \cos\left(\frac{a_A\left(\sigma + A_s c_A - T c_A\right)}{c_A}\right) N}{D^2}$$

$$\begin{aligned} N = {} & L_w V^2 c_A - 180 L_w \Theta V^2 \\ & + 180 A_w L_w R T \Theta h_0 \\ & - 180 A_w L_w R \Theta T_{\text{amb}} h_0 \\ & - 180 A_w L_w R T c_A h_0 \\ & + 180 A_w L_w R T_{\text{amb}} c_A h_0 \\ & + 180 A_w L_w R T^3 \Theta h_2 \\ & + 180 S E L_w V^2 c_A \epsilon_{\max} \\ & - 180 A_w L_w R T^3 c_A h_2 \\ & - 180 A_w L_w R T^2 \Theta T_{\text{amb}} h_2 \\ & + 180 A_w L_w R T^2 T_{\text{amb}} c_A h_2 \\ & + \pi E R c_p \dot{\theta_C} m_w r \\ & - 180 A_w S E L_w R T c_A \epsilon_{\max} h_0 \\ & + 180 A_w S E L_w R T_{\text{amb}} c_A \epsilon_{\max} h_0 \\ & - 180 A_w S E L_w R T^3 c_A \epsilon_{\max} h_2 \\ & + 180 A_w S E L_w R T^2 T_{\text{amb}} c_A \epsilon_{\max} h_2) \end{aligned}$$

$$D = R c_p m_w r \pi \left(2 c_A + \Omega a_A \xi_M \sin\left(\frac{a_A\left(\sigma + A_s c_A - T c_A\right)}{c_A}\right) + 2 S E c_A \epsilon_{\max}\right)$$

$$J_{f1,2} = \frac{N c_A}{D^2}$$

$$\begin{aligned} N =& A_w L_w R \Omega \xi_M \\ & (a_A h_0 + a_A c_A h_0 + T^2 a_A h_2 + T^2 a_A c_A h_2 - 2 T T_{\text{amb}} a_A h_2 - 2 T T_{\text{amb}} a_A c_A h_2) \\ & \sin\left(\frac{a_A(\sigma + A_s c_A - T c_A)}{c_A}\right) \\ & + \left(A_w L_w R \Omega \xi_M^2 \left(\frac{1}{2} a_A^2 h_0 + \frac{3}{2} T^2 a_A^2 h_2 - T T_{\text{amb}} a_A^2 h_2\right)\right) \\ & \sin^2\left(\frac{a_A(\sigma + A_s c_A - T c_A)}{c_A}\right) \\ & + (A_w L_w R \Omega \xi_M + A_w S E L_w R \epsilon_{\max} + L_w \Omega V^2 + \pi E \Omega R c_p m_w r) \\ & \cos\left(\frac{a_A(\sigma + A_s c_A - T c_A)}{c_A}\right) \end{aligned}$$

$$D = 90 L_w R c_p m_w \left(2 c_A + \Omega a_A \xi_M \sin\left(\frac{a_A\,(\sigma + A_s c_A - T c_A)}{c_A}\right) + 2 S E c_A \epsilon_{\max}\right)$$

$$J_{f2,2} = \frac{A_w\ \left(3\,h_2\,T^2 - 2\,T_{\text{amb}}\,h_2\,T + h_0\right)}{c_p\,m_w}$$

$$J_{f3,2} = \frac{a_A \xi_M}{90\, L_w\, R\, c_p\, m_w D^2} \left(\mathcal{C} \cos \mathcal{T} + \mathcal{S} \sin \mathcal{T} + \mathcal{Q} \sin^2 \mathcal{T} \right)$$

$$\mathcal{T} = \frac{a_A \left(\sigma + A_s c_A - T c_A \right)}{c_A}$$

$$D = 2c_A + \Omega a_A \xi_M \sin \mathcal{T} + 2SEc_A \epsilon_{\max}$$

$$\begin{aligned}
\mathcal{C} &= 180 L_w V^2 a_A c_A^2 - 180 L_w \Theta V^2 a_A c_A \\
&\quad + 360 SEL_w V^2 a_A c_A^2 \epsilon_{\max} + 180 C^2 E^2 L_w V^2 a_A c_A^2 \epsilon_{\max}^2 \\
&\quad - 180 A_w L_w R T a_A c_A^2 h_0 + 180 A_w L_w R T_{\text{amb}} a_A c_A^2 h_0 \\
&\quad - 180 A_w L_w R T^3 a_A c_A^2 h_2 + 180 A_w L_w R T^2 T_{\text{amb}} a_A c_A^2 h_2 \\
&\quad + 180 A_w L_w R T \Theta a_A c_A h_0 - 180 A_w L_w R \Theta T_{\text{amb}} a_A c_A h_0 \\
&\quad + 180 A_w L_w R T^3 \Theta a_A c_A h_2 - 180 A_w L_w R T^2 \Theta T_{\text{amb}} a_A c_A h_2 \\
&\quad - 360 A_w SEL_w R T a_A c_A^2 \epsilon_{\max} h_0 + 360 A_w SEL_w R T_{\text{amb}} a_A c_A^2 \epsilon_{\max} h_0 \\
&\quad - 360 A_w SEL_w R T^3 a_A c_A^2 \epsilon_{\max} h_2 + 360 A_w SEL_w R T^2 T_{\text{amb}} a_A c_A^2 \epsilon_{\max} h_2 \\
&\quad - 180 A_w C^2 E^2 L_w R T a_A c_A^2 \epsilon_{\max}^2 h_0 + 180 A_w C^2 E^2 L_w R T_{\text{amb}} a_A c_A^2 \epsilon_{\max}^2 h_0 \\
&\quad - 180 A_w C^2 E^2 L_w R T^3 a_A c_A^2 \epsilon_{\max}^2 h_2 + 180 A_w C^2 E^2 L_w R T^2 T_{\text{amb}} a_A c_A^2 \epsilon_{\max}^2 h_2 \\
&\quad + \pi E R a_A c_A c_p m_w r\, \dot{\theta_C} + \pi S E^2 R a_A c_A c_p m_w r\, \epsilon_{\max}
\end{aligned}$$

$$\begin{aligned}
\mathcal{S} &= 180 A_w L_w R c_A^2 h_0 - 180 A_w L_w R \Theta c_A h_0 \\
&\quad + 540 A_w L_w R T^2 c_A^2 h_2 - 540 A_w L_w R T^2 \Theta c_A h_2 \\
&\quad - 360 A_w L_w R T T_{\text{amb}} c_A^2 h_2 + 360 A_w L_w R T \Theta T_{\text{amb}} c_A h_2 \\
&\quad + 360 A_w SEL_w R c_A^2 \epsilon_{\max} h_0 - 180 A_w SEL_w R \Theta c_A \epsilon_{\max} h_0 \\
&\quad + 1080 A_w SEL_w R T^2 c_A^2 \epsilon_{\max} h_2 - 540 A_w SEL_w R T^2 \Theta c_A \epsilon_{\max} h_2 \\
&\quad - 720 A_w SEL_w R T T_{\text{amb}} c_A^2 \epsilon_{\max} h_2 + 360 A_w SEL_w R T \Theta T_{\text{amb}} c_A \epsilon_{\max} h_2 \\
&\quad + 180 A_w C^2 E^2 L_w R c_A^2 \epsilon_{\max}^2 h_0 + 540 A_w C^2 E^2 L_w R T^2 c_A^2 \epsilon_{\max}^2 h_2 \\
&\quad - 360 A_w C^2 E^2 L_w R T T_{\text{amb}} c_A^2 \epsilon_{\max}^2 h_2
\end{aligned}$$

$$\begin{aligned}
\mathcal{Q} &= 90 A_w L_w \Omega R a_A h_0 \xi_M (c_A - \Theta) \\
&\quad + 270 A_w L_w \Omega R T^2 a_A c_A h_2 \xi_M - 270 A_w L_w \Omega R T^2 \Theta a_A h_2 \xi_M \\
&\quad - 180 A_w L_w \Omega R T T_{\text{amb}} a_A c_A h_2 \xi_M + 180 A_w L_w \Omega R T \Theta T_{\text{amb}} a_A h_2 \xi_M \\
&\quad + 90 A_w SEL_w \Omega R a_A c_A \epsilon_{\max} h_0 \xi_M \\
&\quad + 270 A_w SEL_w \Omega R T^2 a_A c_A \epsilon_{\max} h_2 \xi_M - 180 A_w SEL_w \Omega R T T_{\text{amb}} a_A c_A \epsilon_{\max} h_2 \xi_M
\end{aligned}$$

$$J_{f4,2} = \frac{-2Sc_A\epsilon_{\max}}{R\,c_p\,m_w\,r\,\pi D^2}\left(\mathcal{C}\cos\mathcal{T} + \mathcal{S}\sin\mathcal{T} + \mathcal{Q}\sin^2\mathcal{T} + \mathcal{K}\right)$$

$$\mathcal{T} = \frac{a_A\left(\sigma + A_s c_A - Tc_A\right)}{c_A}$$

$$D = 2c_A + \Omega a_A \xi_M \sin\mathcal{T} + 2SEc_A\epsilon_{\max}$$

$$\begin{aligned}
\mathcal{C} &= 180L_w\Omega V^2 a_A^2 c_A \xi_M - 180L_w\Omega\Theta V^2 a_A^2 \xi_M \\
&+ 180A_w L_w \Omega RT\Theta a_A^2 h_0 \xi_M - 180A_w L_w \Omega R\Theta T_{\text{amb}} a_A^2 h_0 \xi_M \\
&- 180A_w L_w \Omega RT a_A^2 c_A h_0 \xi_M + 180A_w L_w \Omega RT_{\text{amb}} a_A^2 c_A h_0 \xi_M \\
&+ 180A_w L_w \Omega RT^3\Theta a_A^2 h_2 \xi_M - 180A_w L_w \Omega RT^3 a_A^2 c_A h_2 \xi_M \\
&- 180A_w L_w \Omega RT^2\Theta T_{\text{amb}} a_A^2 h_2 \xi_M + 180A_w L_w \Omega RT^2 T_{\text{amb}} a_A^2 c_A h_2 \xi_M \\
&+ 180SEL_w\Omega V^2 a_A^2 c_A \epsilon_{\max}\xi_M \\
&+ \pi E\Omega R a_A^2 c_p m_w r\,\dot{\theta_C}\,\xi_M \\
&- 180A_w SEL_w \Omega RT a_A^2 c_A \epsilon_{\max} h_0 \xi_M + 180A_w SEL_w \Omega RT_{\text{amb}} a_A^2 c_A \epsilon_{\max} h_0 \xi_M \\
&- 180A_w SEL_w \Omega RT^3 a_A^2 c_A \epsilon_{\max} h_2 \xi_M + 180A_w SEL_w \Omega RT^2 T_{\text{amb}} a_A^2 c_A \epsilon_{\max} h_2 \xi_M
\end{aligned}$$

$$\begin{aligned}
\mathcal{S} &= 180A_w L_w \Omega R\Theta a_A h_0 \xi_M + 180A_w L_w \Omega R a_A c_A h_0 \xi_M \\
&+ 540A_w L_w \Omega RT^2\Theta a_A h_2 \xi_M + 540A_w L_w \Omega RT^2 a_A c_A h_2 \xi_M \\
&- 360A_w L_w \Omega RT\Theta T_{\text{amb}} a_A h_2 \xi_M - 360A_w L_w \Omega RTT_{\text{amb}} a_A c_A h_2 \xi_M \\
&+ 180A_w SEL_w \Omega R a_A c_A \epsilon_{\max} h_0 \xi_M \\
&+ 540A_w SEL_w \Omega RT^2 a_A c_A \epsilon_{\max} h_2 \xi_M - 360A_w SEL_w \Omega RTT_{\text{amb}} a_A c_A \epsilon_{\max} h_2 \xi_M
\end{aligned}$$

$$\begin{aligned}
\mathcal{Q} &= 90A_w L_w \Omega^2 R a_A^2 h_0 \xi_M^2 \\
&+ 270A_w L_w \Omega^2 RT^2 a_A^2 h_2 \xi_M^2 \\
&- 180A_w L_w \Omega^2 RTT_{\text{amb}} a_A^2 h_2 \xi_M^2
\end{aligned}$$

$$\begin{aligned}
\mathcal{K} &= 360A_w L_w R\Theta c_A h_0 + 1080A_w L_w RT^2\Theta c_A h_2 - 720A_w L_w RT\Theta T_{\text{amb}} c_A h_2 \\
&+ 360A_w SEL_w R\Theta c_A \epsilon_{\max} h_0 + 1080A_w SEL_w RT^2\Theta c_A \epsilon_{\max} h_2 \\
&- 720A_w SEL_w RT\Theta T_{\text{amb}} c_A \epsilon_{\max} h_2
\end{aligned}$$

$$J_b = \begin{bmatrix} J_{b1,1} & J_{b1,2} & 0 & 0 \\ 0 & J_{b2,2} & 0 & 0 \\ J_{b3,1} & J_{b3,2} & 0 & 0 \\ J_{b4,1} & J_{b4,2} & 0 & 0 \end{bmatrix}$$

$$J_{b1,1} = \frac{\Omega {a_M}^2 c_A \cos\left(\frac{a_M\left(\sigma + M_f c_M - T c_M\right)}{c_M}\right)(\xi_A - 1)\, N}{90 L_w R c_M c_p m_w D^2}$$

$$\begin{aligned} N = {} & 180 L_w V^2 c_A \\ & - 180 L_w \Theta V^2 \\ & + 180 A_w L_w R T \Theta h_0 \\ & - 180 A_w L_w R \Theta T_{\text{amb}} h_0 \\ & - 180 A_w L_w R T c_A h_0 \\ & + 180 A_w L_w R T_{\text{amb}} c_A h_0 \\ & + 180 A_w L_w R T^3 \Theta h_2 \\ & + 180 S E L_w V^2 c_A \epsilon_{\max} \\ & - 180 A_w L_w R T^3 c_A h_2 \\ & - 180 A_w L_w R T^2 \Theta T_{\text{amb}} h_2 \\ & + 180 A_w L_w R T^2 T_{\text{amb}} c_A h_2 \\ & + \pi E R c_p \dot{\theta_C} m_w r \\ & - 180 A_w S E L_w R T c_A \epsilon_{\max} h_0 \\ & + 180 A_w S E L_w R T_{\text{amb}} c_A \epsilon_{\max} h_0 \\ & - 180 A_w S E L_w R T^3 c_A \epsilon_{\max} h_2 \\ & + 180 A_w S E L_w R T^2 T_{\text{amb}} c_A \epsilon_{\max} h_2) \end{aligned}$$

$$\begin{aligned} D = {} & 2 c_A + \Omega a_M \sin\left(\frac{a_M\left(\sigma + M_f c_M - T c_M\right)}{c_M}\right) \\ & - \Omega a_M \xi_A \sin\left(\frac{a_M\left(\sigma + M_f c_M - T c_M\right)}{c_M}\right) + 2 S E c_A \epsilon_{\max} \end{aligned}$$

$$J_{b3,1} = \frac{{a_M}^2 c_A \cos\left(\frac{a_M\left(\sigma + M_f c_M - T c_M\right)}{c_M}\right)\left(SE\epsilon_{\max} + 1\right)\left(\xi_A - 1\right)N}{90 L_w R c_M c_p m_w D^2}$$

$$\begin{aligned}
N = {} & 180 L_w V^2 c_A \\
& - 180 L_w \Theta V^2 \\
& + 180 A_w L_w R T \Theta h_0 \\
& - 180 A_w L_w R \Theta T_{\text{amb}} h_0 \\
& - 180 A_w L_w R T c_A h_0 \\
& + 180 A_w L_w R T_{\text{amb}} c_A h_0 \\
& + 180 A_w L_w R T^3 \Theta h_2 \\
& + 180 S E L_w V^2 c_A \epsilon_{\max} \\
& - 180 A_w L_w R T^3 c_A h_2 \\
& - 180 A_w L_w R T^2 \Theta T_{\text{amb}} h_2 \\
& + 180 A_w L_w R T^2 T_{\text{amb}} c_A h_2 + \pi E R c_p \dot{\theta_C} m_w r \\
& - 180 A_w S E L_w R T c_A \epsilon_{\max} h_0 \\
& + 180 A_w S E L_w R T_{\text{amb}} c_A \epsilon_{\max} h_0 \\
& - 180 A_w S E L_w R T^3 c_A \epsilon_{\max} h_2 \\
& + 180 A_w S E L_w R T^2 T_{\text{amb}} c_A \epsilon_{\max} h_2
\end{aligned}$$

$$\begin{aligned}
D = {} & 2 c_A + \Omega a_M \sin\left(\frac{a_M\left(\sigma + M_f c_M - T c_M\right)}{c_M}\right) \\
& - \Omega a_M \xi_A \sin\left(\frac{a_M\left(\sigma + M_f c_M - T c_M\right)}{c_M}\right) + 2 S E c_A \epsilon_{\max}
\end{aligned}$$

$$J_{b4,1} = -\frac{2C\Omega {a_M}^2 c_A \epsilon_{\max} \cos\left(\frac{a_M\left(\sigma + M_f c_M - T c_M\right)}{c_M}\right)(\xi_A - 1)\, N}{R c_M c_p m_w r \pi D^2}$$

$$\begin{aligned} N = (&180 L_w V^2 c_A \\ &- 180 L_w \Theta V^2 \\ &+ 180 A_w L_w R T \Theta h_0 \\ &- 180 A_w L_w R \Theta T_{\text{amb}} h_0 \\ &- 180 A_w L_w R T c_A h_0 \\ &+ 180 A_w L_w R T_{\text{amb}} c_A h_0 \\ &+ 180 A_w L_w R T^3 \Theta h_2 \\ &+ 180 C E L_w V^2 c_A \epsilon_{\max} \\ &- 180 A_w L_w R T^3 c_A h_2 \\ &- 180 A_w L_w R T^2 \Theta T_{\text{amb}} h_2 \\ &+ 180 A_w L_w R T^2 T_{\text{amb}} c_A h_2 \\ &+ \pi E R c_p \dot{\theta_C} m_w r \\ &- 180 A_w C E L_w R T c_A \epsilon_{\max} h_0 \\ &+ 180 A_w C E L_w R T_{\text{amb}} c_A \epsilon_{\max} h_0 \\ &- 180 A_w C E L_w R T^3 c_A \epsilon_{\max} h_2 \\ &+ 180 A_w C E L_w R T^2 T_{\text{amb}} c_A \epsilon_{\max} h_2 \end{aligned}$$

$$\begin{aligned} D = {} & 2c_A + \Omega a_M \sin\left(\frac{a_M\left(\sigma + M_f c_M - T c_M\right)}{c_M}\right) \\ & - \Omega a_M \xi_A \sin\left(\frac{a_M\left(\sigma + M_f c_M - T c_M\right)}{c_M}\right) + 2CE c_A \epsilon_{\max} \end{aligned}$$

$$J_{b1,2} = \frac{c_A}{90\,L_w R c_p m_w D^2}\left(\mathcal{C}\cos\mathcal{T} + \mathcal{S}\sin\mathcal{T} + \mathcal{Q}\sin^2\mathcal{T} + \mathcal{K}\right)$$

$$\mathcal{T} = \frac{a_M\left(\sigma + M_f c_M - T c_M\right)}{c_M}$$

$$D = 2c_A + \Omega a_M \sin\mathcal{T} - \Omega a_M \xi_A \sin\mathcal{T} + 2SEc_A\epsilon_{\max}$$

$$\begin{aligned}
\mathcal{C} &= -180L_w\Omega\Theta V^2 a_M^2 + 180L_w\Omega V^2 a_M^2 c_A - 180L_w\Omega V^2 a_M^2 c_A\xi_A \\
&+ 180L_w\Omega\Theta V^2 a_M^2\xi_A + 180A_w L_w\Omega RT\Theta a_M^2 h_0 - 180A_w L_w\Omega R\Theta T_{\text{amb}} a_M^2 h_0 \\
&- 180A_w L_w\Omega RT a_M^2 c_A h_0 + 180A_w L_w\Omega RT_{\text{amb}} a_M^2 c_A h_0 + 180A_w L_w\Omega RT^3\Theta a_M^2 h_2 \\
&- 180A_w L_w\Omega RT^3 a_M^2 c_A h_2 - 180A_w L_w\Omega RT^2\Theta T_{\text{amb}} a_M^2 h_2 \\
&+ 180A_w L_w\Omega RT^2 T_{\text{amb}} a_M^2 c_A h_2 + 180SEL_w\Omega V^2 a_M^2 c_A\epsilon_{\max} \\
&- 180SEL_w\Omega V^2 a_M^2 c_A\epsilon_{\max}\xi_A + \pi E\Omega R a_M^2 c_p m_w r\,\dot{\theta_C} - \pi E\Omega R a_M^2 c_p m_w r\,\xi_A\,\dot{\theta_C} \\
&- 180A_w SEL_w\Omega RT a_M^2 c_A\epsilon_{\max} h_0 + 180A_w SEL_w\Omega RT_{\text{amb}} a_M^2 c_A\epsilon_{\max} h_0 \\
&- 180A_w SEL_w\Omega RT^3 a_M^2 c_A\epsilon_{\max} h_2 + 180A_w SEL_w\Omega RT^2 T_{\text{amb}} a_M^2 c_A\epsilon_{\max} h_2 \\
&+ 180A_w SEL_w\Omega RT a_M^2 c_A\epsilon_{\max} h_0\xi_A - 180A_w SEL_w\Omega RT_{\text{amb}} a_M^2 c_A\epsilon_{\max} h_0\xi_A \\
&+ 180A_w SEL_w\Omega RT^3 a_M^2 c_A\epsilon_{\max} h_2\xi_A - 180A_w SEL_w\Omega RT^2 T_{\text{amb}} a_M^2 c_A\epsilon_{\max} h_2\xi_A \\
\mathcal{S} &= 180A_w L_w\Omega R\Theta a_M h_0 + 180A_w L_w\Omega R a_M c_A h_0 - 180A_w L_w\Omega R a_M c_A h_0\xi_A \\
&+ 540A_w L_w\Omega RT^2\Theta a_M h_2 + 540A_w L_w\Omega RT^2 a_M c_A h_2 - 540A_w L_w\Omega RT^2 a_M c_A h_2\xi_A \\
&- 360A_w L_w\Omega RT\Theta T_{\text{amb}} a_M h_2 - 360A_w L_w\Omega RTT_{\text{amb}} a_M c_A h_2 \\
&+ 360A_w L_w\Omega RTT_{\text{amb}} a_M c_A h_2\xi_A + 180A_w SEL_w\Omega R a_M c_A\epsilon_{\max} h_0 \\
&- 180A_w SEL_w\Omega R a_M c_A\epsilon_{\max} h_0\xi_A + 540A_w SEL_w\Omega RT^2 a_M c_A\epsilon_{\max} h_2 \\
&- 540A_w SEL_w\Omega RT^2 a_M c_A\epsilon_{\max} h_2\xi_A - 360A_w SEL_w\Omega RTT_{\text{amb}} a_M c_A\epsilon_{\max} h_2 \\
&+ 360A_w SEL_w\Omega RTT_{\text{amb}} a_M c_A\epsilon_{\max} h_2\xi_A \\
\mathcal{Q} &= 90A_w L_w\Omega^2 R a_M^2 h_0 - 180A_w L_w\Omega^2 R a_M^2 h_0\xi_A + 90A_w L_w\Omega^2 R a_M^2 h_0\xi_A^2 \\
&+ 270A_w L_w\Omega^2 RT^2 a_M^2 h_2 - 540A_w L_w\Omega^2 RT^2 a_M^2 h_2\xi_A + 270A_w L_w\Omega^2 RT^2 a_M^2 h_2\xi_A^2 \\
&- 180A_w L_w\Omega^2 RTT_{\text{amb}} a_M^2 h_2 + 360A_w L_w\Omega^2 RTT_{\text{amb}} a_M^2 h_2\xi_A \\
&- 180A_w L_w\Omega^2 RTT_{\text{amb}} a_M^2 h_2\xi_A^2 \\
\mathcal{K} &= 360A_w L_w R\Theta c_A h_0 + 1080A_w L_w RT^2\Theta c_A h_2 - 720A_w L_w RT\Theta T_{\text{amb}} c_A h_2 \\
&+ 360A_w SEL_w R\Theta c_A\epsilon_{\max} h_0 + 1080A_w SEL_w RT^2\Theta c_A\epsilon_{\max} \\
&- 720A_w SEL_w RT\Theta T_{\text{amb}} c_A\epsilon_{\max} h_2
\end{aligned}$$

$$J_{b2,2} = \frac{A_w\,\left(3\,h_2\,T^2 - 2\,T_{\text{amb}}\,h_2\,T + h_0\right)}{c_p\,m_w}$$

$$J_{b3,2} = \frac{-a_M(\xi_A - 1)}{90\, L_w R c_p m_w D^2} \left(\mathcal{C}\cos\mathcal{T} + \mathcal{S}\sin\mathcal{T} + \mathcal{Q}\sin^2\mathcal{T}\right)$$

$$\mathcal{T} = \frac{a_M\left(\sigma + M_f c_M - T c_M\right)}{c_M}$$

$$D = 2c_A + \Omega a_M \sin\mathcal{T} - \Omega a_M \xi_A \sin\theta + 2SEc_A\epsilon_{\max}$$

$$\begin{aligned}
\mathcal{C} &= 180L_wV^2a_Mc_A^2 - 180L_w\Theta V^2a_Mc_A - 180A_wL_wRTa_Mc_A^2h_0 \\
&+ 180A_wL_wRT_{\text{amb}}a_Mc_A^2h_0 + 180A_wL_wRT\Theta a_Mc_Ah_0 - 180A_wL_wR\Theta T_{\text{amb}}a_Mc_Ah_0 \\
&- 180A_wL_wRT^3a_Mc_A^2h_2 + 180A_wL_wRT^3\Theta a_Mc_Ah_2 + 180A_wL_wRT^2T_{\text{amb}}a_Mc_A^2h_2 \\
&- 180A_wL_wRT^2\Theta T_{\text{amb}}a_Mc_Ah_2 + 360SEL_wV^2a_Mc_A^2\epsilon_{\max} + 180C^2E^2L_wV^2a_Mc_A^2\epsilon_{\max}^2 \\
&+ \pi ERa_Mc_Ac_pm_wr\,\dot{\theta_C} \\
&- 360A_wSEL_wRTa_Mc_A^2\epsilon_{\max}h_0 + 360A_wSEL_wRT_{\text{amb}}a_Mc_A^2\epsilon_{\max}h_0 \\
&- 360A_wSEL_wRT^3a_Mc_A^2\epsilon_{\max}h_2 + 360A_wSEL_wRT^2T_{\text{amb}}a_Mc_A^2\epsilon_{\max}h_2 \\
&- 180A_wC^2E^2L_wRTa_Mc_A^2\epsilon_{\max}^2h_0 + 180A_wC^2E^2L_wRT_{\text{amb}}a_Mc_A^2\epsilon_{\max}^2h_0 \\
&- 180A_wC^2E^2L_wRT^3a_Mc_A^2\epsilon_{\max}^2h_2 + 180A_wC^2E^2L_wRT^2T_{\text{amb}}a_Mc_A^2\epsilon_{\max}^2h_2
\end{aligned}$$

$$\begin{aligned}
\mathcal{S} &= 180A_wL_wRc_A^2h_0 - 180A_wL_wR\Theta c_Ah_0 \\
&+ 540A_wL_wRT^2c_A^2h_2 - 540A_wL_wRT^2\Theta c_Ah_2 \\
&- 360A_wL_wRTT_{\text{amb}}c_A^2h_2 + 360A_wL_wRT\Theta T_{\text{amb}}c_Ah_2 \\
&+ 360A_wSEL_wRc_A^2\epsilon_{\max}h_0 \\
&+ 1080A_wSEL_wRT^2c_A^2\epsilon_{\max}h_2 - 720A_wSEL_wRTT_{\text{amb}}c_A^2\epsilon_{\max}h_2 \\
&+ 180A_wC^2E^2L_wRc_A^2\epsilon_{\max}^2h_0 + 540A_wC^2E^2L_wRT^2c_A^2\epsilon_{\max}^2h_2 \\
&- 360A_wC^2E^2L_wRTT_{\text{amb}}c_A^2\epsilon_{\max}^2h_2
\end{aligned}$$

$$\begin{aligned}
\mathcal{Q} &= 90A_wL_w\Omega Ra_Mh_0 - 90A_wL_w\Omega R\Theta a_Mh_0 \\
&+ 270A_wL_w\Omega RT^2a_Mh_2 - 270A_wL_w\Omega RT^2\Theta a_Mh_2 \\
&- 180A_wL_w\Omega RTT_{\text{amb}}a_Mh_2 \\
&+ \xi_A(90A_wL_w\Omega R\Theta a_Mh_0 - 90A_wL_w\Omega Ra_Mc_Ah_0 \\
&+270A_wL_w\Omega RT^2\Theta a_Mh_2 - 270A_wL_w\Omega RT^2a_Mc_Ah_2 - 180A_wL_w\Omega RT\Theta T_{\text{amb}}a_Mh_2)
\end{aligned}$$

$$J_{b4,2} = \frac{-2Sc_A\epsilon_{\max}}{Rc_p m_w r\pi D^2}\left(\mathcal{C}\cos\mathcal{T} + \mathcal{S}\sin\mathcal{T} + \mathcal{Q}\sin^2\mathcal{T} + \mathcal{K}\right)$$

$$\mathcal{T} = \frac{a_M\left(\sigma + M_f c_M - Tc_M\right)}{c_M}$$

$$D = 2c_A + \Omega a_M\sin\theta - \Omega a_M\xi_A\sin\mathcal{T} + 2SEc_A\epsilon_{\max}$$

$$\begin{aligned}
\mathcal{C} = {} & -180L_w\Omega\Theta V^2a_M^2 + 180L_w\Omega V^2a_M^2c_A - 180L_w\Omega V^2a_M^2c_A\xi_A + 180L_w\Omega\Theta V^2a_M^2\xi_A \\
& + 180A_wL_w\Omega RT\Theta a_M^2h_0 - 180A_wL_w\Omega R\Theta T_{\text{amb}}a_M^2h_0 - 180A_wL_w\Omega RTa_M^2c_Ah_0 \\
& + 180A_wL_w\Omega RT_{\text{amb}}a_M^2c_Ah_0 + 180A_wL_w\Omega RT^3\Theta a_M^2h_2 - 180A_wL_w\Omega RT^3a_M^2c_Ah_2 \\
& - 180A_wL_w\Omega RT^2\Theta T_{\text{amb}}a_M^2h_2 + 180A_wL_w\Omega RT^2T_{\text{amb}}a_M^2c_Ah_2 \\
& + 180SEL_w\Omega V^2a_M^2c_A\epsilon_{\max} - 180SEL_w\Omega V^2a_M^2c_A\epsilon_{\max}\xi_A \\
& + \pi E\Omega Ra_M^2c_pm_wr\,\dot{\theta_C} - \pi E\Omega Ra_M^2c_pm_wr\,\xi_A\,\dot{\theta_C} \\
& - 180A_wSEL_w\Omega RTa_M^2c_A\epsilon_{\max}h_0 + 180A_wSEL_w\Omega RT_{\text{amb}}a_M^2c_A\epsilon_{\max}h_0 \\
& - 180A_wSEL_w\Omega RT^3a_M^2c_A\epsilon_{\max}h_2 + 180A_wSEL_w\Omega RT^2T_{\text{amb}}a_M^2c_A\epsilon_{\max}h_2 \\
& + 180A_wSEL_w\Omega RTa_M^2c_A\epsilon_{\max}h_0\xi_A - 180A_wSEL_w\Omega RT_{\text{amb}}a_M^2c_A\epsilon_{\max}h_0\xi_A \\
& + 180A_wSEL_w\Omega RT^3a_M^2c_A\epsilon_{\max}h_2\xi_A - 180A_wSEL_w\Omega RT^2T_{\text{amb}}a_M^2c_A\epsilon_{\max}h_2\xi_A
\end{aligned}$$

$$\begin{aligned}
\mathcal{S} = {} & 180A_wL_w\Omega R\Theta a_Mh_0 + 180A_wL_w\Omega Ra_Mc_Ah_0 - 180A_wL_w\Omega Ra_Mc_Ah_0\xi_A \\
& + 540A_wL_w\Omega RT^2\Theta a_Mh_2 + 540A_wL_w\Omega RT^2a_Mc_Ah_2 - 540A_wL_w\Omega RT^2a_Mc_Ah_2\xi_A \\
& - 360A_wL_w\Omega RT\Theta T_{\text{amb}}a_Mh_2 - 360A_wL_w\Omega RTT_{\text{amb}}a_Mc_Ah_2 \\
& + 360A_wL_w\Omega RTT_{\text{amb}}a_Mc_Ah_2\xi_A + 180A_wSEL_w\Omega Ra_Mc_A\epsilon_{\max}h_0 \\
& - 180A_wSEL_w\Omega Ra_Mc_A\epsilon_{\max}h_0\xi_A + 540A_wSEL_w\Omega RT^2a_Mc_A\epsilon_{\max}h_2 \\
& - 540A_wSEL_w\Omega RT^2a_Mc_A\epsilon_{\max}h_2\xi_A - 360A_wSEL_w\Omega RTT_{\text{amb}}a_Mc_A\epsilon_{\max}h_2 \\
& + 360A_wSEL_w\Omega RTT_{\text{amb}}a_Mc_A\epsilon_{\max}h_2\xi_A
\end{aligned}$$

$$\begin{aligned}
\mathcal{Q} = {} & 90A_wL_w\Omega^2Ra_M^2h_0 - 180A_wL_w\Omega^2Ra_M^2h_0\xi_A + 90A_wL_w\Omega^2Ra_M^2h_0\xi_A^2 \\
& + 270A_wL_w\Omega^2RT^2a_M^2h_2 - 540A_wL_w\Omega^2RT^2a_M^2h_2\xi_A + 270A_wL_w\Omega^2RT^2a_M^2h_2\xi_A^2 \\
& - 180A_wL_w\Omega^2RTT_{\text{amb}}a_M^2h_2 + 360A_wL_w\Omega^2RTT_{\text{amb}}a_M^2h_2\xi_A \\
& - 180A_wL_w\Omega^2RTT_{\text{amb}}a_M^2h_2\xi_A^2
\end{aligned}$$

$$\begin{aligned}
\mathcal{K} = {} & 360A_wL_wR\Theta c_Ah_0 + 1080A_wL_wRT^2\Theta c_Ah_2 - 720A_wL_wRT\Theta T_{\text{amb}}c_Ah_2 \\
& + 360A_wSEL_wR\Theta c_A\epsilon_{\max}h_0 + 1080A_wSEL_wRT^2\Theta c_A\epsilon_{\max}h_2 \\
& - 720A_wSEL_wRT\Theta T_{\text{amb}}c_A\epsilon_{\max}h_2
\end{aligned}$$

$$J_n = \begin{bmatrix} 0 & J_{n1,2} & 0 & 0 \\ 0 & J_{n2,2} & 0 & 0 \\ 0 & 0 & 0 & 0 \\ 0 & J_{n4,2} & 0 & 0 \end{bmatrix}$$

$$J_{n1,2} = \frac{A_w \Theta \left(3h_2 T^2 - 2T_{\text{amb}} h_2 T + h_0\right)}{c_p m_w \left(SE\epsilon_{\max} + 1\right)}$$

$$J_{n2,2} = \frac{A_w \left(3h_2 T^2 - 2T_{\text{amb}} h_2 T + h_0\right)}{c_p m_w}$$

$$J_{n4,2} = -\frac{180 A_w S L_w \Theta \epsilon_{\max} \left(3h_2 T^2 - 2T_{\text{amb}} h_2 T + h_0\right)}{c_p m_w r \pi \left(SE\epsilon_{\max} + 1\right)}$$